Remote Sensing based Method for Glacier Surface Velocity and Ice Thickness Distribution Estimations

Submitted in partial fulfillment of the requirements

of the degree of

Doctor of Philosophy

of the
Indian Institute of Technology Bombay, India
and
Monash University, Australia

by

Sangita Kumari

The course of study for this award was developed jointly by
Monash University, Australia and the Indian Institute of Technology Bombay, India
and was given academic recognition by each of them.
The programme was administrated by The IITB-Monash Research Academy

(Feb 2021)

COPYRIGHT NOTICE

DECLARATION

I declare that this written submission contains my ideas in my own words and where other's ideas or words have been included, I have adequately cited and referenced the original sources. I also declare that I have adhered to all principles of academic honesty and integrity and have not misrepresented or fabricated or falsified any idea/data/fact/source in my submission. I understand that any violation of the above will cause disciplinary action by the Institute and can evoke penal action from the sources which have not been properly cited or from whom proper permission has not been taken when needed.

Singh

Sangita Kumari

(Name)

154044002

(Roll No.)

Date: 28/02/2021

ABSTRACT

The melting of ice mass and glaciers worldwide has been mentioned as one of the most prominent indicators of climate change (IPCC 2014). Glaciers, excluding Greenland and the Antarctic region, have been reported to undergo rapid changes in response to climate change (Vaughan et al., 2013) and the consequences of their mass loss are of global significance. Additionally, melting glaciers pose a variety of risks such as glacial lake outburst floods (GLOF) and contamination of nearby water bodies due to toxic substances present in the glaciers (Nagorski et al., 2014; Hock et al., 2019). Glacier ice thickness distribution gives an idea of total water capacity maintained by a glacier at a given time, which is crucial for quantifying glacial ice melt and used in many glaciological applications. Thus, it is important that glacier ice thickness be monitored globally (Huss et al., 2008; Gabbi et al., 2012; Jouvet et al., 2009; Allen, Schneider, and Owens 2009; Linsbauer et al., 2016). Given that the field-based approaches are limited to only a few accessible glaciers, it is necessary to develop alternate approaches to estimate ice-thickness distribution globally. Glacier ice thickness modelling approaches provide an alternative to glacier monitoring where the ground-based surveys are difficult to carry out.

In the present research, a physics-based glacier ice thickness model has been presented which uses remotely sensed glacier surface velocity. To estimate the glacier surface velocity, a new algorithm for automated glacier feature tracking named as SWIFT (**S**patially varying **WI**ndow based maximum likelihood **F**eature **T**racking) has been proposed. This algorithm utilises both optical data (to determine the window size) and Synthetic Aperture Radar (SAR) data (to perform feature tracking). The proposed glacier feature tracking algorithm uses a spatially varying window size unlike other existing softwares like SNAP, SARscape, CIAS and COSI-Corr that cannot provide the flexibility of spatially varying window sizes. Moreover, this method for estimation of window size can be implemented in combination with other existing feature tracking methods. The proposed glacier surface velocity tracking algorithm has been tested for three different glaciers (South Glacier, Chhota Shigri Glacier and Tasman Glacier) for which the field measured data were available for validation. The methodology has been demonstrated with a variety of SAR and optical satellite data. Moreover, the effect of different satellite data characteristics on glacier surface velocity estimation have been explored to prove the effectiveness of the technique. The obtained results for all the three study glaciers indicate

that the proposed spatially varying window size based estimates shows consistent improvement over spatially fixed window size based estimates. Moreover, the performance evaluation against the normalized cross correlation method (NCC) with calibrated window size revealed the better performance of the proposed feature tracking approach (no calibration required) in the middle and upper zones of the three study glaciers. This indicates that the proposed glacier feature tracking method holds potential for feature tracking in glaciers with no prior field information available.

The proposed model to estimate glacier ice thickness is named GATHI **(G**l**A**cier ice **THI**ckness distribution using remote sensing) which requires only remotely sensed inputs such as surface velocity and DEM. The performance of the model was assessed through application in four study glaciers. Along with the ice thickness modelling, GPR based ice thickness measurement over Patsio Glacier has been collected. This data which has been used for ice thickness model validation in this study shall be also useful for future glacier ice thickness modelling studies.

To explore the applicability of the ice thickness model to glaciers without any field ice thickness measurements available, two different scenarios were considered. In scenario 1, the transferability of the model parameter from one glacier (with available field observations) to other glaciers sharing similar characteristics (with no available field measurements) was explored. These observations revealed that for the ice thickness model application, the two calibrated model parameters $A = 3.8*10^{-24}$ and $n = 3$ can be assumed to be constant for temperate type glaciers. In scenario 2, considering that the geometry-based parameter f cannot be replicated from one glacier to other, potential for field-data-independent calibration (Ramsankaran et al., 2018) was explored. The obtained results showed that the field-data-independent calibration led to noticeable improvement in mean error of the ice thickness. Accordingly, the error in estimated ice thickness was reduced by 5-17% (of mean observed ice thickness) when calibrated shape factor was used instead of the uncalibrated shape factor.

To explore the effect of calibration data on the ice thickness model, the model's sensitivity was evaluated towards observation's spatial and quantity-related characteristics. The result indicates that, although it is convenient from the logistical point of view, survey configurations where low elevations are sampled should be avoided, or at least should be complemented with measurements gathered along the glacier central flowline.

In the present study, the proposed ice thickness model has been developed and tested over four study glaciers located in different regions around the world. The model along with the self-calibration approach showed noticeable improvements over the uncalibrated modelled estimates. Moreover, the approach does not require extensive parameterization or field data. Hence, it has a significant potential for ice thickness estimation over data-scarce glaciers. However, further experiments need to be carried out to examine the implementation capability of the proposed ice thickness model at regional scale considering the factors such as availability of data and computational efficiency.

GRAPHICAL ABSTRACT

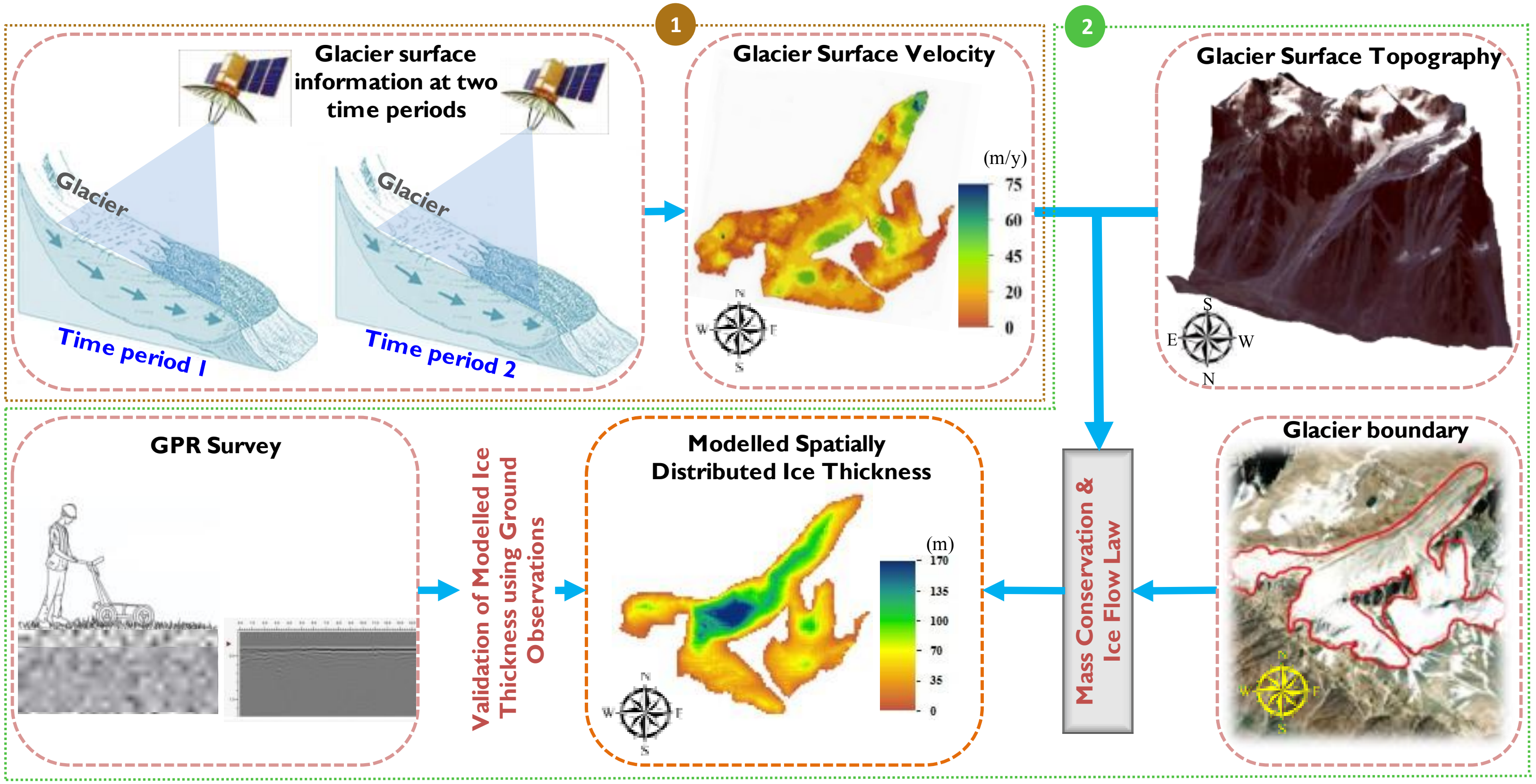

1 Remote sensing based estimation of glacier surface velocity

2 Modelling of spatially distributed glacier ice thickness using only remotely sensed inputs

ACKNOWLEDGEMENT

"A dream does not become reality through magic;
it takes sweat, determination, and hard work."

First of all, I would like to express my sincere gratitude to my supervisor at IITB, Prof. RAAJ Ramsankaran who has helped me to evolve as a better researcher through my PhD journey. His insights, valuable suggestions and continuous support which made me strive towards perfection. Over the years, I have learnt different aspects of research through numerous one to one conversations specially during the later stages of my PhD. Through his keen personal involvement in each of his student he has not only helped me evolve as a researcher but also added to my personal growth.

Jeff, has also been very supportive and encouraging supervisor and mentor to me. His guidance always made sure keeping me focused on the quality as well as the deadlines of my work. His concise but helpful feedback at every stage of my research, helped not only to get a different perspective on my research but also improved the quality of my research and documentation work. I hope that I get both of my supervisors' sound advice throughout my future career.

Besides my advisors, sincere thanks also go to the rest of my PhD review committee: Prof. E. P. Rao, Prof. Avik Bhattacharya, Prof. Chris Rudiger and Prof. Eswar Rajasekaran for their insightful and critical comments that has helped my thesis reach to the present shape.

Special thanks to the IITB-Monash Research Academy who made this PhD possible. The staff at the academy have provided a home like feel where Nancy acted as our caretaker. Jayashree, Kuheli, Laya who never get tired of clearing my doubts (which are a lot!). I also thank Kuheli and Kiran who handled all my finance related issues.

I thank my fellow lab mates (H-RSA Group): Ankur sir, Ashish sir, Anita di, Antara, Amol, Estifanos, KD, Sujith sir, Navin, Pratiksha, Sathya, Shruthi di, Swathy, Smarika, Jaya, Vivek, Shivraj sir and Vishveswaran for fun filled conversations which always led to improve my writing, presentation or research skills.

A significant part of my PhD includes the GPR surveys at the Himalayan Glaciers. I thank all of my team members specially RAAJ sir for making this possible. I am also thankful to my fellow researchers, KD, Ankur sir, Parla, Smarika, Anisha, Vivek, Navin, Anirudha, Yogesh, Thupstan sir and Som who made these trips entertaining as well. My special thanks to all the *porters* during my fieldwork who helped our team to cope with the difficulties during the treks and surveys specially near the crevasses. All through the climb, porters replenished the supplies of essential goods.

I am very grateful to IITB-Monash Research Academy, IRCC and Civil department, IIT Bombay for providing monetary support during my research work.

My friends whom I met through IITB Monash academy, *Debo, Tagori, Uzma, Priyanka, Chandrima* and *Niti,* have shared this joint PhD program's experience and accompanied me through the program's challenges and perks.

I would like to express my deepest gratitude to my parents Mummy and Papa for their unconditional love and continuous support throughout my life. You have motivated me at my lowest low. You both are the pillars of my life. I convey my special acknowledgment to my brother *Rahul* and adorable sisters *Nina* and *Buttu* who reminded me prime concern '*Do not deviate, focus and finish'*. No matter how far we were, your conversations never made me feel like away from home and thus made me stay happily at the hostel and work more productively. Last but not the least, I would like to thank my husband, best friend, and fellow partner in the glacier expedition, KD, whom I met at IITB during the course of my PhD and has been my silent partner since then. Whether professional or personal he has been equally understanding and supportive towards my goals. He has taught me to be more organized in the way I work.

I thank you all for being in my life!

Though unexpected, I would like to thank COVID-19 which almost put my thesis work to stagnation but also helped me realize the importance of social life and what impact it has on our mental wellbeing. It has also made me realize the importance of facilities like high-speed internet and excellent hostel facilities given to us at the campus which we took for granted.

Above all, I owe this research to the Almighty *God* for bestowing me the strength and perception to undertake this research task and enabling me to its completion.

CONTENTS

LIST OF FIGURES

LIST OF TABLES

ABBREVIATIONS

Abbreviation	Description
ALOS	Advanced Land Observing Satellite
ALS	Average Linear Sensitivity
ANN	Artificial Neural Network
AR5	Fifth Assessment Report
ASTER	Advanced Spaceborne Thermal Emission and Reflection Radiometer
CDEM	Canadian Digital Elevation Model
CFL	Central Flowline
DEM	Digital Elevation Model
DGNSS	Differential Global Positioning System
DLR	German Aerospace Center
ELA	Equilibrium Line Altitude
GATHI	GlAcier ice THIckness distribution using remote sensing
GIS	Geographic information system
GlabTop	Glacier Bed Topography
GLIMS	Global Land Ice Measurements from Space initiative
GLOF	Glacial lake outburst floods
GPR	Ground Penetrating Radar
GSI	Geological Survey of India
HKH	Hindu Kush Himalayan
IDW	Inverse Distance Weighting
InSAR	Interferometric SAR
ITMIX	Ice Thickness Model Intercomparison eXperiment
IH	Indian Himalayan
IPCC	Inter-Governmental Panel on Climate Change
ITEM	Ice Thickness Estimation Method
m a.s.l	Meters above sea level
NASA	National Aeronautics and Space Administration
RISAT	Radar Imaging Satellite
RGI	Randolph Glacier Inventory
RMSE	Root Mean Square Error

SAR	Synthetic Aperture Radar
SCE	Shuffle Complex Evolution
SIA	Shallow Ice Approximation
SPOT	Satellites Pour l'Observation de la Terre
SRTM	Shuttle Radar Topography Mission
SSA	Shallow-Shelf Approximation
SWIFT	Spatially varying WIndow based maximum likelihood Feature Tracking
USGS	United States Geological Survey
WGI	World Glacier Inventory

SYMBOL AND NOTATIONS

Symbol and Notation	Description
$\dot{b}$	The rate of ice accumulation or melting at a location on the glacier surface
B	the total glacier net balance
$\bar{B}$	the specific net balance
H/h	Ice thickness
$\bar{h}$	Mean ice thickness
u	components of ice velocity along x direction
v	components of ice velocity along y direction
w	components of ice velocity along z direction
u_s	components of surface ice velocity along x direction (along glacier flowline)
v_s	components of surface ice velocity along y direction (across glacier flowline)
w_s	components of surface ice velocity along z direction (vertical)
τ_d	Driving stress
ρ	Density of ice
g	Gravitational acceleration due to gravity
τ_b	Basal shear stress
f	Shape factor
α	Surface slope
β	Bed slope
$\dot{\epsilon}$	Shear strain
A	Creep parameter
n	Creep or Glen’s flow law exponent
τ	Shear stress
f_{cs}	Shape factor at a given cross section
f_{cs_avg}	Average of the shape factor estimated at different cross sections
$f_{cs\_avg\_observed}$	Average of the shape factor observed at different cross sections
h_{avg_cs}	Average of the ice thickness estimated at different cross sections

w_{cs}	Width of glacier at a given cross section
P	Pressure
Δh	Elevation range
u_{b}	Basal ice flow velocity
$\frac{dq}{dx}$	Flux divergence along flowline
k	Total number of pixels in a block
N	Multi-looking factors
T	Temperature
$\overline{q_\iota}$	Mean specific ice flux at point i
q_i	ice flux at point i

CHAPTER 1

1 INTRODUCTION

This thesis presents a physics-based glacier ice thickness model for data scarce regions through utilization of remotely sensed glacier velocity information. The methodology for remote sensing based glacier surface velocity estimation and ice thickness estimation model were developed from the perspective of model independence from in-situ observations. The methodology has been demonstrated with a variety of Synthetic Aperture Radar (SAR) and optical satellite data. Moreover, the effect of different satellite data characteristics on glacier surface velocity estimation have been explored to prove the effectiveness of the technique. The proposed ice thickness estimation model was tested for four study glaciers distributed around the world.

1.1 Motivation

The recent Inter-Governmental Panel on Climate Change (IPCC) in its Fifth Assessment Report (AR5) highlighted the melting of ice mass and glaciers worldwide as one of the most prominent indicators of climate change (IPCC 2014). Glaciers, excluding Greenland and the Antarctic region, have been reported to undergo rapid changes in response to climate change (Vaughan et al., 2013). Although they contain only a fraction (~1%) of the ice volume worldwide (Lambeck et al., 2014), the consequences of their mass loss are widespread and of global significance. Glacier changes affect global trends in freshwater availability, have dominated cryospheric contributions to recent sea level changes, and are anticipated to affect regional water resources over the twenty-first century (IPCC 2014).

In mountain regions glacier melt contributes freshwater to rivers. In countries like China, India, and other parts of the Asian continent, many rivers are fed predominantly by snowmelt from the Himalaya, with a large part of river flow coming from melting glaciers towards the end of summer. Therefore, a rapid change in melting rate of these glaciers can heavily affect streamflow. Additionally, melting glaciers pose a variety of risks such as:

1. Outbursts of glacial lakes resulting in acute damage to local population due to extreme water discharges that may lead to a tremendous amount of socioeconomic loss, especially

for mountainous regions of the world. Past events include glacial lake outburst floods (GLOF) in Peru, (Lliboutry et al., 1977; Reynolds, 1992; Frey et al., 2018), British Columbia (Clague and Evans 2000), the Himalayas (Vuichard and Zimmermann, 1987; Yamada, 1998; Richardson and Reynolds, 2000), Central Asia (Popov, 1997) and North America (O'Connor and Costa, 1993; Evans and Clague, 1994; Clague and Evans, 2000). Many of these events were reported to have catastrophic effects.

2. Glacial rivers contamination which can have lasting and latent effects on remote areas. For example, melting Himalayan glaciers have been shown to contain organic pollutants while glaciers in the inland Tibetan Plateau are known to contain chemically toxic discharge (Zhang et al. 2017). Increased meltwater due to warming temperatures and extreme rainfall could lead to greater glacial river discharge, which would detach and transport higher levels of these chemicals.

Glacier ice thickness distribution gives an idea of total water capacity maintained by a glacier at a given time, which is crucial for quantifying glacial ice melt, and consequently their contribution to the above-mentioned risks and sea-level rise (Helfricht et al. 2019). Glacial ice thickness is also a fundamental parameter used in many glaciological applications, such as identification of potential future lake formation, glacial evolution modeling, runoff projection, and modelling the past, present and future condition of glaciers etc. Consequently, it is important that glacier ice thickness be monitored globally (Huss et al. 2008; Gabbi et al. 2012; Le Meur et al. 2007; Jouvet et al. 2009; Allen, Schneider, and Owens 2009; Frey et al. 2010; Paul and Linsbauer 2012; Linsbauer et al. 2016).

1.2 Problem Statement

The field measurement techniques to find glacier ice thickness include ice core drilling and geophysical techniques. Ice core drilling is a technique which serves as the most direct way to find the glacier ice thickness and to study subsurface processes. However, this is a cumbersome procedure involving huge manpower, time and cost. There have been several studies using ice core drilling to estimate the glacier ice thickness (eg. Athabasca glacier, Savage and Paterson., 1963; Ross Ice Shelf, Zagorodnov et al., 2014). Inferred methods include geophysical techniques such as Ground Penetrating Radar (GPR) for glacier ice thickness mapping in a non-destructive way.

However, these methods are also expensive, laborious and difficult due to logistical reasons, meaning that they can only be conducted during times of the year with favorable weather conditions. Moreover, determination of complete glacier wide ice thickness cannot be carried out directly but is necessarily linked to interpolation or extrapolation of direct (point) measurements.

Glacier thickness has been estimated around the world using ground-penetrating radar (GPR) (eg. Schaufelferner Glacier, Andrea Fischer, 2009; Degenhardt, 2009; Chhota Shigri Glacier, Azam et al., 2012; Tianshan glaciers, Wang et al., 2013; Svalbard glaciers, Saintenoy et al., 2013; Navarro et al., 2014 and other studies). The Himalayan region, due to its highest mountain ranges in the world, contains glaciers of the most inaccessible nature. In this region only a few field-based estimates (e.g. Gergan et al. 1999; Azam et al. 2012; Singh et al. 2012) are available, based on GPR measurements to estimate the ice-thickness and bedrock topography. Other field-based measurements can be used to estimate ice thickness with less expensive instrumentation (viz. stakes), such as mass balance and velocity, but these also suffer from accessibility. While these methods are limited to easily accessible glaciers, they are very useful for validation purpose.

Given that field-based approaches are limited to only a few accessible glaciers, it is necessary to develop alternate approaches to estimate ice-thickness distribution globally. Glacier ice thickness modelling approaches are known to complement the GPR based measurements where sparse observations are available. Elsewhere, these approaches provide an alternative to glacier monitoring where the ground-based surveys are difficult to carry out. A variety of glacier ice thickness models have been developed and can be classified according to a range of criteria including spatial and physical process representation and the nature of outputs given by the models. These approaches are based on either empirical relationships, simple physical models or complex models of ice dynamics and its variant. The physics-based models incorporate processes that closely represent glacial dynamics and thus can be more robust in representing a range of conditions, however they require certain field-based information which does not exist for every glacier. Considering the data scarcity over inaccessible glaciers, extraction of these information using simple and efficient approaches is needed.

To replace the field-based information required by the ice thickness models, satellite remote sensing can provide a suitable alternative. Moreover, it permits real-time, year-round and long-term monitoring of the glaciers. Since the launch of the first remote sensing satellite, remote sensing has proven to be valuable using data in different forms such as multispectral (e.g. Landsat, QuickBird), hyperspectral (e.g. Hyperion, AVIRIS) and microwave (e.g. RISAT-1, RADARSAT-1 & 2, ERS-1 &2, ENVISAT, ALOS PALSAR and TanDEM-X). The glacier-surface velocity, one of the important inputs to ice thickness modelling, can be easily retrieved using these remote sensing datasets. However, the retrieval method needs to be explored in the case of limited or no prior field information being available. Herein the proposed research is aimed to develop an ice thickness model based on remotely sensed inputs such as glacier-surface velocity, thus describing the glacier physics while utilizing the potential of ever evolving remote sensing technology.

1.3 Aim and Objectives of the Study

The primary aim of this research is to model the ice thickness distribution of glaciers using remotely sensed velocity due to the limitations identified above. Based on a detailed review of the literature and thus identified research gaps given in Chapter 3, the following research objectives have been formulated.

1. To develop a remote sensing-based feature tracking algorithm to estimate glacier surface velocity where optical data is used for window size determination and SAR data is used for feature tracking. The sub-objectives are:

- To develop an automated window size determination technique using optical data, to be useful SAR speckle feature tracking to estimate glacier surface velocity.
- To investigate the effect of different SAR and optical-data characteristics on the proposed feature tracking algorithm for glacier surface velocity estimation.
- To assess the performance against the existing methods for glacier surface velocity estimation.

2. To develop a physics-based glacier ice thickness model to estimate spatially distributed ice-thickness using remote sensing inputs. The sub-objectives are:

- To study the accuracy and performance of the proposed remote sensing-based glacier ice thickness model against field data and other modelling approaches respectively.

- To explore the model applicability for glaciers with different distribution of available field measured ice thickness information.

1.4 Scope of the Work

This study focused on glacier ice thickness model development using remote sensing data for data scarce regions, based on the Shallow Ice Approximation where longitudinal and other horizontal stresses are not considered. The remotely sensed inputs such as glacier surface velocity, surface topography and glacier outlines were considered. From these, only the glacier surface velocity was estimated with a focus on automation, while the other inputs such as DEM and glacier boundary have been taken from freely available sources and not been considered for further improvements in terms of quality and accuracy. The ice thickness estimation model was tested for various valley type glaciers, representing the majority of non-polar glacier types located in various climatic zones. The proposed ice thickness model has not been tested for glacier types such as cirques and piedmont glaciers. The physics in the model is also applicable to these glaciers so one can apply this model to these glacier types, however, need to be cautious.

1.5 Organisation of the Thesis

The research encompassed in this thesis is divided into seven chapters. Chapter 2 presents a brief overview of the fundamental processes involved in glacier dynamics. These include underlying principles, laws and their characteristics under certain assumptions as manifested in the existing categories of ice thickness models. This is followed by the Stokes equations which explain complex dynamic glacier processes, with the chapter ending with an introduction to the shallow ice approximation, which is the basis of the majority of ice thickness models available.

Chapter 3 presents a review of the state-of-the-art literature in studies of glacier ice thickness estimation based on the shallow ice approximation. Extensive discussions were constrained to physics-based model studies. The chapter concludes with the research gaps identified.

A detailed description of the four study glaciers and the data used in this thesis is presented in Chapter 4. Some critical topographical aspects and climate characteristics of these glaciers has been presented to understand the variability among the study glaciers. The study glaciers presented in this chapter are common to both the glacier velocity estimation in Chapter 5 and the ice thickness modelling in Chapter 6. The remote sensing and in-situ data used for glacier velocity estimation and ice thickness modelling were described in detail. In addition to freely available in-situ datasets used for validation, the in-situ glacier ice thickness data collected for this thesis via an extensive field survey at one of the study glaciers (Patsio Glacier) is described. To maintain the flow of the thesis, the estimated velocity used as one of the inputs to ice thickness model is described in Chapter 6.

The remote sensing based glacier surface velocity estimation component of this thesis is described in Chapter 5. At first, the theoretical background pertaining to development of the method for automatic determination of window size for image matching is given. Subsequently, the complete framework to estimate glacier surface velocity is presented and implemented for the study glaciers. Furthermore, the results from inter-comparison of the newly developed framework with other widely used methods were also reported.

Chapter 6 presents the modelling framework, application and assessment of the proposed ice thickness model. Following this, the estimation capabilities have been explored via the performance analysis for the four study glaciers. Moreover, a number of experiments were undertaking, seeking for possible improvements and automation, which is important for large scale application.

Chapter 7 summarizes the major contributions and conclusions of this thesis along with the limitations of the research. It concludes with a discussion on the future perspectives for each major research component of this thesis.

CHAPTER 2

2 THEORETICAL BACKGROUND

This chapter presents the basic concepts that represent the current understanding of glacier dynamics from an ice thickness modelling perspective. A wide range of processes which form the basis of existing physics-based ice thickness modelling approaches are described. These concepts are later used in the formulation of ice thickness modelling framework given in chapter 6. The following sections introduce the primary processes observed in a glacier system. Starting from an already formed glacier, the basics of glacier mechanics are presented based on glacier mass balance, which involves ice flow and the forces acting on a glacier. The chapter is organized such that simple individual components are given before proceeding to the complex representation of glacier system.

2.1 Glacier Formation

A glacier forms when snow melts and refreezes, or is compressed, to form ice. Once formed, glaciers flow under their own weight, channeled along constrained routes that are defined by the underlying bedrock. The ice moves by stretching in the flow direction, and by shearing or sometimes sliding over the bedrock. The velocity of ice flow is determined by several parameters such as glacier geometry, temperature, basal conditions, and the underlying stress (Cohen et al., 2018; Wu et al., 2019). Basal conditions determine whether sliding can occur and at what rate. Moreover, the driving force acting on the glacier is proportional to the ice thickness and surface geometry (Hughes et al., 2003; Wohland et al., 2016). Moreover, flow rates depend strongly on temperature; ice at 0°C flows much faster than at -10°C (Cuffey and Patterson, 2004). Consequently, theoretical models of glaciers must get both the dynamics and thermodynamics right if they are to approach reality.

2.2 Glacier Mass Balance

The glacier mass balance refers to changes in the mass of the glacier and the distribution of this change in space and time particularly, allowing the change in mass in a given year to be estimated (Cuffey and Paterson, 1994). The measure for this change is the specific balance rate, defined as the rate at which mass is added to or removed from a glacier. The rate of ice accumulation or melting at location x on the glacier surface is denoted as $\dot{b}$ (kg m^{-2} yr^{-1}). The sum of mass gain (accumulation) and mass loss (ablation) during a certain time span is therefore defined as the net balance.

In a hydrological year, which is considered from 1 October to 30 September, b can be evaluated by integrating over time interval t_1 to t_2 such that

$$b(x) = \int_{t_1}^{t_2} \dot{b}(x,t)dt. \tag{2.1}$$

This net balance is the mass gain or loss at a location x on the glacier surface. Therefore $b(x)$ describes the spatial distribution of mass balance over the glacier surface. Integrating this function over the glacier surface area S leads to the total glacier net balance B (kg) such that

$$B = \int_S b(x)dS. \tag{2.2}$$

The glacier net balance is the sum of accumulation and ablation over the whole glacier surface, and therefore the volume change of the glacier. Dividing the total mass balance by the glacier surface area gives the average net balance otherwise known as the specific net balance $\bar{B}$ (Kg m^{-2}) by

$$\bar{B} = \frac{B}{S}. \tag{2.3}$$

In general, these mass balance terms are stated in terms of water equivalent, so that comparisons can be made between different glaciers and years. When B is positive, the glacier is said to have a positive mass balance; if this condition persists for some years the glacier will advance. If it is negative it will retreat.

2.3 Principle of Mass Conservation

The principle of mass conservation states that the changes in ice thickness at any point must be due to the flow of the ice and local snowfall or loss due to melting. This conservation of mass is expressed by the continuity equation. Many important characteristics of glacier flow and evolution are manifestations of the requirement that mass be conserved. Figure 2.1 shows the accumulation and ablation processes in a typical valley glacier (Hooke, 2005). The vertically integrated continuity equation during long-term evolution of an ice mass, or its steady-state properties, can be represented by the relation (Cuffey and Patterson, 2004)

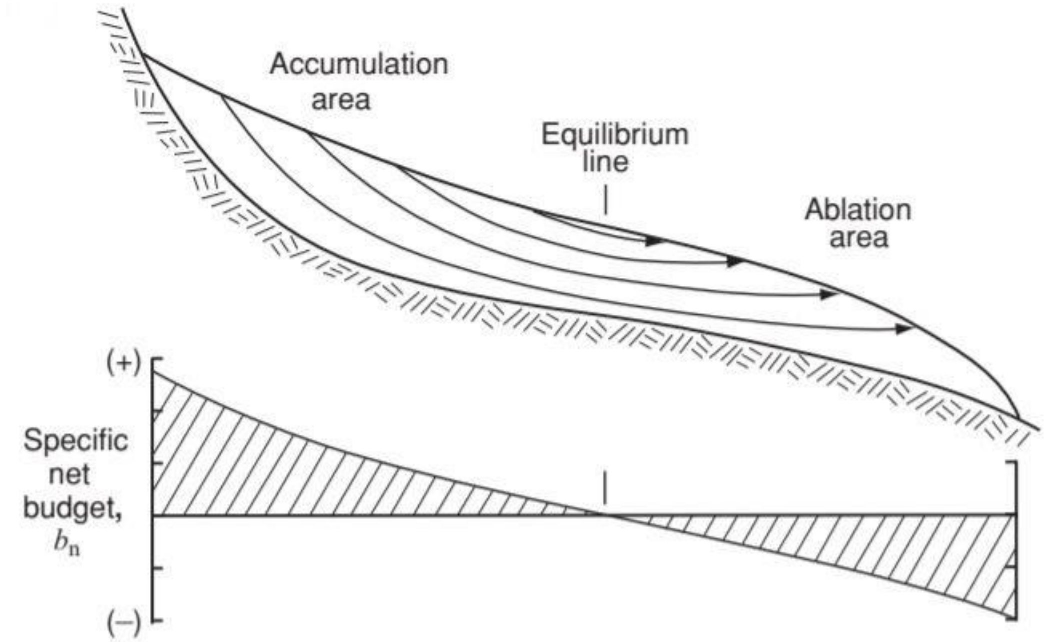

Figure 2.1 Accumulation and ablation processes in a typical valley glacier (Hooke, 2005).

$$\frac{\partial H}{\partial t} = b_i - \frac{\partial q}{\partial x}, \tag{2.4}$$

where the flux $q = uH$ is the flux averaged over depth, H is the ice thickness and b_i is the mass balance (m/yr). The underlying approximation here is i) a negligible internal mass balance compared to the surface and basal ones, and ii) a uniform ice density. The flux averaged over depth is essentially indistinguishable from q_i (flux at the surface) in an ablation zone or for a large ice sheet. However, for a total ice thickness of ~200 m, this error can contribute to about 6% uncertainty (Cuffey and Patterson, 2004).

It follows that the flux can also be represented as

$$\frac{\partial q}{\partial x} = b_i - \frac{\partial H}{\partial t}, \tag{2.5}$$

where the right hand side represents the apparent mass balance term, which according to kinematics is equivalent to

$$b_i - \frac{\partial H}{\partial t} = w - u\frac{\partial H}{\partial x} - v\frac{\partial H}{\partial y}, \tag{2.6}$$

where *u*, *v*, and *w* are the components of ice velocity along the *x*, *y* and *z* direction, respectively. If $w > 0$, upward flow raises the surface unless the ice is removed by ablation ($b < 0$). Conversely, flow downwards, that is, $w < 0$ lowers the surface unless ice is accumulated. Additionally, the surface also rises or falls as the horizontal flow (*u*, *v*) transports surface features along the glacier.

2.4 Driving Stresses and Glens Ice Flow Law

Under gravitational force, the glacier flows due to two different reasons: i) pressure gradients in the glacier and ii) the sloping glacier bed. A simple case with a parallel-sided slab of ice and thickness *H*, resting on a rough plane of slope α is shown in Figure 2.2a. If the length and width of the slab are assumed to be long compared to *H* and a column of ice with unit cross-section is kept perpendicular to the rough plane, the component parallel to the plane due to weight of the column is the driving stress, τ_d,. (Nm^{-2}) of the glacier. For equilibrium, resisting forces must balance the driving stress. On most glaciers, the largest resisting force is the basal drag, being the shear stress τ_b (also referred to as the basal shear stress) across the base of the column. Thus

$$\tau_d = \rho g H \text{ and } \tau_b = f\tau_d\,, \tag{2.7}$$

where *f* denotes a number usually of order one. Figure 2.2b and Figure 2.2c represent this stress component for ice mass with different basal and surface characteristics.

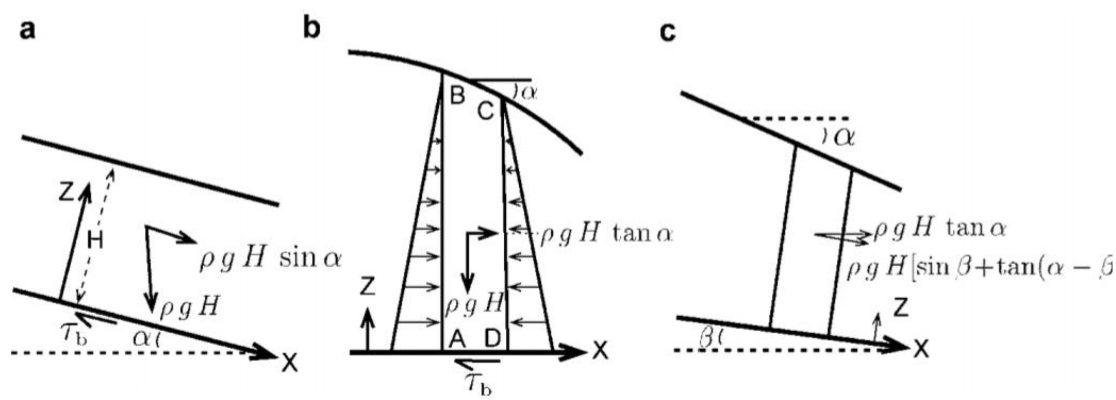

Figure 2.2 Gravitational forces composing the driving stress: (a) the down-slope component of weight, (b) the pressure gradient force, and (c) the combination (Hooke, 2006).

An ice mass resting on a horizontal surface at its base but having a surface slope of α represents an ice sheet or the lower zone of a large mountain glacier (Fig. 2.2b). The driving stress here is balanced by the basal drag such that

$$\tau_d = -\rho g H \frac{\partial S}{\partial x} = \rho g H \tan \alpha \; and \; \tau_b = f\tau_d \, , \qquad (2.8)$$

where *f* denotes a constant of proportionality (unitless) and a number usually of order one. A real glacier does not match either of these simple cases, but the precise shape has little influence on the force that drives flow. At depth in any glacier, there is always a horizontal gradient of hydrostatic head proportional to $-\frac{\partial S}{\partial x} = \tan \alpha$, where S is the elevation of the ice surface and α is the surface slope. This means that a vertical column will always be pushed by a horizontal driving stress of magnitude $\tau_d = \rho g H \tan \alpha$, regardless of the bed slope. Gravity therefore always pushes a glacier horizontally, in the direction of the downward surface slope.

For Fig 2.2c where the glacier rests on a small bed slope β, and the surface is inclined at angle α, the driving force τ_d is balanced in part by the uphill basal drag such that

$$[\rho g H \sin \beta]\, \delta x - \rho g H \left[\frac{\partial H}{\partial x}\right] \delta x = f\tau_b \delta x. \qquad (2.9)$$

For small angles $\frac{\partial H}{\partial x} = \beta - \alpha$ and $\sin\beta = \beta$. Thus, reducing to

$$\tau_d \approx \rho g H \alpha \text{ and } \tau_b = f\tau_d. \qquad (2.10)$$

Therefore, provided that the slopes are small, τ_d is the same as for a parallel-sided slab or a flat bed, as long as α refers to the surface slope.

2.4.1 Isotropic Creep of Ice

Previous experiments (Glen, 1965) on the behavior of ice show that, at stresses during normal glacier flow (~ 50 to 150 kPa), the relation between a dominant shear stress τ and the corresponding shear strain rate follows the power law

$$\dot{\epsilon} = A\tau^n, \qquad (2.11)$$

where n (unitless), the creep exponent, is approximately constant. However, the creep parameter A (unitless) depends strongly on temperature, grain size and impurity level of material. This is known as Glen's Law. Through measurements performed using strain rates, the determined values of n range from 1.5 to 4.2 (Weertman 1973; Weertman 1983), with a mean of about 3. This is most consistent with field data, whereby analyses of glacier dynamics usually assume that n = 3. Such a high value for n means that glacier flow differs markedly from that of a Newtonian viscous fluid.

The state of stress in glaciers can be complex, with combined shear and normal stresses acting in all three dimensions. The creep relation given by Eq. 2.11 applies only to simple cases where one component of stress is applied. Assuming that ice is incompressible, isotropic and each strain rate component is assumed to be proportional to its corresponding deviatoric stress component

$$\dot{\epsilon}_{jk} = \lambda \tau_{jk}, \tag{2.12}$$

where λ is the proportionality. In isotropic ice, the effective viscosity does not depend on the strain orientation. Thus, λ has the same value for all x, y and z components, although it varies along the glacier depending on factors like stress and temperature. A creep relation for complex stress systems must connect quantities that describe the overall state of stress and strain rate. Nye (1953), proposed that the effective stress and strain rate follow the observed power-law behavior for ice (Eq. 2.11), so that

$$\dot{\epsilon}_{E} = A\, \tau_{E}{}^{n}, \tag{2.13}$$

where $\dot{\epsilon}_{E}$ and τ_{E} are the second invariants of $\dot{\epsilon}$ and τ_{E}. From Eq. 2.12 and 2.13, the strain rates depend on deviatoric stresses according to

$$\dot{\epsilon}_{jk} = \mathrm{A}\tau_{E}^{n-1}\tau_{jk}. \tag{2.14}$$

This is known as the generalized Glen's Law or the Nye-Glen Isotropic Law, the most commonly used creep relation for glacier ice.

2.5 Driving Stress Under Perfect Plasticity Assumption

When the surface of a glacier is assumed to be a smoothed mirror of the underlying bed (Oerlemans 2001), then the thickness of the ice is largely governed by its surface slope (steeper the surface corresponds the thinner the ice and vice versa). Moreover, if ideal plasticity of the ice is assumed, basal sliding can be neglected, and the glacier width is much larger (~ 10 times) than its ice thickness, meaning the ice thickness H depends on the slope α and basal shear stress τ_b according to

$$H = \tau_b \, (\rho g f \, sin \, \alpha), \tag{2.15}$$

where ρ is the density of the ice, g the acceleration due to gravity, and f is the factor which represents the shape of the cross section; specifically the ratio between the cross-sectional area of the glacier and its perimeter and is related to the friction of a real glacier with the valley walls. The value of 0.8 is typical for valley glaciers and can be smaller for other glacier types (Paterson 1994). The relation has two main implications i) the smaller the slope, the thicker the ice and ii) that thickness is increasingly sensitive to surface slope toward smaller values of slope. When Eq. 2.15 is used to calculate glacier thickness, τ_b must be derived by another means. While a constant value of 1 bar (105 Pa) often serves as a good starting point (Binder et al. 2009, Clarke et al. 2009), Haeberli and Hoelzle (1995) used the glacier-specific empirical relation proposed by Maisch and Haeberli (1982). The relation is based on the analysis of topographic parameters from previously existing late-glacial ice bodies (found to be rather similar in size and shape to today's glaciers) and thus based on real glacier beds. It relates τ to the elevation range Δh of a glacier using a quadratic regression to all data points such that

$$\tau = 0.005 + 1.598\Delta h - 0.435\Delta h^2. \tag{2.16}$$

2.6 Stokes Equations in Glaciology

The Stokes equations in glaciology are a simplified version of the Navier-Stokes equations, which are the general equations in computational fluid dynamics for simulating fluids like air or water. Combining the Glen's ice flow law (Eq 2.14) with the fundamental physical principles of conservation of momentum and mass gives the Stokes equations, which determine the velocity vector $\mathbf{u} = (u_x, u_y, u_z)$ and pressure P such that

$$-\nabla P + \nabla\left(\eta(\nabla\mathbf{u} + (\nabla\mathbf{u})^{\mathbf{T}})\right) + \rho\boldsymbol{g} = \mathbf{0} \tag{2.17a}$$

$$\boldsymbol{\nabla}.\mathbf{u} = \mathbf{0}\,, \tag{2.17b}$$

Where the density is denoted by ρ and g is the gravitational force. An additional equation for the temperature T is omitted here since this thesis is focused on the Stokes equations and describing the movement of the ice surface, where the temperature of ice is generally assumed to be constant. This also limits the flow rate factor (creep parameter) A as a constant. It shall be noted that the term 'Stokes equations' usually refers to the linear Stokes equations. In the case of a power law fluid, Eq. 2.17 along with Glen's law are sometimes called the p-Stokes equations, where p refers to the power law parameter equal to $1/n + 1$. In glaciology, Eq 17a and 17b are usually called the full Stokes equations, since approximate models neglecting a few stress components are common.

Ice sheet flow is not only a non-linear flow, it is also a free surface flow. The surface position, h, of the ice mass is given by the surface evolution equation described by Eq. 2.6. Here, the net accumulation of ice (snow) at the ice surface depends on climate data such as precipitation and surface air temperature. The velocity thus determines the ice surface, and the surface shape in turn influences the velocity. As the Stokes equations are stationary, the time evolution of the (isothermal) glacier or ice sheet is determined by the evolution of the surface.

2.7 Stokes equations and Glacier Mechanics

The glacier ice dynamics is completely represented by the Stokes equation which includes all components of the stress tensor acting on the glacier. These nine principle stress components, including longitudinal (stretching and compressional) and transverse stresses (such as drag against the valley sides), are shown in Figure 2.3.

The full-Stokes model considers the three laws as follows:

a. Conservation of Mass,
b. Conservation of linear momentum, and
c. Conservation of angular momentum.

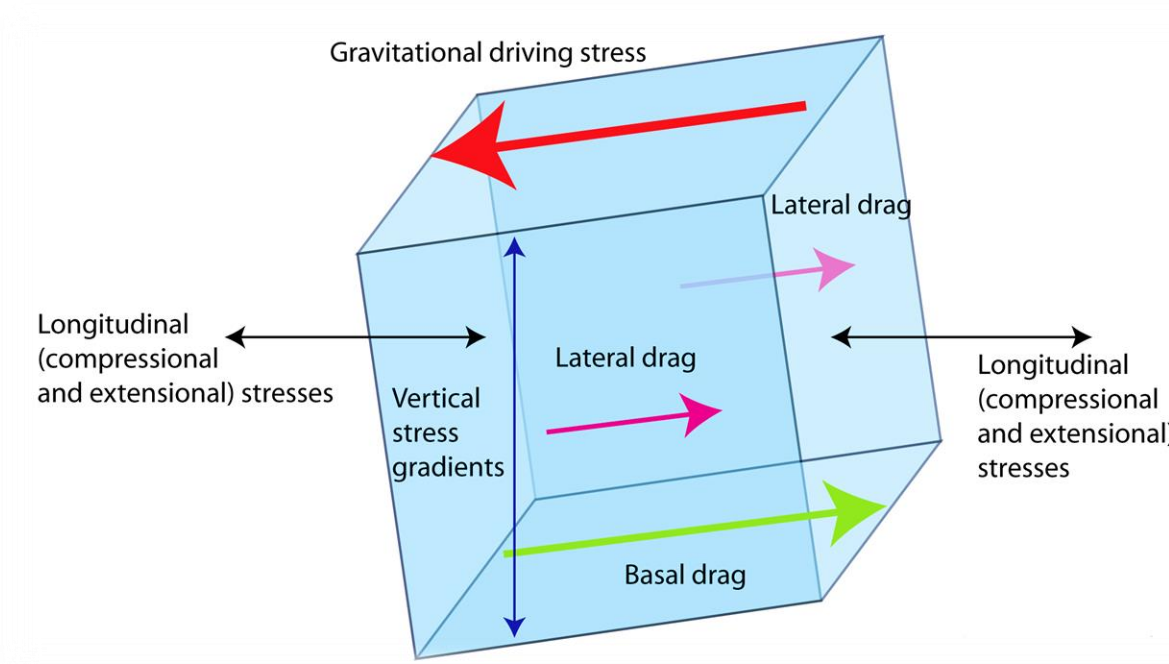

Figure 2.3 Schematic showing the different stress components acting on a small piece of glacier ice (Source: AntarcticGlaciers.com).

If the conservation of mass and momentum is represented in terms of velocity components, and the glacier ice is assumed to be incompressible, then the full-Stokes equations can be expressed as

$$\frac{\partial P}{\partial x} - \frac{\partial}{\partial x}\left(2\eta \frac{\partial u}{\partial x}\right) - \frac{\partial}{\partial y}\left(\eta\left(\frac{\partial u}{\partial y} + \frac{\partial v}{\partial x}\right)\right) - \frac{\partial}{\partial z}\left(\eta\left(\frac{\partial u}{\partial z} + \frac{\partial w}{\partial x}\right)\right) = 0 \qquad (2.18)$$

$$\frac{\partial P}{\partial y} - \frac{\partial}{\partial x}\left(\eta\left(\frac{\partial v}{\partial x} + \frac{\partial u}{\partial y}\right)\right) - \frac{\partial}{\partial y}\left(2\eta \frac{\partial v}{\partial y}\right) - \frac{\partial}{\partial z}\left(\eta\left(\frac{\partial v}{\partial z} + \frac{\partial w}{\partial z}\right)\right) = 0 \qquad (2.19)$$

$$\frac{\partial P}{\partial z} - \frac{\partial}{\partial x}\left(\eta\left(\frac{\partial w}{\partial x} + \frac{\partial u}{\partial z}\right)\right) - \frac{\partial}{\partial y}\left(\eta\left(\frac{\partial w}{\partial y} + \frac{\partial v}{\partial z}\right)\right) - \frac{\partial}{\partial z}\left(2\eta \frac{\partial w}{\partial z}\right) = -\rho g \qquad (2.20)$$

$$\frac{\partial u}{\partial x} + \frac{\partial v}{\partial y} + \frac{\partial w}{\partial z} = 0, \qquad (2.21)$$

where *u*, *v*, *w* represents the velocity along the *x*, *y*, and *z* directions, respectively. η is the viscosity, ρ is the density of ice, g the gravitational acceleration, and *P* denotes the pressure acting on the glacier at a particular location. Moreover, *x* represnts the direction along the glacier length, y represnts the direction across the glacier, and z represent the vertical direction. Observations by Glen (1952) suggest that the viscosity depends on temperature and effective strain rate. Due to the velocity dependence of the viscosity, the Full Stokes equations are highly non-linear.

From the modelling perspective, a full-Stokes based model is an accurate differential equation model that includes all the relevant ice flow dynamics. Such a model is considered to be the most accurate available, capable of describing highly dynamic ice sheets, including ice streams, ice shelves, and grounding line migration. Solutions obtained with full-Stokes models often agree well with data wherever available, or can be used in inverse models to identify unknown boundary conditions such as sliding parameters (Isaac et al., 2015). However, their application to evolution over large domains and for long time intervals is not yet possible, because their high level of physical model accuracy requires substantial computational resources (time and memory). For large scale simulations, high computational requirements restrict the application of these models to smaller timescale and glaciers sizes. To model the ice sheet behavior on longer timescales, approximations to the full-Stokes model are used. The equations listed above represent the ice sheet dynamics and can be applied to mountain/valley type glaciers by certain assumptions/modifications in the existing equations for ice sheet modelling. Considering that a mountain/valley type glacier as a simplified form of an ice sheet which has negligible width to thickness ratio, the equations are modified to represent mountain/valley type glaciers by neglecting the different types of stresses such as longitudinal, transverse and the vertical stress components.

2.8 Shallow Ice Approximation

The Shallow Ice Approximation (SIA), better known as the simplified version of the full stokes equations, can be derived if the stress tensor along the y and z direction is ignored. This gives the relation

$$\frac{\partial P}{\partial x} - \frac{\partial}{\partial z}\left(\eta\left(\frac{\partial u}{\partial z} + \frac{\partial w}{\partial x}\right)\right) = 0 \quad \text{and} \tag{2.22}$$

$$\frac{\partial P}{\partial z} = -\rho g\ . \tag{2.23}$$

"Shallowness" in the SIA refers to the assumption that the depth to width ratio of a glacier is small in glaciology. The SIA is the simplest approximation of the full-Stokes equations that is commonly used in glacier modelling approaches. The assumption made here is that shear stress at the glacier base is purely balanced by the driving stress due to gravity. Out of all the stresses acting on the glacier/ice mass it considers only one stress, that is, the basal shear stress. Another assumption is that the longitudinal stress is negligible. Due to neglecting the longitudinal stress, the accuracy of the SIA decreases when the contribution of basal slip to ice velocity increases.

2.9 Chapter Summary

This chapter has presented a brief overview of the principles and laws involved in modelling glaciers. A wide range of processes such as glacier mass balance and ice flow have been covered here, representing different aspects of glacier dynamics. Subsequently, the Stokes equations have been presented, being a complex representation of glacial processes that includes all the other listed processes. The concepts presented here are crucial to the formulation of the proposed ice thickness modelling framework in this thesis. Moreover, the underlying simplifications mentioned during the mathematical formulation of these real-world processes gives an idea of the implications when implementing these. The chapter ends with the shallow ice approximation which is the basis of the majority of the ice thickness models present. As a way forward, in chapter 3, the state of art review of approaches to glacier ice thickness modelling are presented, being essentially built upon single or a combination of the concepts presented in this chapter. Thus, this chapter will help in identifying the underlying strengths and limitations of each approach.

CHAPTER 3

3 LITERATURE REVIEW

This research aims to design and develop a remote sensing based distributed glacier ice thickness model for data scarce regions where no in-situ measurements are available. This chapter reviews the state-of-the-art in remote-sensing-based glacier ice thickness estimation and remote-sensing-based glacier surface velocity estimation, being two major components of this thesis. The chapter is organized such that the focus on the specific objectives of this thesis is maintained. The first two sections present an exhaustive set of studies categorized based on model complexity, followed by implementation schemes catering to the challenges commonly incurred in the field of glaciology.

3.1 Approaches to Modelling Glacier Ice Thickness

The ice thickness distribution of a glacier, ice cap, or ice sheet is a fundamental parameter for many glaciological applications (Farinotti et al., 2009). It determines the total volume of the ice body, which is crucial to quantify water availability or sea-level change and provides the link between surface and subglacial topography, which is a prerequisite for ice-flow modelling studies (Farinotti et al., 2017). Despite this importance, knowledge about the ice thickness of glaciers and ice caps around the globe is limited which is mainly due to the difficulties in measuring ice thickness directly.

To overcome this problem, several approaches have been developed to infer the ice thickness distribution. This section is dedicated to a discussion on the available approaches for glacier ice thickness modelling at different level of modelling complexity.

3.1.1 Full-Stokes based Approaches

The approaches to glacier/ice sheet modelling based on Stokes equation (here after referred to as full-stokes) provide the best possible description for complex fluids such as ice. Initially developed to solve ice sheet simulation processes, it was then evolved to accommodate glacier modelling as well. Elaborate studies using the Stokes equation have simulated various characteristics of glaciers (ice sheets), including ice velocity (Duan et al., 2012; Zhang et al., 2013; Wu et al., 2020), evolution of glacier characteristics such as length, ice-thickness, and volume (Duan et al., 2012, Ren and Leslie, 2011), mass balance (Carr et al., 2007, Jarosch et al., 2013), ice temperature (Zhang et al., 2013, Zhen et al., 2016), glacier hydrology (Pattyn et al., 2009, Denis et al., 2010), basal sliding (Zmitrowicz, 2003) and glacier surge (De Paoli and Flowers., 2009; Dunse et al., 2011; Flowers et al., 2011).

The basic constituents of an ice flow model following physical principles such as conservation laws (mass, momentum, energy) is shown in Figure 3.1**.** At the ice/atmosphere interface, a mass balance and/or energy exchange function as well as the stress values are prescribed. The mass balance is either directly measured in the field or reconstructed from meteorological data which is a systematic representation of local climate using regional climate models. Boundary conditions are prescribed under various forms at the limit of the domain i.e. at the glacier boundary. The initial conditions include a specific rheology for the ice, initial ice-thickness, and bedrock topographies. Solving the ensuing system of equations yields either the glacier geometrical characteristics (such as thickness, extent etc.) through time, or some specific fields at a given time like velocity or stress throughout the domain. Implementation of these modelling approaches for ice masses of complicated shape requires numerical methods such as finite element methods (Zienkiewicz, 1971).

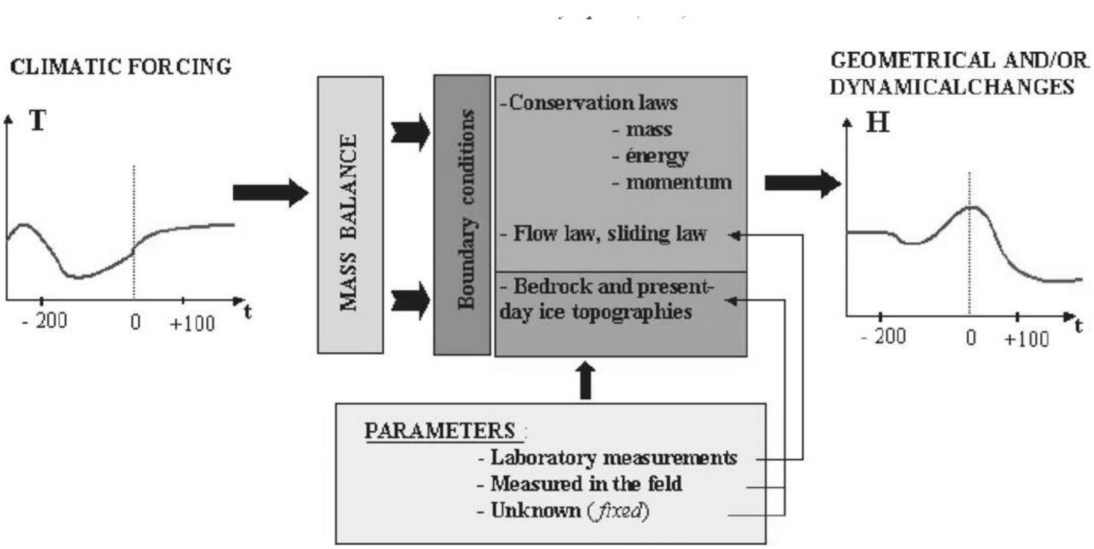

Figure 3.1 Flowchart depicting different components of a general ice flow model (Le Meur et al., 2004).

The boundary conditions represent the geological, hydrological and thermal conditions of a glacier. The required boundary conditions for the based problems in glaciology can be divided into two categories: upper and lower boundary conditions. Both include the surface elevation, ice mass velocity, thermal properties of ice, and viscosity at the glacier boundary. A common approach for modelling alpine glaciers is to synthesize the lower boundary condition using a Weertman-type sliding law (Weertman, 1964) in which the basal sliding velocity is proportional to basal drag (for example Le Meur and Vincent, 2003; Jouvet et al., 2011). The calculation of basal drag which corresponds to the sum of all basal resistive forces (Van der Veen and Whillans, 1989) is facilitated by numerical approximations.

The viscous properties of the glacier ice are mainly temperature dependent and thus modelled using a thermodynamic model of ice (glacier or ice sheet) to calculate its value. This thermal equation is derived from the energy conservation equation and includes conduction and advection in three-dimensional space. This problem is solved using Finite Element Methods (FEMs) such as the Streamline Upwind Petrov-Galerkin (SUPG) method (Gresho and Sani, 2000a). Numerical solutions of the complete full-stokes equations are commonly obtained using the finite element method based on the code Elmer (http://www.csc.fi/elmer).

Important ice sheet characteristics such as ice thickness, surface elevation or surface velocity are most efficiently derived from instruments operating at different spatial resolutions and deployed at different timestamps (Morlighem et al., 2011). However, their combined use into the modelling approaches generally complicates the application where the available data sets derived from airborne and satellite platforms operating at different spatial resolution are not consistent with one another.

The full-stokes ice flow models facilitate a non-steady-state assumption and work in a transient mode. These models can be effectively applied for complex modelling at high spatial resolution. Studies show that these models provide detailed understanding of every aspect of glacial processes and a more realistic picture of underlying processes. However, its application is limited to only a few glaciers due to both the inputs required and the complexity of the modelling process. Moreover, they require boundary conditions which are often not available for inaccessible glaciers. The limited number of full-stokes based studies in glacier modelling expresses the underlying challenges for model implementation.

3.1.2 Higher order approaches

Comparatively simpler versions of the full-stokes models have been developed, also known as higher-order (HO) models. These models can be broadly categorised as:

1) Blatter-Pattyn's (BP) higher-order model (Pattyn, 2003), and
2) MacAyeal's shelfy-stream model or Shallow Shelf Approximation (SSA) model (MacAyeal, 1989).

Zekollari et al., (2013) used a finite difference approximation based on Blatter/Pattyn type (Blatter, 1995; Pattyn, 2003; Furst et al., 2011). It solves for 3D momentum balance according to the Multilayer Longitudinal Stresses approximation (Hindmarsh, 2004). The model includes longitudinal as well as transverse stress gradients. In contrast to the full-stokes models, the HO solution assumes cryostatic equilibrium in the vertical direction and neglects the resistive stresses along the vertical direction. The model solves only for the horizontal component of velocity under the assumption that horizontal gradients of the vertical velocity are small with respect to the vertical gradient of the horizontal velocity. This HO model is found to be accurate only to first order. Accordingly, it does not resolve the intricate details of the flow pattern at higher horizontal resolutions. However, the discretization scheme used here makes extensive use of information on varied grid points (Furst et al., 2011). Even though model inputs were used at a spatial resolution of 25m for a good numerical convergence, it was suggested that results should be interpreted at a lower horizontal resolution of 100–200 m. In addition, a final smoothing of this field was required to follow with the approximations underlying the flow model. Importantly, Morlinghem et al., (2010), through implementation of higher order models for Pine Island Glacier, suggested that full-stokes is not required everywhere to model ice sheet flow or ice shelf flow.

3.1.3 Shallow Ice Approximation based Approaches

Recently, the number of ice thickness estimation approaches has increased at a fast pace. Pertaining to modelling simplicity of the Shallow Ice Approximation (SIA), this category of approaches has become dominant over the last few years.

Existing studies show that even though full-Stokes and higher order models are useful for detailed investigation of different aspects of glaciers and ice sheets, they are limited to individual glaciers. Moreover, studies on the grounding zone of large ice shelves have revealed that for small basal motion the width of the transition zone is of the same order of magnitude as the ice thickness, so that the grounding zone is reduced to a grounding line and the shallow-ice approximation still holds, provided that there is no passive grounding of the ice shelf. A full derivation of the Stokes balance equations is not necessary; it suffices to calculate the longitudinal stress deviator along the grounding line and prescribe a longitudinal stress gradient (Van der Veen, 1987).

The SIA based approaches can be divided into several categories based on the basic principles adopted in individual models and on the nature of inputs. These approaches include data such as surface velocities and mass balance (for example Morlighem et al., 2011; McNabb et al., 2012; Clarke et al., 2013; Farinotti et al., 2009; Huss and Farinotti, 2012; Gantayat et al., 2014; Brinkerhoff et al., 2016), as well as approaches that make use of iterative and relatively more complex forward models of ice flow (for example van Pelt et al., 2013; Michel et al., 2013, 2014), or statistical methods based on neural networks (Clarke et al., 2009; Haq et al., 2014). These approaches are discussed categorically by highlighting their key features, scope of improvement and limitations from their application perspective.

3.1.3.1 Mass-conservation based Approaches

Early approaches that consider mass conservation and ice flow dynamics go back to Budd and Allison (1975) and Rasmussen (1988) which were later further developed by Fastook et al., (1995) and Farinotti et al., (2009b). Farinotti et al., (2009) proposed an approach to calculate glacier ice thickness distribution by calculating ice balance fluxes through cross profiles along the glacier and applying the flow law of Glen (1955). A limitation of the approach is the time-consuming preparation of the input-data, as central flow lines (Linsbauer et al., 2012) or catchment areas for each glacier branch (Farinotti et al., 2009) need to be digitized manually. Moreover, the apparent mass balance was parametrized using long term field-based mass balance data collected for Alps glaciers. Thus, the availability of apparent mass balance data hinders its implementation where mass balance studies have not been carried out. It is thus necessary to explore alternative way to get apparent mass balance data.

This approach was successively extended by Huss and Farinotti (2012), who presented the first estimate for the ice thickness distribution of every single glacier on Earth by first providing distributed ice thickness for all the glaciers listed in Randolph Glacier Inventory (RGI) 2.0. Conversely, alternative methods based on more rigorous inverse modelling of glacier ice flow have often focused on inferring additional properties at the glacier base, besides ice thickness (for example Raymond-Pralong and Gudmundsson, 2011; Mosbeux et al., 2016).

Morlighem et al., (2011) adopted a new approach to obtaining a high resolution map of ice thickness by combining sparse ice thickness data collected by airborne radar sounding profilers and high resolution ice velocity derived from Interferometric Synthetic Aperture Radar (InSAR). One of the aims was to present an alternative to the traditional mapping of ice thickness with kriging, which has some serious limitations for ice sheet applications. Following the mass conservation law that conserves mass and minimizes the departure from observations. This approach was applied to the case of Nioghalvfjerdsfjorden Glacier, a major outlet glacier in northeast Greenland that has been relatively stable in recent decades. The final interpolated data showed high accuracy and found to be lying within 5% of the original data. These thickness maps can be directly used in high spatial-resolution, higher-order ice flow models. It has proven to be most effective for ice sheet models containing fast flowing regions. The technique however requires information on apparent mass balance data, and dense measurements of ice velocity in addition to radar based ice thickness data which makes it complex and limits its applicability to inaccessible and slow moving glaciers (such as valley type glaciers in Himalaya). Moreover, ice sheet characteristics such as ice thickness, surface elevation or surface velocity are most efficiently derived from airborne and satellite platforms carrying instruments operating at different spatial resolutions and at different time. Consequently, data sets are not always consistent with one another which may complicate their combined use in numerical ice sheet models.

Mcnabb et al., (2012) presented a method, based on conservation of mass, for estimating spatially distributed glacier ice thickness and bed topography. The method requires several input data such as DEM, surface velocities, surface mass-balance rates, rate of surface elevation change, and ice thickness at the boundary of the area of interest. Using this method, they presented a high-resolution bed topography map for Columbia Glacier. The mean difference between measured and calculated ice thickness observed was found to be good i.e. 5m, and with an RMSE of 44m. However, the required model inputs limits the method applicability to certain glaciers where those data have been collected.

Clarke et al., (2013) independently implemented the Farinotti et al., (2009) approach by considering ice thickness estimation as an optimization problem. The final ice thickness estimate calculation was preceded by delineation of the ice flow drainage basin which was performed manually. Applied to the western Canadian Glaciers, model validation included field measurement of surface elevation change between 1985–99 (Schiefer et al., 2007) to incorporate the ice thickness changes that have occurred between the measurement and the estimation date. However, due to limitations with the available dataset, they have applied less accurate and more coarsely resolved elevation dependent estimates (Schiefer et al., 2007) to obtain the ice thickness change correction.

Recently, Furst et al., (2017) presented a two-step approach to ice thickness estimation which is based on Elmer/Ice (Gagliardini et al., 2013) and mass conservation (Morlighem et al., 2011). In both steps, the observed ice thickness was used to constrain the estimates. The study presented ice thickness estimates as well as an error map calculated using error propagation (of inputs) for the Svalbard Glaciers. The error estimates show an aggregate uncertainty of at least 25 % in the reconstructed ice thickness for glaciers with very sparse or no observations.

The surface mass balance (SMB) field is one of the prerequisites for mass conservation approaches. Moreover, it is not directly measurable via remote sensing methods. The field measured SMB, which is generally sparse, can be used to determine elevation changes that are extrapolated using a local Digital Elevation Model (DEM)(Farinotti et al., 2009). Alternatively, the field measured SMB are exploited to validate parametric SMB approaches (Möller et al., 2016).

Efforts have been made towards using ice velocity (usually field based velocity measurements) to infer ice thickness. Rasmussen (1988) used this approach on Columbia Glacier using a finite difference scheme. Fastook et al., (1995) used a fourth-degree polynomial derived from the Shallow Ice Approximation (SIA) to calculate the ice thickness of Jakobshavn Isbræ, in West Greenland. Warner and Budd (2000) employed the SIA to calculate the ice thickness over the Antarctic Ice Sheet using mass flux conservation. Farinotti et al., (2009) employed a method derived from the same principle, to determine the ice volume of Swiss alpine glaciers. All these studies, however, suffered from significant deviations from the original thickness data, i.e., by hundreds of meters (Fastook et al., 1995; Warner and Budd, 2000), and an average of 25% of mean ice thickness (Farinotti et al., 2009).

3.1.3.2 Shear-stress based approaches

The shear-stress based approaches are a class of approaches that rely on simple empirical relationships between shear stress and the glacier ice thickness. Nye (1952), noted that for the case of an idealized glacier of infinite width, ice thickness can be calculated from the surface slope using estimates of basal shear stress and assuming perfect plastic behaviour. Nye (1965) successively extended these considerations to valley glaciers of idealized shapes. Later Li et al., (2012) additionally accounted for the effect of side drag from the glacier margins.

Haeberli and Hoelzle (1995) first suggested that shear stress can be estimated from the glacier elevation range, with the corresponding parameterization used in a series of recent studies (for example Paul and Linsbauer, 2011; Linsbauer et al., 2012; Frey et al., 2014; Ramsankaran et al., 2018). Common to these approaches is the assumption of a constant basal shear stress.

Linsbauer et al., (2009) generated hydrologically consistent DEMs (using Topogrid) from elevation contours/points and other vector data (Hutchinson, 1989), resulting in concave-shaped landforms. Such results mimic the typical parabolic shape of glacier beds without explicitly considering mass fluxes.

Frey et al., (2014) compared the ice thicknesses derived from with GlabTop2 and the HF-model to 86 local point ice thicknesses estimates derived from GPR measurements across six glaciers in the Himalaya-Karakoram (HK) region. The average differences between the models and the measurements was 25.7m for GlabTop2 and 19.0 m for the HF-model; the RMSE of all validation points were observed to be similar for both Glaptop2 and the HF-method. The negative mean differences indicate an underestimation of the ice thicknesses by both models, which to a certain extent is caused by glacier changes between the dates of the measurements and the acquisition dates of the DEM and the glacier outlines used by the models. The errors and artifacts in the input data and simplifications and parameterizations in the models might also account for the differences. In addition, uncertainties related to the measurements (resolution, interpretation, and spatial reference of GPR data) and their digitalization influence the results of the validation. Another factor leading to differences between measured and modelled ice thicknesses is the comparison of local ice-thickness measurements with model results on a 90m grid, which can cause large differences, particularly at the steep margins of glacier beds.

There exist general sources of uncertainties in both of the approaches due to the level of accuracy of glacier outlines and the DEM used. These input data uncertainties affect the results of each method. When compared against field measurements which were available for only a few study glaciers, locally large differences were noted. However, in some cases these model approaches (GlabTop2 and HF) agree in terms of trend but exhibit large difference to the measured ice-thicknesses. The average difference between GlabTop2 and the HF-model for the 86 validation points was −6.6m or −4.1% with a standard deviation of 41 m. Huss and Farinotti, (2012) suggest that approaches which take the three-dimensional shape of the glacier surface into account can be considered as superior.

3.1.3.3 Velocity based approaches

This category of approaches are based on the integrated form of Glen's ice flow law (Glen, 1955). To estimate ice thickness h, the flow law can be represented as

$$\mathrm{h} = \frac{n+1}{2\mathrm{A}} \frac{u_{\mathrm{s}} - u_{\mathrm{b}}}{\tau^{n}} , \tag{3.1}$$

where u_s and u_b are the surface and basal ice flow velocities respectively, or to replace q in the mass continuity equation with the depth averaged profile velocity u (since q = uh). In these cases, an assumption relating u_s to u_b or u is required because u_b is an unknown quantity and cannot be measured directly. This approach has been implemented by few studies over Gangotri Glacier, India (Gantayat et al., 2014) and over 13 selected glaciers worldwide

(Farinotti et al., 2017). Though a simple approach, these methods cannot be used for glacier evolution investigations.

3.1.3.4 Neural Network based Approaches

As implied by the name this class of approaches utilise an artificial neural network (ANN) to estimate the underlying glacier bedrock by training the network with the surrounding glacier free topography. These approaches were aimed to reduce the dependence on site-specific information during the modelling.

Clarke et al., (2009) applied this approach for the first time in the Mount Waddington area in British Columbia and Yukon, Canada. In this approach, the multi-layer feed forward ANN was used to transfer the characteristics of current ice-free glacier beds to present-day glaciers. This method yielded a plausible subglacial topography with a representative RMSE of ±70 m.

Haq et al., (2014) used additional topographical information such as slope and DEM along with an ANN to train the ice thickness model. This method was tested over the Gangotri Glacier located in the Indian Himalayas. However, due to non-availability of direct field measurements, this study does not provide errors in estimated ice thickness.

Though requiring limited inputs, these approaches are computationally intensive when applied to large glaciers (Clarke et al., 2009; Haq et al., 2014). Since the geological and environmental settings vary spatially, it logically follows that a neural network trained to estimate ice thickness in a particular geographical region may not perform well if applied to another region (Clarke et al., 2009).

3.1.3.5 Minimisation based approaches

Glacier ice thickness approaches that fall within this category consider the ice thickness estimation (via inversion) as a minimization problem. The minimization in the estimated ice thickness is achieved through defining a cost function that corrects for the difference between the estimated and observed quantity. The observable quantity here generally includes surface elevation (Leclercq et al., 2012; Michel et al., 2013; Van Pelt et al., 2013), which can be obtained from a DEM derived from either optical or SAR imagery. Additional constraints such as zero ice thickness outside the glacier boundaries and if available, surface flow velocities, are used in inversion of bed rock estimations. Starting with an initial guess, a forward model for glacier ice flow is then used to predict the target quantity. The difference between estimates and observations is utilised to further update the estimates, which is repeated iteratively to achieve minimal deviation from the observation. The forward model generally considers mass conservation (Farinotti et al., 2017; Furst et al., 2017) and often relies on a higher-order representation of ice dynamics (for example Gagliardini et al., 2013).

3.1.3.6 Estimating spatially distributed ice thickness

Vital to model performance and accuracy is the approach to modelling and the implementation technique to generate spatially distributed ice thickness (McNabb et al., 2012). Unlike the full-Stokes or higher order modelling approaches which provide grid-wise ice thickness, a majority of SIA based approaches have presented a spatially distributed ice thickness map by extrapolating/interpolating the modelled ice thickness. This is accomplished by generating spatially distributed ice thickness from the estimated ice thickness central flowline (Farinotti et al., 2009; Morlingham et al., 2011; Brinkerhoff et al., 2016), adjacent flowlines (McNabb et al., 2012) or interpolation of few selected points over the glacier (Frey et al., 2014; Ramsankaran et al., 2018). This simplifies and reduces the computing time of the modelling approaches. Also, considering that the SIA based estimations are more likely to be accurate near the central flowline of the glacier (Cuffey and Patterson, 2004), where longitudinal stresses are dominant, it is reasonable to generate spatially distributed ice thickness starting from the central flowlines.

3.1.3.7 Glacier ice thickness estimation at large scale

The above-mentioned approaches based on the SIA, when implemented for large scale, involve a variety of implementation level changes to get a simplified version of the individual existing models. These changes involve change in parameterization technique or some additional assumptions.

Huss and Farinotti (2012) presented the first global estimated volume and thickness distribution of all glaciers worldwide following RGI 2.0. By combining glacier outlines with digital elevation models, they calculated glacier-specific distributed thickness based on an inversion of surface topography using the principles of flow dynamics. Extending the approach presented earlier by Farinotti et al., (2009), where the parameterization of mass balance gradient using long term mass balance data of Swiss glaciers, the parameterization additionally included continentality index (which describes mass balance distribution based on the closeness to the sea or a continent) of each glacier. This continentality index is calculated using relations between geographical latitude and a reference equilibrium line altitude (ELA). Climatic inputs such as air temperature was taken from NCEP reanalysis data, which could contribute to uncertainties.

Frey et al., (2014) estimated glacier ice thickness and volume for the complete glacier inventory (RGI 4.0) of the 28,000 glaciers in the Himalaya Karakoram region (containing glacier coverage of ~40,775 km^2), over the period 2000–2010. One volume-area scaling based approach and two spatially distributed models (GlabTop2 and Huss and Farinotti, 2012) were used to estimate the ice thickness and volume. However, the volume-area scaling approach was used to estimate mean ice thickness and volume because of its lumped type model approach. For the GlabTop2 model a constant shape factor parameter was used for all of the glaciers whereas for Huss and Farinotti (2012) no changes in model implementation were carried out. Due to limited information available for the Himalaya Karakoram region, the obtained results were validated with ice thickness measurements available for only six glaciers.

Helfricht et al., (2019) presented a calibrated ice thickness model for glaciers in the Austrian Alps. It was based on the model presented by Huss and Farinotti (2012). The field data of three glaciers were used to calibrate the ice thickness model to provide improved ice thickness data. The obtained optimal model parameters through calibration were applied on a regional scale to derive an up-to-date glacier ice volume estimate for Austria. Through cross-validation between modelled and measured point ice thickness measurements, model uncertainty of 25–31% of the measured point ice thickness was estimated. Comparison of the modelled and measured average glacier ice thickness revealed an underestimation of 5% with a mean standard deviation of 15% for the glaciers with calibration data.

Farinotti et al., (2019) presented a consensus of estimated ice thickness and volume of 220,000 glaciers around the world by consolidating five different model estimates. An ensemble of estimated ice thickness was generated for all the study glaciers around the world. All five models were implemented with modifications.

- Model 1 (HF Model): Based on Huss and Farinotti (2012) was calibrated to the available ice thickness measurements by optimizing parameters specific to each RGI region. No model tuning was performed to reproduce ice thickness observations of individual glaciers.
- Model 2 (GlabTop2): Based on Frey et al., (2014) was empirically derived via a cross-validation experiment that utilised field measurements.
- Model 3 (OGGM): Based on Farinotti et al., (2009) but based on gridded climate data (Harris et al., 2014) to estimate the mass balance and not on linear mass balance gradient. The parameter calibration was performed for two parameters (ice thickness interpolation parameters and creep parameter) with the others kept constant and the same set of parameters used globally.
- Model 4: Based on Furst et al., (2017) but only the calibration using ice thickness was performed by skipping the calibration for velocity. This was due to the input constrained design of this study. Moreover, the required information on surface mass balance (SMB) for each glacier was taken from the Global Glacier Evolution Model (Huss and Hock, 2015). The long term averaged SMB was interpolated and carried out separately for land terminating and marine terminating glaciers.
- Model 5 (GlabTop2 IITB version): Based on Ramsankaran et al., (2018). Due to no direct ice thickness observations available for the study region, a set of 31 simulations were performed by varying the shape factor parameter in the interval from 0.6 to 0.9 with an interval of 0.01. An average of these 31 simulations was taken as the final estimated ice thickness.

3.1.4 Summary of Ice Thickness Modelling Approaches and Challenges

This section presents a summary of the current efforts and challenges to estimate the glacier ice thickness using remotely sensed information. The afore mentioned studies on ice thickness modelling approaches give a significant insight to the expectations in the quality of ice thickness estimates as and when the nature of inputs vary. Though a variety of approaches based on different model complexities exist, the prevailing large number of studies based on the SIA category models show a potential for simple and efficient application.

Particularly for SIA based approaches, a variety of existing modelling approaches for glacier ice thickness estimation has been discussed. Since these models have been designed and tested for a different study area and different input data, a common platform to make a detailed comparison among these is needed. In this context, the Working Group on glacier ice thickness estimation has initiated the Ice Thickness Models Intercomparison eXperiment (ITMIX). So far, this experiment has conducted a coordinated comparison between existing models capable of estimating the ice thickness distribution of glaciers and ice caps using surface characteristics (Farinotti et al., 2017). The accuracy of individual approaches was assessed in a unified manner, along with the strengths and shortcomings of individual models. However, availability of consistent input data remains a challenge, having large temporal differences. Additionally, the data used for validation were provided by different independent groups, and so the underlying uncertainty could not be standardized for the study. Table 3.1 lists the details of the studies carried out using the modelling approaches falling under SIA. In the case of multi input based modelling approaches (such as McNabb et al., 2012) further problem emerged. The greater the number of inputs, the greater the temporal differences between them which leads to uncertainty in the estimates due to inconsistent timestamps of the input data. This was majorly due to limited temporal coverage of available remote sensing data.

When analysed with respect to observed ice thickness measurements for the 21 selected glaciers around the world. Large variations in the modelled estimates were observed at individual level. However, models within the same category showed the same trend. This seems reasonable for the minimization approaches which are based on diverse forward models or for the mass conserving approaches and velocity based approaches which differ significantly due to varying implementation schemes. The same was observed for shear-stress-based approaches particularly due to prominent differences in estimates for ice caps.

Importantly, it was found that the average solution matched the field measurements well for most of the study glaciers, with an average deviation of less than 10 %. This increase in prediction accuracy is expected for an unbiased model ensemble. However, generating an ensemble of model estimates is an unrealistic approach for frequent monitoring and for operational purposes.

The studies mentioned in the previous sections also represent the challenges in modelling of ice thickness with limitations in the in-situ data available. Considering the current situation of available data, the challenges posed to glacier modellers include:

- Limited data for validation: The existing measurements of ice thickness are few and their usefulness for testing the ice thickness estimation method still remains an open ended question. For ice-thickness measurements, a standardised, open-access database has been launched (Gärtner-Roer et al., 2014), and its gradual growth already justified an updated release. Despite this international effort, many thickness measurements remain unpublished. For example, ice thickness measurements of the Himalayan glaciers, which are considered as the third pole, are not available in the freely accessible glacier thickness database (GlaThiDa).
- Spatial distribution of the available datasets: Existing knowledge of the actual ice thickness is also limited with respect to spatial coverage over the individual glaciers. Following the freely accessible worldwide glacier ice thickness database (GärtnerRoer et al., 2014), only few glaciers are surveyed with full spatial coverage. Moreover, the majority of glaciers have field data available for only a few cross sections (less than 5) and these are located in the lower region of the glacier (ablation region).

  Temporal coverage of the available measurements: The existing measured ice thickness data also exhibits temporal limitations. The data is either collected at a single timestamp or it is collected over parts of the glaciers surveyed separately at different time periods. For example, field measurement for the Tasman glacier were collected in the early 1970s. This when combined with temporal constraints of available remote sensing datasets is a challenge to glacier modellers. When the timestamp of available ice thickness measurements does not coincide with the remote sensing data (such as synthetic aperture radar (SAR) and optical data) used for modelling, uncertainty is introduced in the modelled estimates.

Table 3.1 A list of some key studies distributed models available for glacier ice-thickness estimation based on SIA concepts.

Model Category	Study	Study Area	Model Inputs	Timestamp of input data used for modelling	Timestamp of observed data used for validation
Mass conservation approaches	Farinotti et al., (2009)	Alpine glaciers	DEM, OL	1929-2007	1990-2007
	Huss and Farinotti (2012)	All glaciers in RGI 2.0	DEM, OL	SRTM(2000) and ASTER*	1990,2003,2009
	Clarke et al., (2013)	Western Canadian Glaciers	DEM, OL, SMB, Vel	2005	1959-1960
	Morlighem et al., (2011)	Nioghalvfjerdsfjorden Glacier	DEM, OL, SMB, Vel	1996	1997, 1999, 2004 and 2010
	McNabb et al., (2012)	Columbia Glacier, Alaska	DEM, OL, H, Vel, $\frac{\partial h}{\partial t}$	1984–2011	2010
	Fürst et al., (2017)	Svalbard Glaciers	DEM, OL, SMB, Vel, $\frac{\partial h}{\partial t}$	1983–2013	1983–2013
Velocity based approaches	Gantayat et al., (2014)	Gangotri Glacier	DEM, OL,Vel	2009–2010	1971–1972
Perfect plasticity, shear-stress based approaches	Linsbauer et al., (2012)	All Swiss Glaciers	DEM, OL,FL	1985,1991, 1995	2003; 2006-2007; 1988-1998
	Frey et al., (2014)	Himalayan-Karakoram	DEM, OL	2000	2000–2009
	Ramsankaran et al., (2018)	Chhota Shigri Glacier	DEM, OL,Slope	2013	2009
	Haq et al., (2014)	Gangotri Glacier, India	DEM, OL	2010	Validated using other modelled estimates
	Brinkerhoff et al., (2016)	Storglaciären (Sweden), Synthetic glacier and Jakobshavn Isbræ Greenland Ice-sheet	DEM, OL, SMB, Vel, $\frac{\partial h}{\partial t}$	1958-2007	2009-2018

SMB- surface mass balance, **Vel-** Glacier surface velocity, **DEM-** Digital Elevation Model, **OL-** outline of glacier, **FL**- flowlines, $\frac{\partial h}{\partial t}$-Ice thickness change or equivalently surface elevation changes, **H-** Glacier ice thickness.

*ASTER DEM is generate using mosaic of multi temporal images so it does not represent any specific timestamp.

The mass balance and ice flow law based approaches are capable of modelling present and future evolution and thus are popularly applied. However, they suffer from complex parametrization or require ice thickness data. With the limited availability of field measurements, these approaches need to be fortified with remotely sensed observation at its best. Moreover, irrespective of the modelling approach used, the absence of accurate estimations of ice thickness over the entire surface of the glacier is the main constraint to accurately simulating future changes (for example, Beniston et al., 2018; Vuille et al., 2018). Apart from DEM which is readily available at global scale, the remotely sensed glacier surface velocity is one of the evolving fields for the researchers to create simple but effective approaches to glacier ice thickness estimation at large scale.

3.2 Approaches to Glacier Surface Velocity Estimation

Glacier velocity is one of the paramount variables that impacts glacier dynamics. Glacier velocity is of three types: surface velocity, sub-surface velocity and basal sliding velocity. Among these, surface velocity can be conveniently monitored using remote sensing technology. Moreover, glacier surface velocity at annual or decadal scale represents the overall stress regime of a glacier, which in turn is an indicator of its geometric characteristics like glacier ice thickness (Anderson et al., 2015). Thus, it is one of the important parameters that helps modelling glacier ice thickness and its evolution. Moreover, surface velocity can also distinguish active from inactive ice on debris-covered glaciers, identify glacier surge events, and even infer basal conditions. However, there remain challenges to routine monitoring of glacier surface velocity globally.

Existing approaches for glacier surface velocity monitoring include ground surveys, Synthetic Aperture Radar (SAR) Interferometric techniques and image matching techniques using optical or SAR imagery. The ground-based survey is the most accurate method but confines the measurements to limited parts of a glacier due to logistical reasons and can only be conducted during a specific time of year and when there are favourable weather conditions. The latter two techniques are discussed in the subsequent sections.

3.2.1 Synthetic Aperture Radar (SAR) Interferometric Techniques

Studies have shown the potential of the Interferometric SAR (InSAR) technique for glacier velocity estimation (Palmer et al., 2011; Kumar et al., 2011; Chae et al., 2017; Sánchez-Gámez and Navarro 2017). Though the precision of velocity estimation through InSAR can reach up to millimetres per day, its successful application is often limited by phase noise and large displacements over time (Pritchard et al., 2005; Joughin et al., 2010).

3.2.2 Image Matching Techniques

The image matching techniques for glacier velocity estimation are used to calculate the shift in a glacier and is derived from the best match between corresponding pairs of images. The criteria for matching can be different such as cross correlation and maximum likelihood.

The cross correlation based techniques come in different variants. The most commonly applied and simplest approach out of these is the normalized cross correlation (NCC), with the peak of the cross-correlation surface indicating the displacement between the images. The normalization of the cross-correlation works relatively better for images with different illumination conditions. Because this method operates in the spatial domain (as a convolution operation), the computation is high compared to computations in the frequency domain, and is easily affected by variability in digital numbers. This means that for NCC to perform better, both images must have same spread of digital numbers. This is a major drawback of the method for applications in glaciology. The glacier areas usually contain a variety of surface features such as dry snow, wet snow, debris and black rocks, which introduces large differences in digital numbers. This, when not met in the other image, can cause problems with the matching performance.

The cross-correlation can also be computed in the frequency domain using the convolution theorem where the Fourier transform of one image is multiplied with the complex conjugated Fourier transform of the second image (Heid and Kaab, 2012). Moreover, Fitch et al., (2002) developed a method called orientation correlation. Haug et al., (2010) showed that this method is well suited for deriving ice shelf velocities. The orientation images are calculated using signum function. These orientation images are then matched using cross-correlation operated in the frequency domain and phase correlation. The orientation correlation is found to be illumination invariant (Fitch et al., 2002) and the correlation is not affected by uniform areas.

Following Heisenberg's uncertainty principle, the frequency domain methods of all variants are expected to perform worse when compared to the spatial domain methods on small window sizes due to lower signal to noise ratio (Heid 2011). However, the small window sizes may in some cases be useful for measuring glacier displacements, especially for shear zones or where glaciers flow over barriers, and for small glaciers (Heid and Kaab, 2012).

The other category of image matching techniques is based on maximum likelihood (ML) criteria of matching. According to the definition of the ML motion estimation (Erten et al., 2009), the matching algorithm performance is directly obtained through maximizing the conditional density function (CDF) of two matched blocks. This matching results in a displacement vector representing the shift between the matched blocks. Here, blocks are obtained from two intensity SAR images Y and X of size $M \times N$ acquired over the same area at times t1 and t2.

From the remote sensing data perspective, both SAR and optical imagery can be utilized to carry out image matching techniques. Using SAR, the glacier velocity can be estimated by tracking the amplitude (Derauw, 1999; Strozzi et al., 2002b; Ciappa et al., 2010; Riveros et al., 2013), intensity (Ruan et al., 2013; Sanchez-Gamez and Navarro 2017; Yellala et al., 2019), speckle (Short and Gray 2005) or coherence (Strozzi et al., 2002) of the images. The SAR image pairs used in these studies have been either separated by a few days or a few months. Yellala et al., (2019) successfully demonstrated an application of SAR-based feature tracking using yearly SAR dataset. Likewise, optical images have also been used for glacier feature tracking by tracking the digital numbers that represent visual features spread over the glacier surface (Kaab et al., 2002; Scherler et al., 2008; Heid and Kaab, 2012; Messerli and Grinsted, 2015, Fahnestock et al., 2016). The use of optical images often suffers due to the presence of cloud cover over the glaciated regions. The studies using either SAR or optical data consider the correlation between two temporal images as a similarity measure to estimate the shift between images. Earlier, there were some improvements in the cross-correlation based glacier feature tracking using techniques like Particle Image Velocimetry (Patel et al.,

2019) and Thin Plate Spline (Ruan et al., 2013) to minimize the errors. Apart from the correlation, other similarity measures such as maximum likelihood have been used to study glacier flow using remote sensing data (Erten et al., 2009). Erten et al., (2009) and Deledalle et al., (2010) performed a comparative study to assess the accuracy of maximum likelihood based tracking with classical correlation based tracking and found the former to be the more robust approach.

A basic concern for any image matching based feature tracking algorithm, including the above-mentioned image matching based approaches is to determine an optimum window size for image matching. Particularly, the successful application of these methods strongly depends on the selected window size (Strozzi et al., 2002; Cai et al., 2017; Paul et al., 2017). Moreover, studies by Huang et al., (2011) and Turrin et al., (2013) have shown that use of a different window size in feature tracking leads to different velocity estimates for the same glacier. With an uncertain image matching window size, the velocity estimates have to be presented either at different window sizes (Huang and Li, 2011; Schubert et al., 2013; Chen et al., 2016) or at a window size which is calibrated using known glacier velocity information (Riveros et al., 2013). At present, calibration of window size is a challenge where no glacier velocity measurements are available. This may introduce a significant level of uncertainty in the remote sensing based glacier velocity estimation. Studies indicate sincere efforts towards automation of the feature tracking procedure with variable window sizes using iterative algorithms (Debella-Gilo and Kääb, 2012; Nagler et al., 2015; Euillades et al., 2016), with complex processing involving multiple datasets (Ahn and Howat, 2011) or focussing on the error reduction.

Recent study by Altena and Kaab (2020) implemented NCC using ensemble matching of repeat satellite images. Similarly, Li et al., (2021) proposed a cross-correlation stacking method by deriving offsets after averaging the NCC stack of a series of consecutive pairwise NCCs.

Studies based on glacier velocity estimates for a large region (for example, MEaSUREs) often misinterpret estimates for small glaciers due to globally selected window sizes that are usually too large for their dimensions. Glacier velocity estimates using very large window sizes (for example 256 x 256 pixels or 512 × 512 pixels) have generally performed well for large structures/features, but are not applicable to small (for example, ~ 500 m width) glaciers, nor do they provide information in textured zones such as shear zones (Strozzi et al., 2002; Paul et al., 2015).

3.2.3 Summary of Glacier Surface Velocity Estimation Techniques and Challenges

This section presents a summary of the current efforts and challenges to estimate the glacier surface velocity using remote sensing. It is shown through the studies on glacier velocity estimation techniques that development has reached saturation, whereby all the existing techniques suffer from similar limitations such as significant changes in the glacier surface over time affecting the estimation capability. However, less has been done in the direction of a glacier specific adaptive automation of the estimation techniques focussing on the glacier velocity estimation with no prior field observations available. Moreover, small glaciers should also be given proper consideration while estimating glacier velocity at large scale.

Like ice thickness measurements, the glacier surface velocity field measurements also suffer from problems such as scarcity (both in time and space) due to inaccessibility of glaciers. Most often, the discrete GPS measurements taken at installed stakes under sample the velocity field in a spatial sense (Voytenko et al., 2012). This hampers the detailed validation of estimated velocities.

3.3 Research and Knowledge Gaps

The freely accessible database of worldwide glacier thickness observations (Gärtner-Roer et al., 2014) and the modelling studies which use field measurement for validation show lack of a sufficient and consistent database. The sparse measurements from the field-based surveys for glacier ice thickness. The surveyed glaciers even suffer from uneven distribution of the collected data points. Very few glaciers are surveyed completely providing a glacier wide ice thickness measurement. Additionally, measured data is limited to one timestamp due to logistical reasons, making it difficult to undertake detailed model evaluation. Accordingly, this thesis will develop a purely-remote-sensing based , spatially distributed glacier ice thickness model.

CHAPTER 3

Based on the review of state of art approaches to glacier ice thickness estimation, it is evident that in spite of recent attempts to address this knowledge gaps, the findings still show high level of uncertainties. Moreover, the present techniques require improvement for applicability to data scarce regions. The research gaps which needs attention are summarized as follows:

1. There is a serious lack of in situ measurements and reliable modelled glacier ice thickness estimates, severely hampering the scientific knowledge about the state of glaciers especially Himalayan Glaciers (Bolch et al., 2012). This means that there is a need to monitor glaciers (both spatially and temporally) in order to contribute towards existing knowledge to have an accurate understanding of glacier evolution.
2. Empirical approaches like the volume-area (V-A) scaling method used in several studies worldwide seem to be fast and convenient but are not recommended for use on individual glaciers (Bahr et al., 2015). Therefore, to study glaciers at an individual level it is required to develop a model which has the capability to represent individual glaciers. Physical models based on mass conservation and ice flow laws provide better estimates of glacier ice thickness then empirical approaches, but they require either large set of inputs or complex set of parametrization using field measurements which are not available for inaccessible glaciers.
3. To find alternative ways to model glacier ice thickness and reduce the dependency on field observations, the focus needs to be on remote sensing based derivation of glacier processes such as glacier flow. The glacier surface velocity can be derived from remote sensing techniques however the identification of optimal window size remains dependent on the prior knowledge of glacier flow. Moreover, the spatial variation of glacier feature should be taken into account for a more realistic glacier velocity estimation. This has not been explored so far.
4. Temporal differences between modelled and observed ice thickness affects the reliability of model assessment. Though the limited temporal coverage of different remote sensing data is an inevitable challenge (for example, it is difficult to get optical, SAR imagery and DEM for the same time stamp), efforts should be made to incorporate the surface level changes occurring in between these temporal gaps.

5. Studies (Rasmussen 1988; Furst et al., 2017) have suggested that the field measured data can be useful to improve the ice thickness model estimations. Thus, thorough investigation need to be conducted to study the impact of the nature (spatial distribution as well as quantity) of the collected field data on a ice thickness estimation model.

3.4 Chapter Summary

This chapter provided an overview of the state-of-the-art in approaches to glacier ice thickness modelling as well as glacier surface velocity estimations. First, the approaches to ice thickness modelling were discussed with a special focus on the opportunities of the approaches towards a simple field-data-independent implementation. The model complexity, number of model inputs required, and limitations were also discussed. Additionally, model implementation techniques critical to model performance were highlighted. Second, progress in remotely sensed glacier velocity estimation techniques and their evolution through time were critically examined. The challenges in the existing approaches to velocity estimation for data scarce regions were highlighted and the opportunities to incorporate of new ways to automate the glacier surface velocity estimation was summarized. Accordingly, the developed algorithm for glacier surface velocity estimation is presented in chapter 5. Following this, chapter 6 describes the overall glacier ice thickness (which includes glacier velocity as one of the inputs) developed in this thesis.

CHAPTER 4

4 STUDY GLACIERS AND DATASET

This chapter presents the details of the study glaciers for which the glacier velocity estimation and ice thickness modelling was carried out in this thesis. The remote sensing as well as in-situ datasets used for the estimation, calibration and validation are also presented, corresponding to glacier surface velocity estimation in chapter 5 and ice thickness modelling in chapter 6. While a brief overview is given of all available data, field data collected specifically for validation of ice thickness modelling as part of the work in executing this thesis has been discussed in detail.

4.1 Study Glaciers

4.1.1 Location and Climate

The area under consideration for the proposed research includes different glaciers widely spread along different climatic regions. The glaciers that were selected to study the performance of the proposed glacier tracking algorithms are South Glacier, Patsio Glacier, Chhota Shigri glacier, and Tasman glacier (Figure 4.1). These glaciers also represent different debris cover (debris free glaciers to heavily debris covered) conditions as well as show a variety of sizes (glacier length of 3km to 30 km). Selecting glaciers of varying size also serves a purpose to efficiently test the developed method of window size estimation (more details in Chapter 5). Since previous studies on glacier velocity estimates for a large region (section 3.2.2) have shown that using very large window sizes have generally performed well for large structures/features but may not be applicable to small glaciers.

The South Glacier is located in the Donjek Range of the St Elias Mountains, southwest Yukon, Canada. It is a small surge-type glacier (Paoli and Flowers 2009) with reported surge events during early 2000. This glacier is influenced by sub-arctic continental climate.

The Patsio Glacier and Chhota Shigri Glacier are located in the Western Himalayas, India. The Patsio Glacier lies in the Bhaga River Basin while Chhota Shigri lies in the Chandra River Basin. Though both lie in the Western Himalayan region, Chhota Shigri Glacier, which is one of the bench mark glaciers of the Himalayas, has a different climate regime to that of the Patsio Glacier; one is situated on the northern slope of Pir-Panjal while the other is in the

Greater Himalayan region otherwise known as the extend region of Zanksar where the precipitation gradient differs from the Pir-Panjal region.

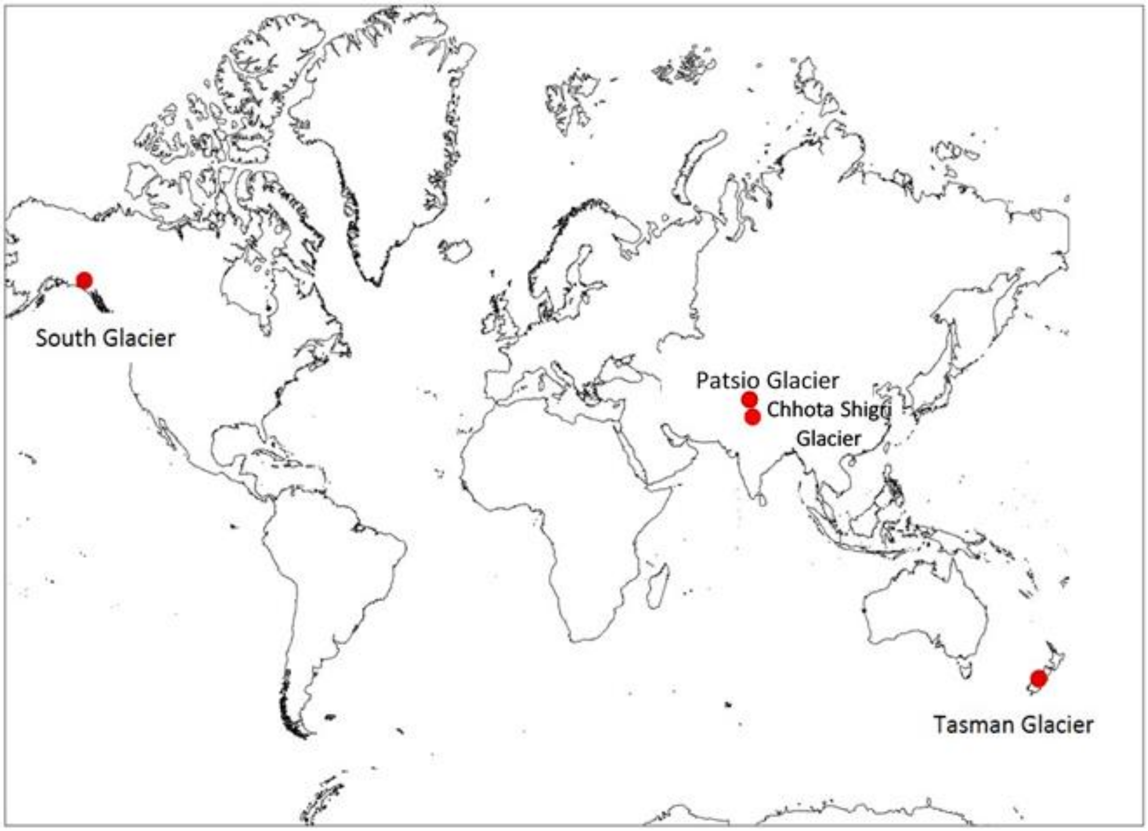

Figure 4.1 Locations of the study glaciers: South Glacier (Canada), Patsio Glacier (India), Chhota Shigri Glacier (India), and Tasman Glacier (New Zealand).

The Tasman Glacier is located in the Southern Alps and is the largest glacier of New Zealand. The region is dominated by marine west coast climate. Surrounded by New Zealand's highest peaks, numerous tributary glaciers contribute to this glacier system. These glaciers have been chosen to represent a variability in the following aspects: glacier complexity, debris coverage, size and climatic region (Table 4.1).

Based on the availability of filed measurements for glacier velocity and ice thickness, three glaciers have been chosen for velocity estimation and validation (Chapter 5). Whereas four glaciers (Patsio Glacier) were chosen for estimation and validation of ice thickness. In particular, the fourth glacier (Patsio Glacier) has only ice thickness data (which is recently collected by our glaciology team) but no velocity data measurements. This led to leave Patsio Glacier from (Chapter 5: velocity estimation) but include in the (Chapter 6: ice thickness estimation).

Table 4.1 Details of the study glaciers**.**

Glacier	Lat/Long	Length	Debris Coverage	Orientation	Country	Elevation Range (m)
South Glacier	60.88º N 139.12º W	4 km	No	South	Alaska	1970-2960
Patsio Glacier	32.4º N 77.41º E	3 km	Yes	North	India	4875–5694
Chhota Shigri Glacier	32.24º N 77.51º E	9 km	Yes	North	India	4050-6263
Tasman Glacier	32.75º N 77.33º E	25 km	Yes	South	New Zealand	3870-5500

4.1.2 Geometry and Surface Morphology

South Glacier is a small glacier being about 4 km long and around 700 m wide, and is totally free of debris. With an average slope of 13º, it lies within the altitude range of 1970-2960 m.

Patsio Glacier is also a small glacier extending up to a length of ∼2.7 km and covers an area of ∼2.37 km^2. This glacier lies within the altitudinal range of 4875–5694 m a.s.l with an average elevation of 5342 m a.sl. The glacier wide average slope is 22º. Unlike other nearby glaciers, the Patsio Glacier has few medial moraines.

The Chhota Shigri Glacier is a medium sized glacier about 9 km long with an average width of 800 m. This glacier has mild debris cover. Its average slope is 17º and elevation range lies between 4050 m and 6263 m.

Tasman Glacier extends up to a length of about 25 km with an average width of about 1300 m. The average surface slope of the glacier is 5.4º and the elevation ranges from 3870 m to 5500 m. Frequent rock avalanches help sustain a relatively thick debris cover on this glacier, which terminates in the proglacial Tasman Lake. A google earth image showing the top view of all four study glaciers is given in (Figure 4.2).

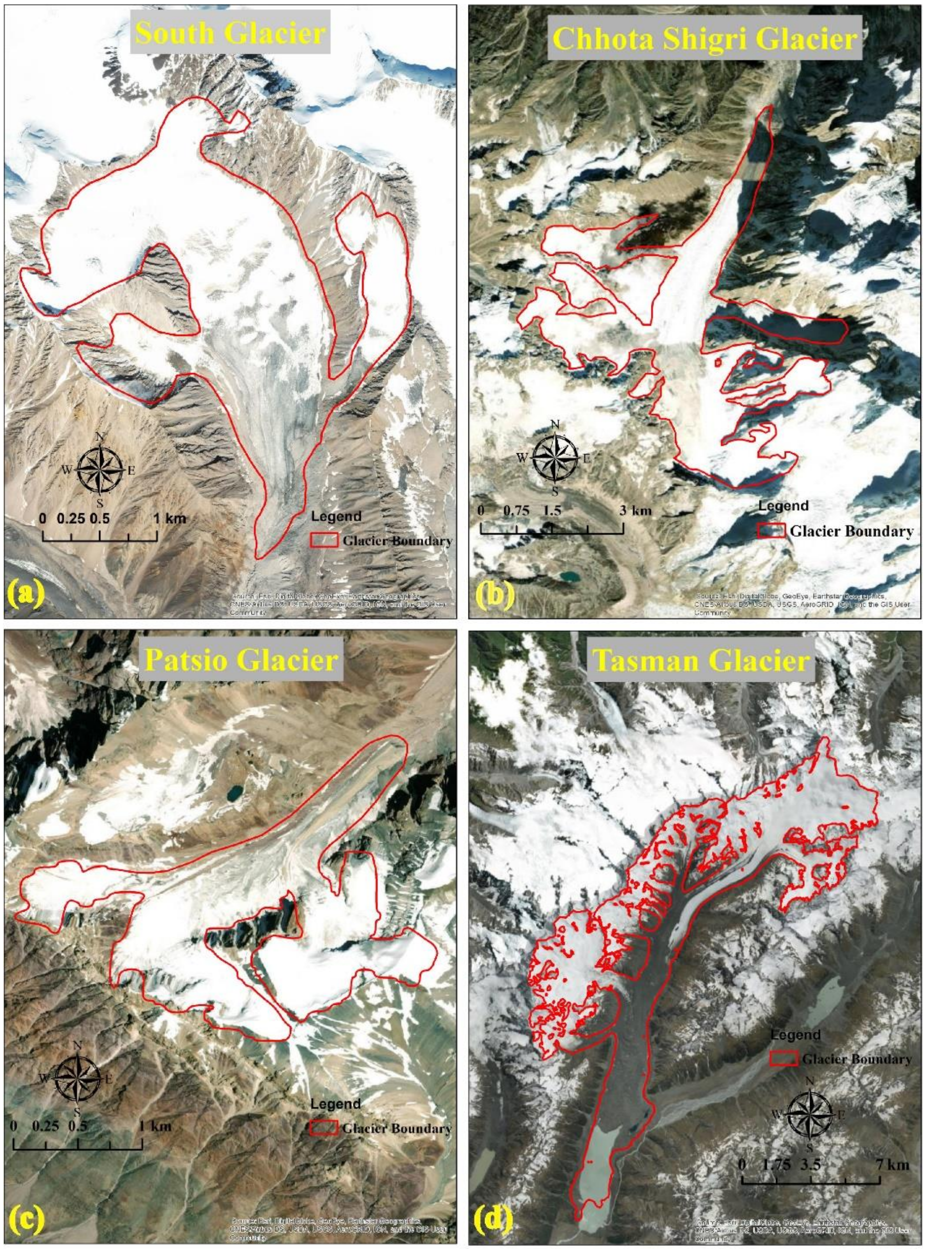

Figure 4.2 Google earth imagery of the study glaciers(a) South Glacier, (b) Chhota Shigri Glacier, (c) Patsio Glacier, and (d) Tasman Glacier.

4.2 Remote Sensing Datasets

To carry out glacier surface velocity estimation for all four of the study glaciers, both optical and SAR remote sensing imagery was utilized. The detailed methodology involving these datasets is described in chapter 5. Since these data were involved in two different steps, the optical and SAR data are discussed separately. Sincere efforts have been made to gather these data for each individual glacier at a common timestamp and similar spatial resolution. However, data inconsistencies remain due to problems such as cloud cover and limited temporal coverage of freely accessible data.

4.2.1 Optical Dataset

The optical dataset was used in the first step of the glacier velocity estimation to determine the window size for image matching. The choice of optical imagery to find scale of feature tracking was bound by the condition that the imagery should have the same resolution as the SAR dataset, and that they should be temporally overlapped with the corresponding SAR images. Images acquired during or nearby the end of ablation season (September for South Glacier, Patsio Glacier and Chhota Shigri Glacier; March for Tasman Glacier) were used to achieve maximum snow free coverage on the glaciers. However, due to unavailability of any cloud free ASTER data covering South Glacier in the ablation period, data from a different season had to be used. The optical data used is of March 2006. The optical datasets used to perform image segmentation and determine the window size for SAR image matching are listed in (Table 4.2).

It should be noted that the reason to use different data sets was their availability during the study period. The data mentioned in Table 4.2 were taken as orthorectified products which is a standard requirement for glacier feature tracking methods. No additional processing was done in this study.

Table 4.2 Optical dataset used to determine window size for glacier velocity estimation.

Glacier	Satellite & (Sensor)	Date	Path/Row	Band No (Spectral Region)	Spatial Resolution
South Glacier	Terra (ASTER)	Mar 02, 2006	204/717	VNIR 3* (0.76 - 0.86 µm)	30 m
	Landsat 8 (OLI)	Aug 29, 2013	061/017	PAN 8 (0.5 - 0.68 µm)	15 m
	Landsat 8 (OLI)	Nov 20, 2014	061/017	PAN 8 (0.5 - 0.68 µm)	15 m
Chhota Shigri	IRS P6 (LISS-III)	Oct 13, 2009	095/048	VNIR 2 (0.52 - 0.59 µm) 3 (0.62 - 0.68 µm) 4 (0.77 - 0.86 µm) SWIR 5 (1.55 - 1.70 µm)	24 m
		Oct 08, 2010			
Patsio Glacier	Sentinel2 (MSI)	Sept 12, 2017	Patsio Glacier	VNIR Band 2 (0.49 - 0.60 µm) 8a(0.86 -0.60 µm)	20 m
Tasman Glacier	Terra (ASTER)	Jan 24, 2006	223/604	VNIR 1 (0.52 - 0.60 µm) 2 (0.63 - 0.69 µm) 3 (0.76 - 0.86 µm)	15 m

4.2.2 SAR Dataset

The SAR dataset was used to perform the second step of glacier velocity estimation. To preserve the applicability of the velocity estimation technique, the SAR imagery used should have the same radar acquisition parameters. The SAR SLC data used in the study are listed in Table 4.3 and Table 4.4. It should be noted that the Sentinel 1 data for South Glacier gives an effective resolution of 15m (instead of 20m). This is due high latitude (near polar region) of the glacier location. The main aim of the thesis was to model the ice thickness of glaciers where the time scale of the underlying process is large for e.g., one year or more. Accordingly, to estimate the glacier velocity suitable for ice thickness modelling, a time period of 1 year was chosen. This was also done to eliminate any seasonal velocity variation in the estimated velocity which would affect comparison with the long term averaged annual velocity data. Since the feature tracking was performed on SAR imagery it was preferable to use L-band due to its better radar signal penetration, which increases the correlation between two long-interval images (Rignot et al., 2001, Nakamura et al., 2007). Using L-band also tackles the problem of decorrelation in snow-covered areas but can be affected by the wetness of snow (Casey et al., 2016); this aspect could not be explored in this study because the snow wetness conditions were unknown for the study glaciers during the study period. The limited availability of the freely available L-band ALOS data has led to usage of C band wherever L-band was not available. The polarization of the available SAR dataset for the chosen study periods were limited to only single pol (either VV or HH) and no other dual pol data was available, restricting the ability to investigate the effect of polarization in the feature tracking.

Table 4.3 SAR dataset used for glacier feature tracking to estimate glacier surface velocity (horizontal).

Glacier	Satellite	Time 1	Time 2	Polarization	Pass	Spatial Resolution
South Glacier	Envisat	Dec-2005	Dec-2006	VV	Descending	20 m
	Sentinel 1	Oct-2014	Oct-2015	VV	Descending	15 m
Chhota Shigri	Envisat	Sept-2009	Sept-2010	VV	Descending	20 m
Patsio	Sentinel 1	Oct-2016	Oct-2017	HH	Descending	20 m
Tasman	Envisat	Mar-2005	Mar-2006	VV	Descending	20 m
	ALOS PALSAR	Mar-2007	Mar-2008	HH	Descending	12.5 m

Table 4.4 SAR dataset used for glacier feature tracking dataset used for glacier feature tracking to estimate glacier surface velocity (vertical).

Glacier	Satellite	Time 1	Polarization	Pass	Spatial Resolution
South Glacier	Sentinel 1	Oct-2014	VV	Ascending	15 m
	Sentinel 1	Oct-2015	VV	Descending	15 m
Chhota Shigri	Envisat	Sept-2009	VV	Descending	20 m
	Envisat	Sept-2010	VV	Ascending	20 m
Patsio	Sentinel 1	Oct-2016	HH	Ascending	20 m
	Sentinel 1	Oct-2017	HH	Descending	20 m
Tasman	Envisat	Mar-2005	VV	Ascending	20 m
	Envisat	Mar-2006	VV	Descending	20 m

4.3 Ancillary Dataset

Apart from satellite imagery, other datasets such as a DEM and the glacier boundary were also used. The freely available Shuttle Radar Topography Mission (SRTM) 1 second DEM was used to derive slope for the glaciers as well as to orthorectify the SAR imagery used in glacier feature tracking. Due to the lack of SRTM data above 60° North, the Canadian Digital Elevation Model (CDEM) was used for South Glacier. Glacier outlines were taken from the latest version of the Randolph Glacier Inventory (RGI 6.0).

4.4 In-situ Dataset

The data collected as part of this thesis for calibration (only ice thickness estimates) and validation (both velocity estimates and ice thickness estimates) is given in this section. A brief introduction is provided for additional data taken from literature and through personal communication. However, a detailed description of the data collected for Patsio Glacier through a dedicated GPR survey performed during 2017 is given.

4.4.1 Available Glacier Surface Velocity and Ice Thickness Dataset

4.4.1.1 Velocity

The glacier surface velocity measurements collected over the study glaciers were taken from different sources as mentioned in Farinotti et al. (2017). It should be noted that these surface velocity measurements are only the horizontal velocities which are used for validation in this study. The vertical component of glacier surface velocity is not available for validation. For South Glacier, the velocity data was obtained from Flowers et al. (2011), which was collected during the years 2005-2014. For Chhota Shigri Glacier, the field measured glacier velocity information was obtained from Azam et al. (2012), which was collected during the years 2009-10. Likewise, for Tasman Glacier, the reference glacier velocity data as reported by Farinotti et al. (2017) and Purdie et al. (2018), collected during the years 2000-2011, was used for validation.

4.4.1.2 Ice Thickness

The ice thickness measurements for three study glaciers (South Glacier, Chhota Shigri Glacier and Tasman Glacier) were taken from the freely available Glacier Thickness Database (GlaThiDa) 3.0.1 (Gärtner-Roer et al., 2014). The ice thickness data collected for

Patsio Glacier is described in section 4.4.2. The spatial distribution of these data is shown in Figure 4.3.

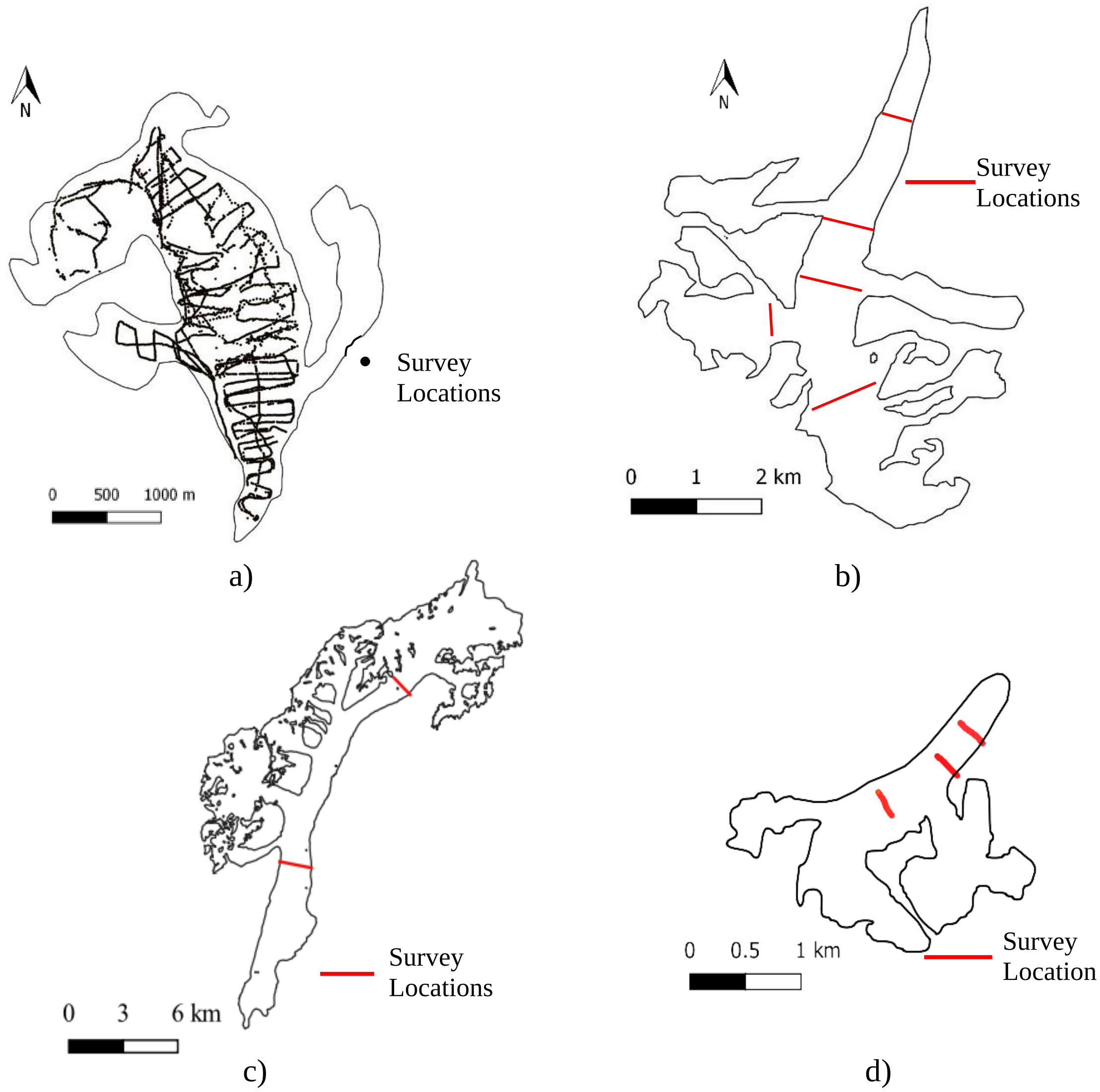

Figure 4.3 Locations of the ice thickness data of the study glaciers taken from available literature (a-c) and collected during field survey (d) depicting their spatial distribution. a) For South Glacier the surveyed locations are spread across the whole glacier. Surveyed location of Chhota Shigri Glacier (b), Tasman Glacier (c) and Patsio Glacier (d).

4.4.2 GPR Based Glacier Ice Thickness Measurements

The ground penetrating radar (GPR) survey was carried out using a Geophysical Survey Systems Inc. (GSSI) SIR 3000 system. Data was collected with a Multiple Low Frequency (MLF) antenna at central frequency of 35 MHz for four profiles (Figure 4.4d) over the surface of Patsio Glacier during July 2017.

Considering the parameters adopted in earlier studies conducted in the Himalayan region (eg. Mishra et al., 2018; Singh et al., 2012; Singh et al., 2018; Swain et al., 2018) and the recommendations for deep sub-surface investigations using low frequency antenna given in the GSSI RADAN 7.0 manual, the GPR parameters were chosen for this study. Accordingly, this survey was carried out in point-mode in which the transmitter and receiver were shifted together in steps of 1 m, throughout. The receiver and transmitter antenna were separated by a constant distance of 2m to avoid any signal interference. The input parameters to the GPR system during data collection for dielectric constant are summarized in Table 4.5, including samples per scan, stacking and other details.

Table 4.5 Details of the GPR data acquisition parameters.

GPR parameter	Setting	Remarks
Antenna central frequency	35MHz	-
Antenna separation	2m	-
Samples/scan	2048	To ensure finer depth profile of scans.
Stacking	64	To reduce the effect of noise from individual signals.
Dielectric constant	3.14	-
Radar velocity in ice	0.168 m/ns	-
Range	4500ns	-
High pass filter (IIR)	10 MHz	-
Low pass filter (IIR)	105 MHz	-

The raw GPR data collected during the survey was processed using GSSI-RADAN v7.0, a propriety software by GSSI. Processing steps common to almost all ground penetrating radar based surveys (Mishra et al., 2018; Singh et al., 2012) were conducted and included the following: (1) horizontally appending individual data files comprising multipart survey lines; (2) static position correction also known as time zero correction to bring air-wave return to the top of the scan time window; (3) application of an infinite response filter with a 10/105 MHz filter for the 35 MHz survey data; (4) background removal and (5) auto gain adjustment. Additional processing steps, effective for noise removal in geophysical surveys of glaciers, included (6) migration, and (7) deconvolution. These additional processing steps are discussed below:

Migration - The radar antenna radiates energy with a wide beam width pattern such that objects few meters away may be detected. Consequently, objects of finite dimensions may appear as hyperbolic reflectors on the radar-gram. Objects or layers beneath may be obscured by shallower objects above them. This causes diffracted reflections of radar energy and can mask other reflections of interest and cause misinterpretation of the depth being measured. To avoid this misinterpretation, following some previous studies on glacier ice thickness measurements (Jouvet et al., 2009; Jouvet et al., 2011; Bohleber et al., 2017), migration has been applied to the collected data.

Deconvolution - This filtering method was used to remove the noise due to multiple reflections between subsurface objects (Singh et al., 2012; Lapazaran et al., 2016).

4.4.2.1 Differential Global Navigation Satellite System (DGNSS) Data

Locations of the GPR survey were precisely measured using the Geo-XH GNSS system in differential mode. A base station was established at a stable region near the glacier snout. After standard post processing using the post-processed kinematic (PPK) module in Trimble Business Centre V4.1, the horizontal accuracy of the measured locations was found to be 5-10 cm.

4.4.2.2 Snow and Debris Thickness

Snow depths over the surveyed profiles (1 - 4) were measured through a snow profiler placed at the same locations where the GPR data were collected. These measurements were performed simultaneously during the GPR and DGNSS survey. Snow thickness varied between 25 and 260 cm. The debris thickness was measured only at Profile 1 as other profiles were free of debris. This depth information was used for adjusting the field measured ice thickness

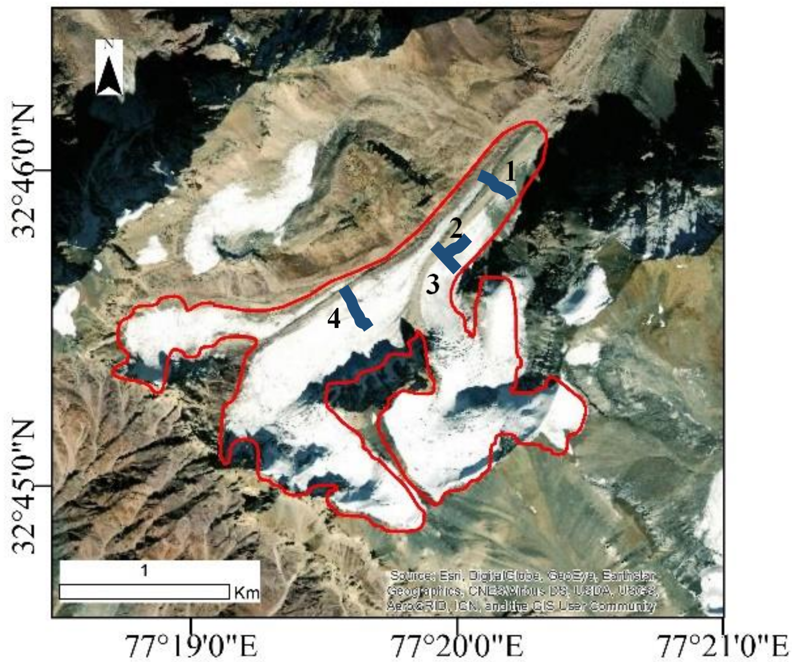

Figure 4.4 Survey locations of Profiles 1-4 (shown in blue) over Patsio Glacier

The uncertainty of ice thickness estimates from the GPR measurements can be due to two factors: radar wave velocity of the GPR signal c and the two-way travel-time t (Lapazaran et al., 2016). Thus, the total uncertainty in ice thickness ($\frac{\Delta d}{d}$) was estimated as

$$\frac{\Delta d}{d} = \sqrt{\left(\frac{\Delta c}{c}\right)^2 + \left(\frac{\Delta t}{t}\right)^2}\,. \tag{4.1}$$

Following Mishra et al., (2018), uncertainty in Δc was assumed to be ~7%. Likewise, Δt was assumed to be the width of positive and negative wave reflections that occurs on the glacier bed region (Mishra et al., 2018). The Δt was measured to be 15 nanoseconds for the survey profiles.

4.4.1.3 Measured Ice Thickness

The processed radar-gram for four survey profiles are shown in (Figure 4.5). For illustration, Figure 4.5a and Figure 4.5b show the raw radar-gram and processed radar-gram respectively for Profile 1. The raw radar-gram shows noise with more pronounced bands of constant horizontal reflections (Figure 4.5a) which were significantly reduced after the processing (Figure 4.5b). Similar processing steps were followed for each profile. Figure 4.5c-e show the processed radar-gram of the Profiles 2-4 respectively. To identify the bed profile, the standard procedure (GSSI RADAN 7.0 manual) was followed using RADAN software. First the strong reflections were identified along the scans which represent the contrast in the two mediums (here its ice and bedrock). Second, the exact location was determined by following the RADAN 7.0 manual for geoprocessing applications. Here the yellow line in figure 4.5 was delineated manually using the pick tool where a search is performed (by the software) on all of the scans between the left and right inside edges of the mouse cursor to locate the maximum amplitude. It should be noted that the thickness due to snow and debris measured at different profiles have been subtracted from the field measured ice thickness from GPR at the respective locations. This was done to facilitate an equitable comparison with the modelled ice thickness estimates. The ice thickness obtained from the radar-gram (after adjusting for snow and debris thickness) of the surveyed profiles is shown in Figure 4.6. It shall be noted that these GPR based cross-section profiles (Figure 4.6) do not exhibit a parabolic shape, which is possibly because the surveyed profiles do not cover a full cross-section of the glacier. Table 4.6 gives the key statistics of each surveyed profile. The uncertainty in the GPR derived ice thickness was estimated to be ±7.8%.

Table 4.6 Details of the surveyed profiles shown in **Figure 4.4**.

Survey Profile	Mean Measured Ice Thickness	Mean Elevation	Length
Profile 1	36 m	5020 m	300 m
Profile 2	53 m	5075 m	115 m
Profile 3	57 m	5090 m	260 m
Profile 4	103 m	5200 m	260 m

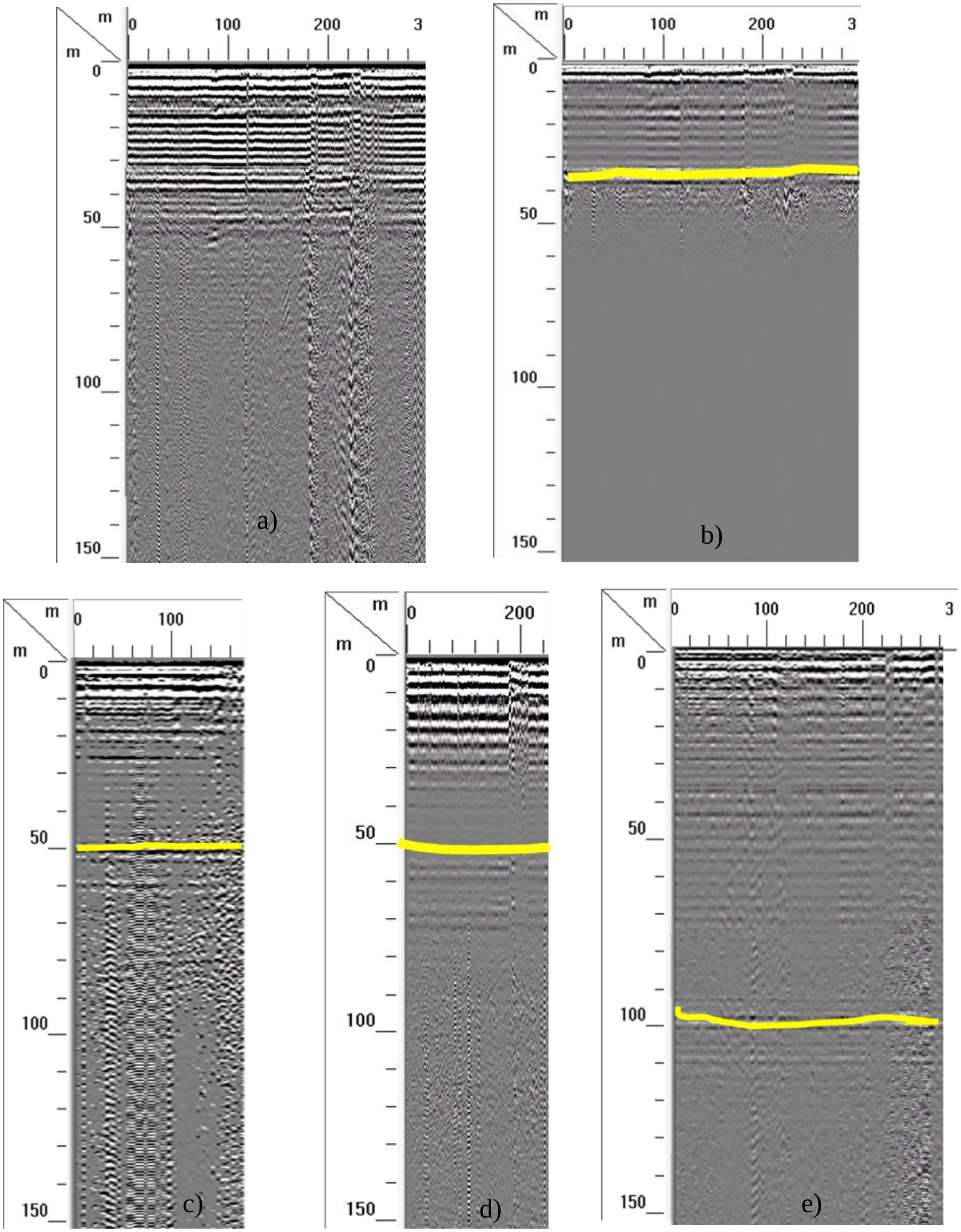

Figure 4.5 Radar-gram of profile 1 (a) before and (b) after processing, and processed radar-grams of profiles 2-4 (c-e). The yellow line denotes the depth (in m) of bedrock topography.

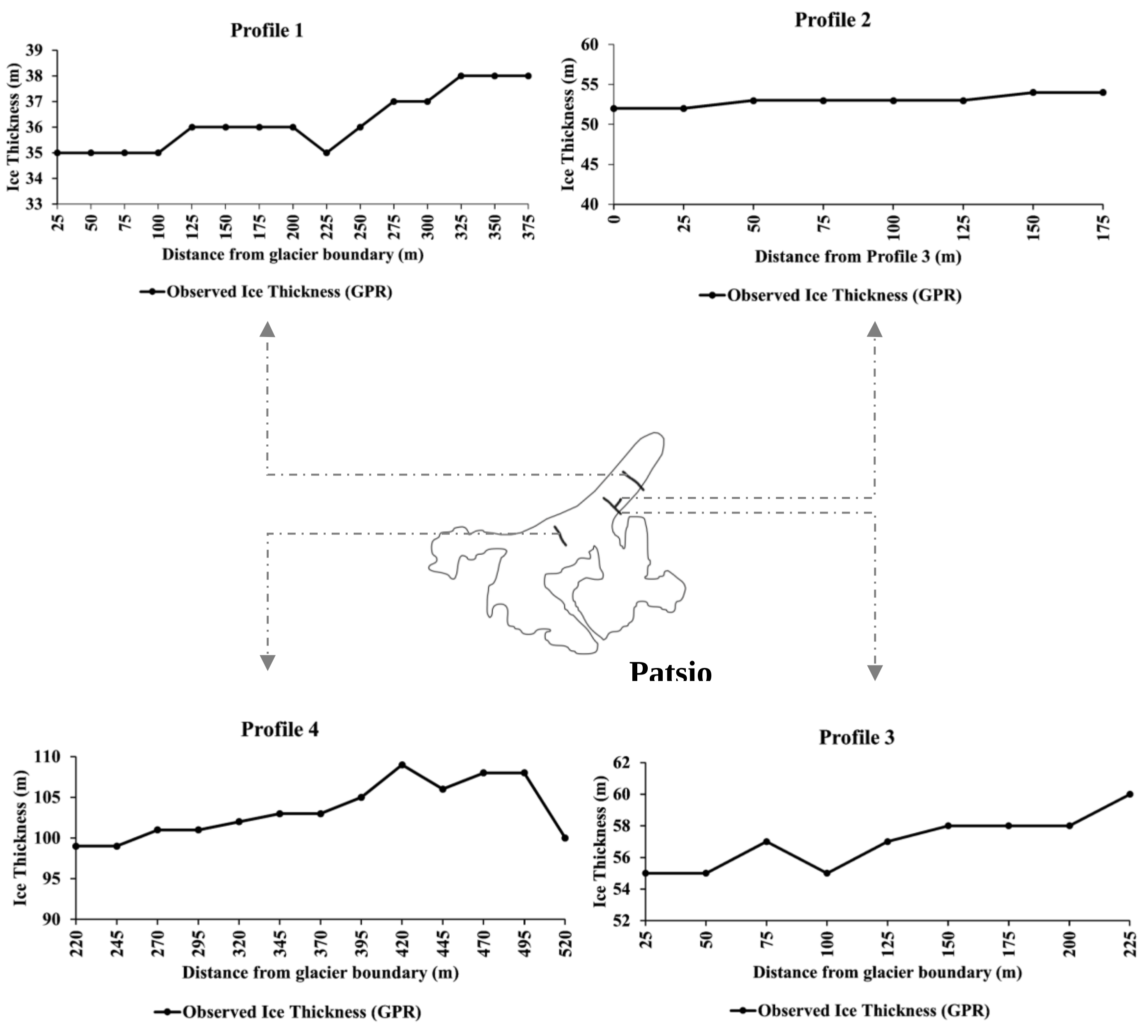

Figure 4.6 Observed ice thickness at the surveyed profiles of Patsio Glacier**.**

4.4.3 Data Quality

The data used for validation of ice thickness modelling varied in terms of nature of collection. For example, South Glacier was surveyed using airborne radar due meaning that data was available for whole glacier area, whereas for the other glaciers, the data collected using ground penetrating radar was limited to certain cross sections. This constrained coverage affects the detailed evaluation the glacier wide ice thickness estimation. Certain additional uncertainties remain due to the velocity of the flight during the airborne radar survey. Apart from this, for some glaciers the data was gathered in a long span of time. For example, the velocity data available for South Glacier was collected over 2005-2014. Several stakes were measured for intermediate duration, and the average for the same was mentioned. Additionally, the timestamp of ice thickness data available for validation also affects the modelling. For example, Tasman Glacier's ice thickness observation was available only for the year 1971, for which the required remote sensing datasets were not available.

4.5 Chapter Summary

This chapter presented an overview of the four study glaciers common to velocity as well as ice thickness modelling and the data that were used to set up and validate the experiments outlined in this thesis. The optical and SAR data described in this chapter were used to estimate the glacier surface velocity in Chapter 5. This velocity was then used along with the DEMs to estimate the ice thickness distribution over the study glaciers in Chapter 6. All the remote sensing data listed above are freely available. The timestamp of the available ice thickness dataset (used for model validation) majorly determined the timestamp of the remotely sensed input data gathered.

CHAPTER 5

5 GLACIER SURFACE VELOCITY ESTIMATION

The main objective of this thesis is to model the glacier ice thickness distribution using remotely sensed velocity. The literature review revealed several gaps in the utilization of remote sensing for ice thickness and glacier velocity estimations. Accordingly, to estimate this glacier surface velocity irrespective of the field data availability, the proposed remote sensing based feature tracking algorithm is presented in this chapter. This feature tracking algorithm was applied to the study glaciers and its performance was assessed over South Glacier, Chhota Shigri Glacier and Tasman Glacier for which the glacier surface velocity field measurements are available for validation. Additionally, several different remote sensing datasets were assessed for implementation capability of the proposed feature tracking algorithm and contribution towards automation explored.

5.1 Methodology

The proposed feature tracking algorithm SWIFT (**S**patially varying **WI**ndow based maximum likelihood **F**eature **T**racking) (Figure 5.1) comprises two stages: i) determination of the spatially varying window size from optical image based on the Object Based Image Analysis (OBIA) concept, and ii) image matching based feature tracking using the maximum likelihood of SAR speckle as similarity measure. The proposed algorithm for feature tracking uses a spatially varying window size which cannot be provided by existing software like SNAP, SARscape, COSI-Corr.

5.1.1 Automated Determination of Window Size

To find the optimum window size distribution for image matching, the concept of Object Based Image analysis (OBIA) has been used. Using this approach, the glacier is divided into homogeneous regions called segments. This segmentation is done at a scale determined as optimum by the approach presented in Dragut et al. (2010), where the optimal scale of segmentation was identified from the peak rate of change of local variance (ROC-LV) in the image. Here the segmentation was performed using a bottom-up approach of region-growing segmentation (Dragut et al., 2010), in which, starting from one pixel, the segment grows in size; the growth is defined by the scale that controls the homogeneity of the resulting segments. Once the segment properties exceed the heterogeneity threshold (as determined by the scale), this growth stops. Additional constraints can be provided by giving weight to shape and compactness of the resulting segments. The weights given to the shape factor indirectly signifies how much spectral information should be used. Conversely, the weight given to the compactness factor signifies the degree of compactness of the segments' shape (Definiens Developer, 2007).

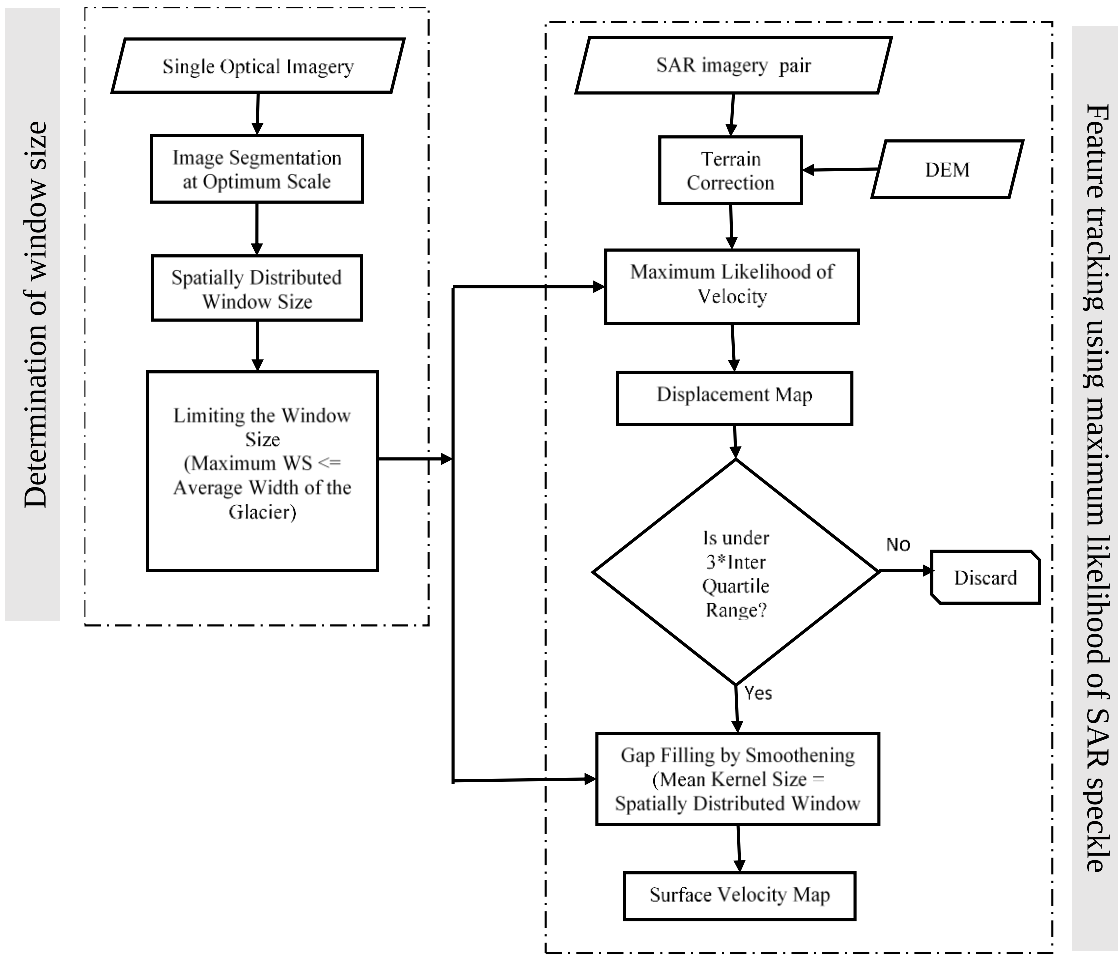

Figure 5.1 Proposed feature tracking algorithm (SWIFT) for glacier surface velocity estimations using optical and SAR imagery.

Assuming that the glacier features can be of varying shapes which are rarely compact, the shape and compactness of segments are not considered in the present study, thus giving weight only to the pixel values (also known as digital number) in the optical image. It is certain that some glacier surface features can be described in a fractal form as they have specific shapes. However, to track all the features of known as well as unknown shape using fractal forms may lead to bias towards known features. Moreover, this weight assignment was checked manually through visual analysis at the initial processing stage. However, no quantification could be done at this stage due to insufficient field information and non-availability of high-resolution optical dataset. The image segmentation was performed on optical imagery falling in the same season as that of the SAR images to reduce any seasonal disturbances contributing to errors in the feature tracking.

A segmented image contains different shape and size segments. To calculate the window size for image matching, geometric properties like length and width of segments have been utilized in the present study. To avoid complexity, instead of matching 'segments' which are irregular in nature, a simplified square size window was chosen to perform image matching without any major loss in information. The square window, which closely matches the segment's geometry is referred to as the window size (WS). Since the segments may vary in geometry over the glacier, the window size was kept as a spatially varying parameter. The main advantage of having a spatially varying window size(s) over that of a fixed window size is that different sized features can be tracked more accurately, with window size(s) closely corresponding to actual features over the glacier surface. Additionally, a constraint was applied to the window size distribution in which only window sizes less than or equal to the average width of the glacier were considered. Window sizes greater than this were discarded to avoid any unrealistic large values of window size. Here, the average width of the glacier was calculated by taking the cross sectional width at different locations of the glacier's main trunk to approximate the average width of the glacier. This step should not be interpreted as manual selection. As with the advent of GIS tools, and freely available datasets containing glacier polygons, automated calculation of glacier geometries such as length and width are possible (Pfeffer et al., 2014; James and Carrivick, 2016). This window size selection technique is independent of glacier type or its environment setting, thus this technique is applicable to the glaciers in any setting.

5.1.2 SAR Feature Tracking

A multiplicative speckle model-based SAR feature tracking algorithm was implemented to estimate glacier surface velocities, where images are compared based on maximum likelihood of SAR speckle. Speckle, which is inherently present in every SAR image gives useful information about the glacier surface characteristics. This speckle can be tracked in time-lapse SAR imagery and thus helps estimate glacier flow.

Before performing the image matching, geometric distortions in SAR images due to side looking viewing geometry have been corrected using the freely available SRTM 30 DEM. The geometric co-registration of the SAR dataset has been addressed during DEM assisted co-registration (Nitti et al., 2010; Sanchez-Gamez and Navarro, 2017) in Terrain Correction with an RMSE threshold of 0.3 (of pixel size) in the co-registration. It should be noted that all the processing was performed for feature tracking on a subset of SAR imagery (not the full scene) for efficient data processing. All SAR imagery (Chapter 4.3) except the ALOS PALSAR image (which was already terrain corrected) were processed via the freely available Sentinel Application Platform (SNAP) toolbox. Readers are referred to the SNAP user guide for a detailed description of this process.

Assuming that the blocks to be matched between two SAR images X and Y of size $m \times n$ share a common region at two annually separated time periods T1 and T2. For each block/matching window, the distribution of Maximum Likelihood (ML) estimators was calculated for different candidate shifts between the two images. The maximum likelihood estimate (v_{ML}) of velocity v_i was obtained by maximizing the cumulative distribution function (CDF) function (ρ) for each block i according to

$$\rho\left(x_{ij} \middle| y_{ij}, v_i\right), \tag{5.1}$$

where x_{ij} and y_{ij} are the pixels corresponding to block X and Y respectively. The above function can also be represented in terms of block size by the objective function

$$\sum_{j=1}^{k} \ln y_{ij} + \ln x_{ij} - 2 \ln(x_{ij}+y_{ij}) - \frac{\ln x_{ij}}{N}, \tag{5.2}$$

where k is the total number of pixels in a block and N is the multi-looking factor.

Following Debellagilo and Kaab (2010), sub-pixel interpolation has been undertaken to achieve sub-pixel precision of $1/4^{th}$ of a pixel by capturing the displacements smaller than the spatial resolution of the input satellite images.

The horizontal displacements were derived by following Strozzi et al. (2002) and Sanchez-Gamez and Navarro (2017) to facilitate the comparison with ground based field measurement of horizontal glacier velocity. From the azimuth and slant range displacements, the net displacement is calculated using the relation

$$\text{Net Displacement} = \sqrt{(R_x\Delta x)^2 + (R_y\Delta y)^2}, \tag{5.3}$$

where R_x and R_y are the pixel spacing in azimuth and slant range directions, Δx and Δy are the displacements in azimuth and slant range directions. The velocities outside the 3*Inter Quartile Range (IQR) have been removed as outliers from the estimates (Figure 5.2). The blank patches have been filled using a mean filter where the kernel size is kept the same as the window size distribution. This filtering approach has been chosen to eliminate the subjectivity of choosing a smoothing filter for individual glaciers.

5.2 Results and Discussions

This section describes the window size obtained for different study glaciers, followed by the results of estimated glacier surface velocity. Experiments were carried out to investigate the effects due to input data characteristics and spatially varying window size over spatially fixed window size. Finally, a comparison of the velocity estimates with the cross correlation based feature tracking method is discussed.

5.2.1 Window Size Determination

Following the methodology discussed in section 5.1.1, a spatially varying window size has been determined for each study glacier. It was found during image segmentation that the segments sometime merged with areas outside of the glacier due to very low/no contrast between the glacier and its surroundings (Figure 5.2). This results in a very large window size, which could be as large as the size of the glacier itself. To control this, the constraint on maximum window size as mentioned in section 5.1.1 has been applied to all three study glaciers used in this chapter. Consequently, significant improvement in the estimated velocity was observed for Tasman Glacier, as reported in section 5.2.3. However, for the other two glaciers (South Glacier and Chhota Shigri Glacier) no changes were observed due to the absence of segments merging with the background.

Sometimes due to cloud cover, using an optical image of the desired acquisition period may not be possible. Thus, to investigate possible alternatives, a comparison was made between the window size distributions from optical images acquired at two different time periods (T1 & T2) a year apart. For illustration purpose, the window size distribution obtained for the Chhota Shigri Glacier from the images acquired in 2009 and 2010 ablation period are shown in Figure 5.3a-b. The results obtained indicate a similar trend of window size distribution for both images.

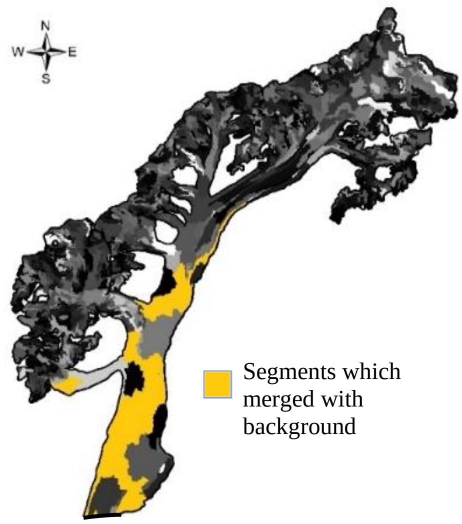

Figure 5.2 Segmented image of Tasman Glacier using ASTER (band 1-3). The highlighted segments in yellow are those segments inside the glacier boundary which merged with a large segment outside the glacier area.

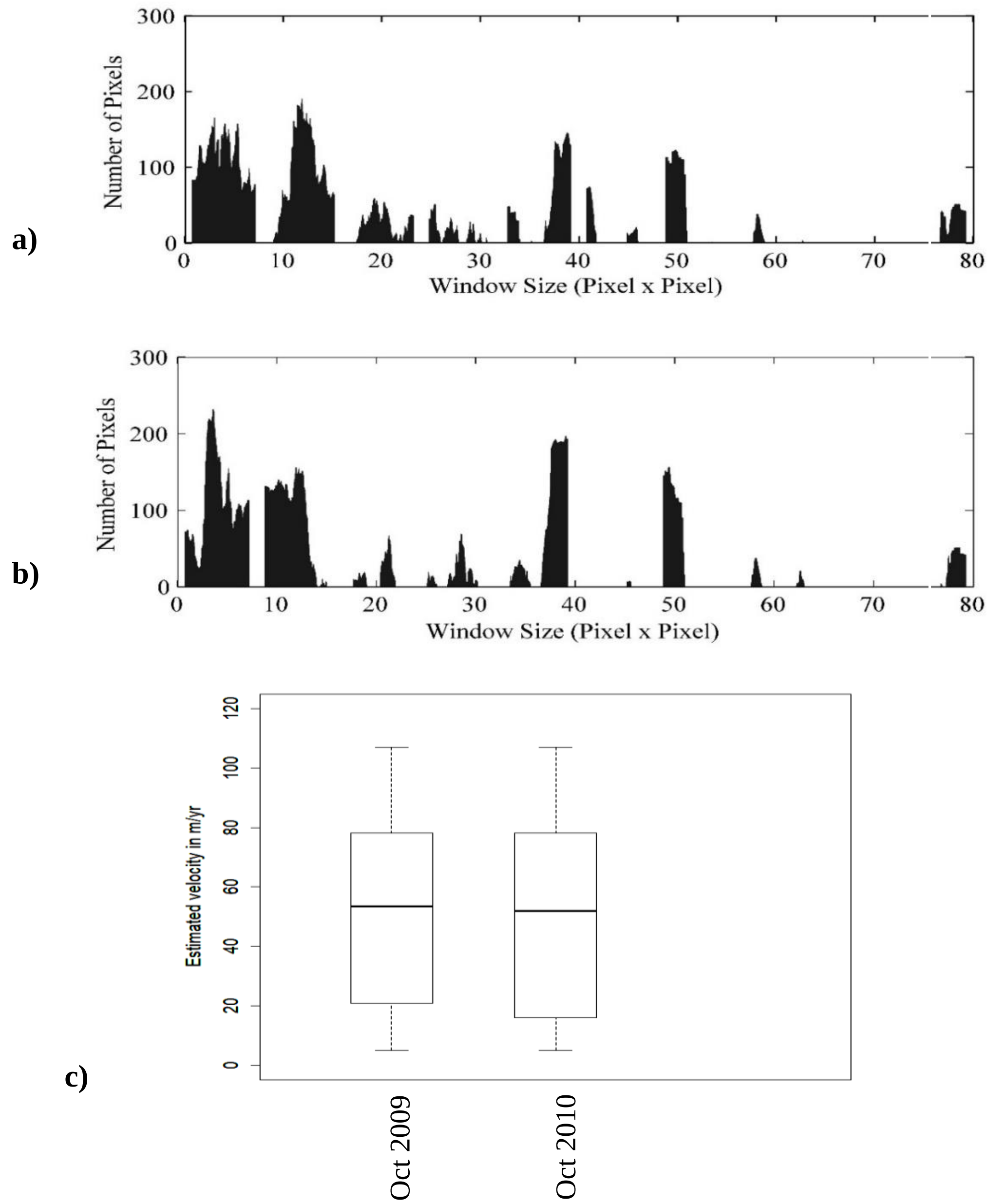

Figure 5.3 Window size distribution of Chhota Shigri Glacier using optical images of a) Oct, 2009 and b) Oct, 2010. c) The statistical distribution of surface velocity estimates using spatially varying window size obtained from a) & b).

This portrays that the window size from the same season's imagery (a year apart) leads to a similar window size distribution. Furthermore, the similarity due to the two window sizes was also reflected in the estimated velocity (Figure 5.3c). Based on this analysis it is evident that choosing either T1 or T2 optical imagery did not have a significant effect on the estimates. It is also observed that for a medium sized glacier such as Chhota Shigri Glacier, the window size barely crosses 80 x 80 pixels, which gives an idea of range of window sizes that can be used for medium sized glaciers. However, this observation needs to be verified by extensive testing of the algorithm. Similar results were obtained for South Glacier (see Appendix- A3), supporting the similarity in window size distribution from two optical images of different time. This analysis could not be performed for Tasman Glacier, since only one optical image was available during the study period.

5.2.2 Glacier Surface Velocity Estimates

5.2.2.1 South Glacier

Here, the proposed feature tracking approach (Figure 5.1) has been implemented for two time periods; 2005-06 and 2014-15. Accordingly, the available ASTER (Mar 02nd, 2006) and Landsat 8 (Nov 20th, 2014) images were used to determine the spatially varying window sizes respectively for the 2005-06 and 2014-15 time periods. The final spatial distributions of the estimated surface velocity for the two time periods are shown in Figure 5.4a and b.

As reported by De Paoli and flowers (2009), South Glacier can be divided into three zones (Figure 4.1a) based on morphology and glacier dynamics: i) crevasse free and smooth lower zone (less than 1700m from snout), ii) extensive crevasses and undulating surface middle zone (1700-3000m from the glacier snout), and iii) upper zone (3300m and beyond from snout) with crevasses and undulating zone in association with prominent icefall. The zone wise and overall error statistics for all three study glaciers are given in Table 5.1. The overall RMSE of the surface velocity estimates of South Glacier for the periods 2005-06 and 2014-15 with respect to the glacier wide stake measurements given by Flowers et al. (2011) were 13.25 m/yr and 12.8 m/yr respectively (Table 5.1). Here the overall bias for these periods were 9.5 m/yr and 11 m/yr respectively (Table 5.1).

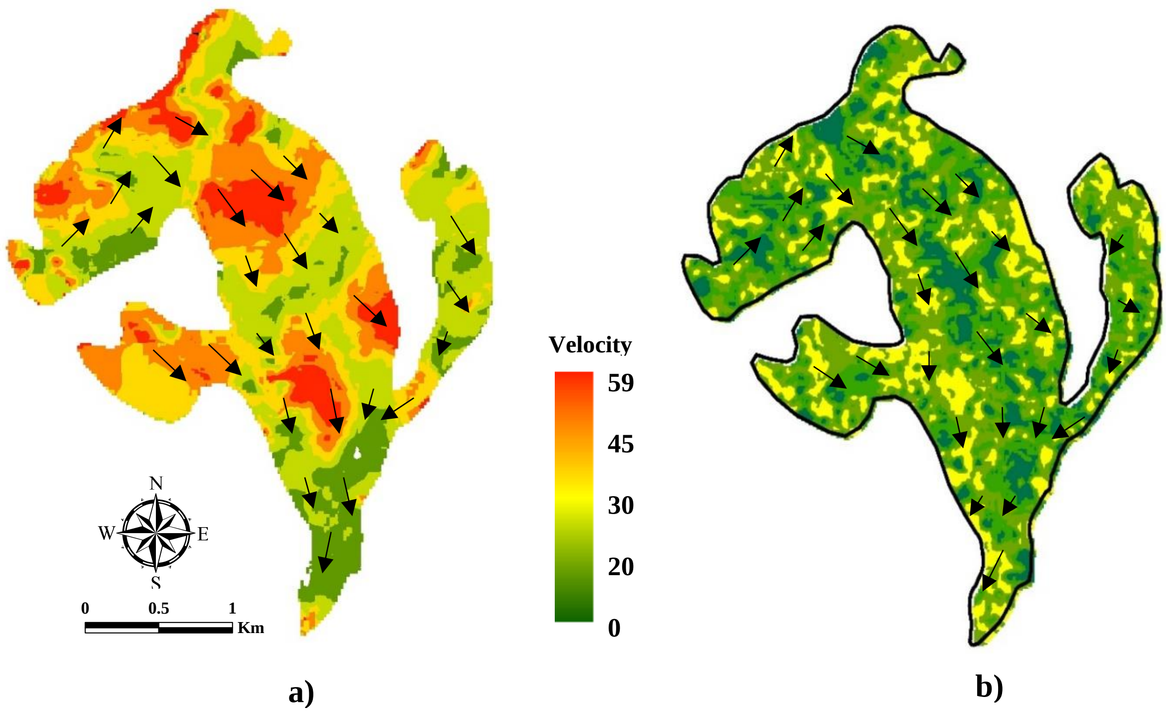

Figure 5.4 Spatial distribution of the estimated surface velocities of South Glacier a) for 2005-06 and b) for 2014-15. The arrows show the direction of estimated velocity at every 200m.

The uncertainty in the proposed surface velocity tracking includes: i) uncertainty due to the spatial resolution of the SAR image pair, and ii) uncertainty due to the co-registration error between these image pairs. The former is dependent upon the spatial resolution of the input SAR images while the latter is reported as the RMSE obtained after the DEM assisted co-registration (Section 4.2). The combined uncertainty is presented as a summation in quadrature which is ± 5.28 m/yr for both study periods being 2005-06 and 2014-15.

Figures 5.5a and b show the estimated and observed surface velocities along the glacier central flowline. Due to unavailability of field measurements for the same year, the estimated glacier surface velocity has been compared with the adjacent year's field observations. This is based on the assumption that annual velocity does not change significantly from year to year on this glacier. For both time periods, higher surface velocities were captured in the mid and upper zones of the glacier (Figures 5.5a and b), where a surge has been reported earlier

(Johnson and Kasper, 1992; De Paoli and Flowers, 2009). However, the lower zone which is nearly dormant has not been represented well for both time periods (2005-06 and 2014-15) as revealed by higher RMSEs in this zone (Table 5.1: South Glacier). From the spatial distribution of surface velocity estimates (Figures. 5.4a and b) and the comparative plot of the estimated and observed surface velocities (Figures. 5.5a and b), it is evident that the surface velocities are significantly overestimated in the lower zone. Here, a high value of deviation from the observed velocity in the surface velocity estimates can be attributed to the limitation of least measurable displacement at present level of sub-pixel precision ($1/4^{th}$ of a pixel) which exceeds the actual displacement (~0.5 m).

The zonal statistics of the surface velocity estimates for each time period are shown in Figure 5.5c. For all the zones, the min-max range were similar for both study periods. However, from mean surface velocities, it appears that for the year 2014-15 all the zones exhibited almost identical surface velocities, which is not consistent with the reported behavior of this glacier (Depaoli and Flowers, 2009). One of the possible reasons could be the distribution of window sizes ranging from 5×5 pixels to 20×20 pixels (Appendix-A2b) which are smaller compared to the window size distribution for period 2005-06, which is 5×5 pixels to 46×46 pixels (Appendix-A2a). These smaller window sizes (which are dominant in the lower zone) can introduce noise in the velocity estimates (Kanade et al., 1994). At the same time, for the year 2005-06, the upper and middle zones showed relatively higher mean velocities than the lower zone, as reported by DePpaoli and Flowers (2009).

For both study periods (2005-06 and 2014-15) similar overall RMSE values were observed (Table 5.1), in spite of the fact that the optical data used were of different wavelengths. Specifically, the ASTER band 3 (VNIR) was used for 2005-06 while the Landsat 8 PAN band was used for 2014-15. This shows that the proposed feature tracking approach is robust even when we use different optical datasets. As the SAR data used for these study periods are of the same wavelength (C-band), a similar investigation for different SAR wavelengths could not be performed due to unavailability of other SAR datasets and could be a matter of investigation for future studies.

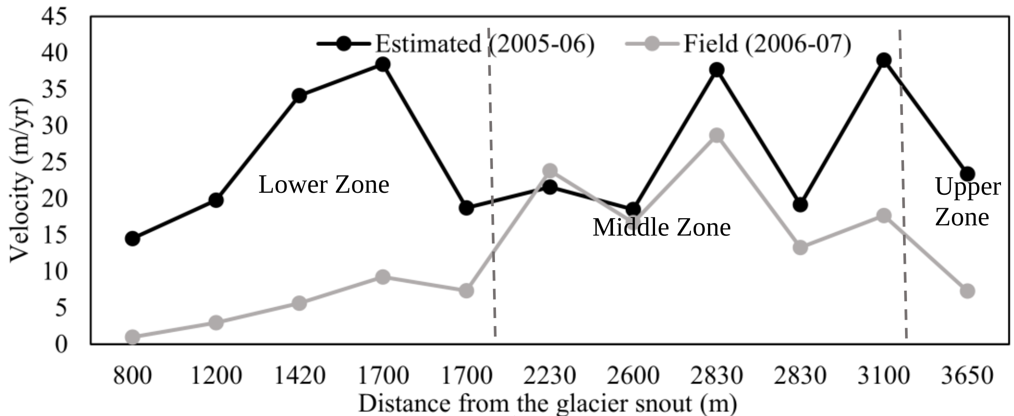

a)

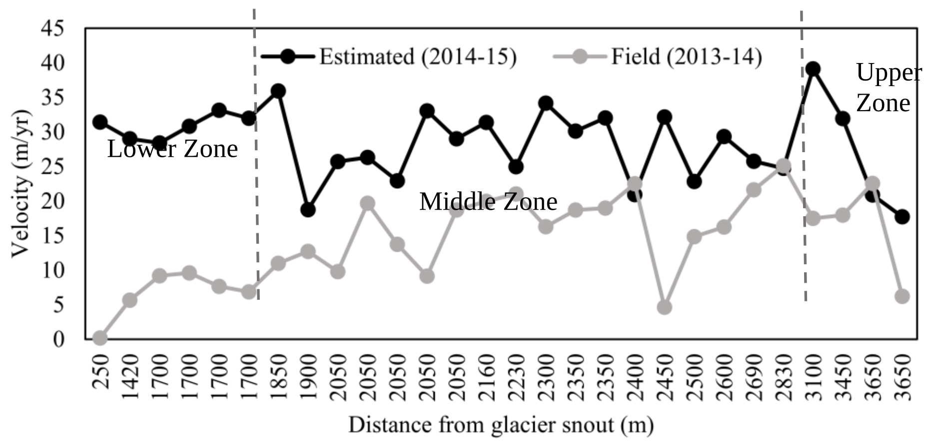

b)

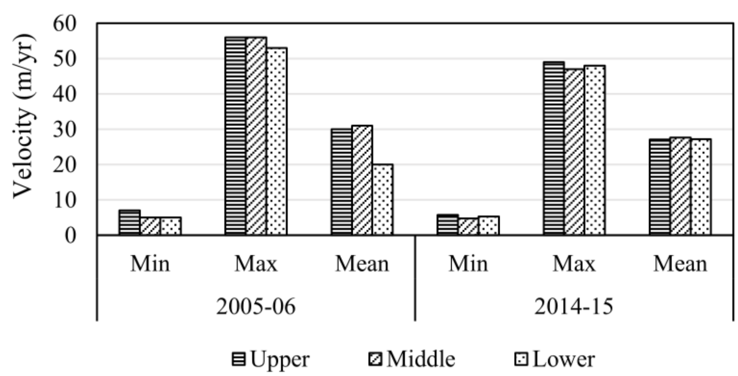

c)

Figure 5.5 Estimated velocities along the central flowline of South Glacier for period a) 2005-06 and b) 2014-15. The field measurements close to the study period are also shown (Flowers et al., 2011; Farinotti et al., 2017). c) Zonal statistics of South Glacier estimates

A significant decrease in feature tracking performance was observed when the window size for a given time period was used to estimate the surface velocities for other time periods, specifically when the temporal distance between those time periods was large. For example, using the 2005-06 window sizes for estimating velocities for the period 2014-15 led to significant degradation in feature tracking performance. This could be due to the significant changes in glacier surface conditions during this ten-year period, which is reflected in the different window size distribution for these periods (see Appendix- A2). This observation suggests that optical images selected for window size determination, when far apart from the study period, may fail to capture the glacier surface conditions during that period.

Table 5.1 Summary of zone wise RMSE of the proposed feature tracking approach for all three study glaciers. The overall RMSE and bias is also presented for each study period. The different zones are shown in Figures. 4.1(a-c).

Glacier	Period	Lower	Mid Zone	Upper	Overall	
		RMSE (m/yr)			RMSE (m/yr)	BIAS (m/yr)
South Glacier	2005-06	16	8	12.2	13.25	9.5
	2014-15	19	7	11.7	12.8	11
Chhota Shigri	2009-10	11.4	16.9	-	15.32	3.2
Tasman Glacier	2005-06	148.8*	41	-	71	28.81
	2007-08	48.1*	70	-	67.1	13.14

*RMSE has been calculated from one stake measurement.

Particularly if the glacier surface conditions have changed notably between this period i.e. study period and the selected time stamp of the optical image.This can degrade the performance of the proposed feature tracking approach. In general, this is not the case when the temporal separation between the optical images (used for window size estimation) and the SAR images (used for feature tracking) is approximately one year, provided there is negligible change in surface conditions. This finding implies that the choice of the time stamp of the optical image is a function of the change in glacier surface conditions. Figure 5.6 shows the glacier wide statistical distribution of velocity estimates for the period 2005-06 and 2014-15. The 2014-15 estimates show a slight acceleration (~13%) in mean velocity from 2005-06 estimates.

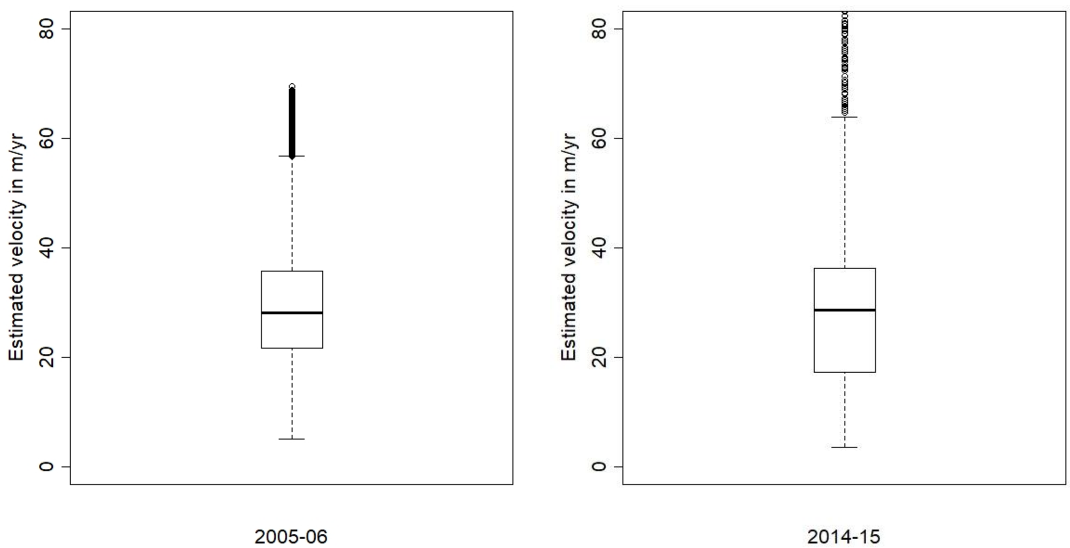

a) **b)**

Figure 5.6 Boxplot of surface velocity estimates of South Glacier for period a) 2005-06 and b) 2014-15.

5.2.2.2 Chhota Shigri Glacier

The surface velocity estimates for Chhota Shigri Glacier for the period 2009-10 have also been calculated using the proposed methodology and compared with the field based velocity measurements. Here the window size distribution has been calculated from IRS LISS-III imagery of Oct 13, 2009 (Table 4.3) supported by the fact that choosing either 2009 or 2010 imagery lead to similar velocity estimates. Figure 5.7a shows the spatial distribution of estimated surface velocity where higher surface velocities can be seen near the snout. Assuming a direct relationship between surface velocity and glacier ice thickness (Cuffey and Paterson, 2010), the peak velocity estimates in middle zone shown as circled areas 1 &

2 (Figure 5.7a) are in agreement with the maximum glacier ice thickness distribution estimated by Huss and Farinotti (2012).

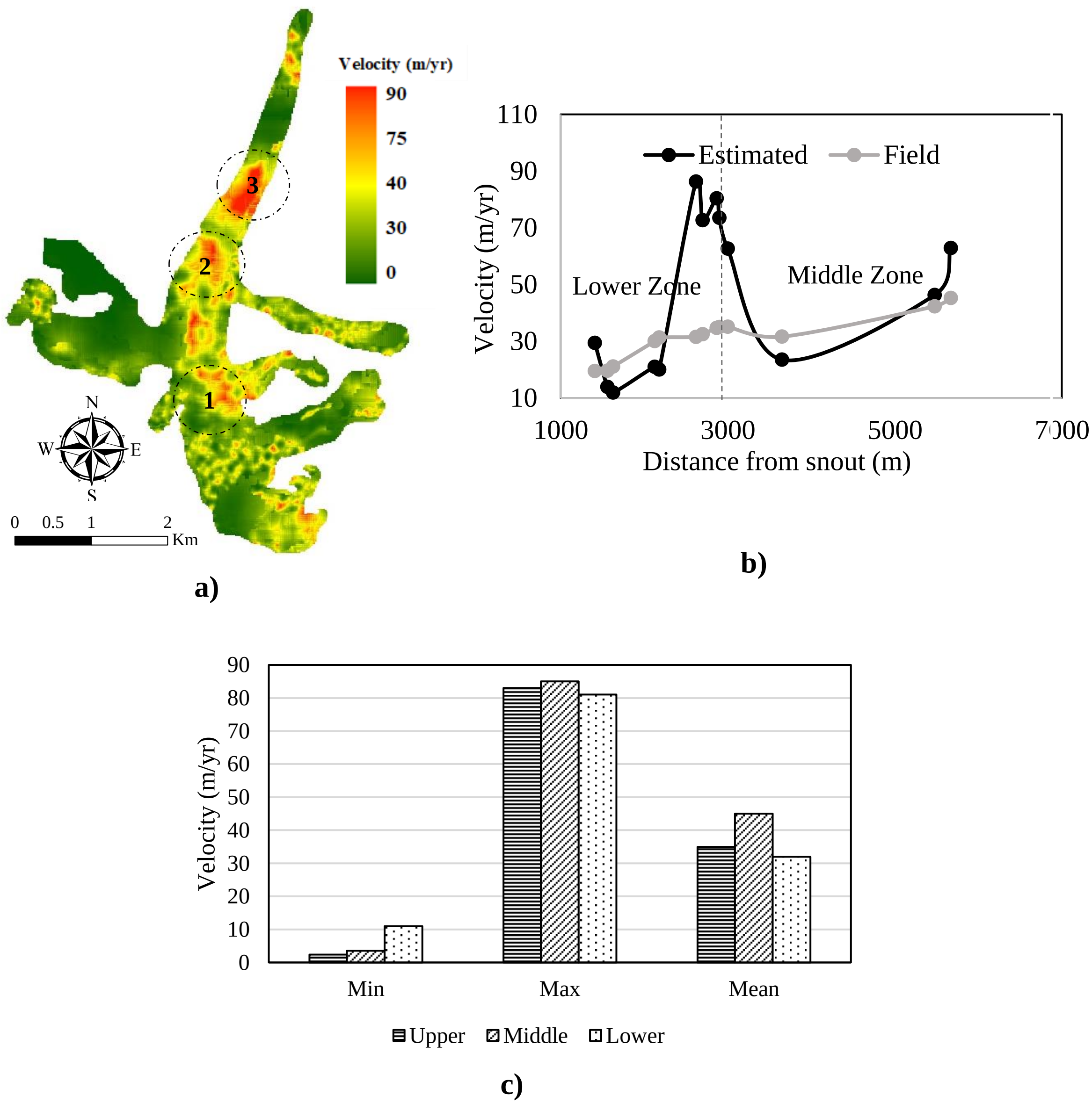

Figure 5.7 a) Spatial distribution of the estimated surface velocity for period 2009 -10 after smoothing. Circled areas of 1, 2 and 3 show the three zones with high velocity. b) Estimated and observed glacier annual surface velocity along the central flow line. c) Zonal statistics of Chhota Shigri Glacier velocity estimates for different zones.

However, the circled area 3 in the lower zone shows a very high surface velocity trend, which is not in agreement with the ice thickness estimates reported by Huss and Farinotti (2012). These high values appear to be an indication of an external contribution (like avalanches/landslide) during the study period leading to significant changes over the glacier surface which is reflected as the erroneous surface velocity estimates. The presence of active avalanches/landslide sites (see Appendix-A1) in the lower zone has been verified by observations made during visits to Chhota Shigri Glacier by field experts.

Figure 5.7b shows comparison of surface velocity estimates with the field measurements along the central flow line of the glacier. It should be noted that the distance is measured from the snout of the glacier. There is a huge difference in the estimated and observed surface velocity at a distance of 2500-3000 m from the snout (Figure 5.7b), which also coincides with circled area 3 in Figure 5.8a. The overall RMSE of surface velocity estimates of the Chhota Shigri Glacier (excluding the circled area 3) was 15.32 m/yr, whereas the overall bias was 3.2 m/yr (Table 5.1: Chhota Shigri Glacier). Likewise, the uncertainty in the surface velocity estimation for this glacier (i.e. ± 3.9 m/yr) has been calculated in a similar manner as that for South Glacier.

Figure 5.7c shows the zone wise statistics of the surface velocity estimates. The min–max range of estimated velocities lie within the range of previously reported estimates for this glacier by Gantayat et al. (2017). However, the maximum velocity in the lower zone was high (~80 m/yr) when compared with field values in this zone (~30 m/yr), as shown in Figure 5.7b. The possible reason has been discussed earlier in this section pertaining to the circled area 3 (Figure 5.7a). The estimated mean velocity in the upper, middle and lower zones are 35 m/yr, 45 m/yr and 32 m/yr respectively (Figure 5.8c). The mean of lower zone estimates (32 m/yr) and the middle zone (45 m/yr) were found to be close to the observed velocities in the respective zones (20-35 m/yr in the lower zone; 35-45 m/yr in the middle zone). The upper zone estimates could not be evaluated because of unavailability of field measurement over this zone.

A number of studies have reported mean surface velocity (annual) of Chhota Shigri Glacier for intermittent periods between 1987 and 2010. The surface velocity estimates obtained by the proposed method agree with this reported trend as shown in Figure 5.8. It is also observed that the mean velocity of this glacier has not changed much during these 23 years indicating that the glacier is more or less stable.

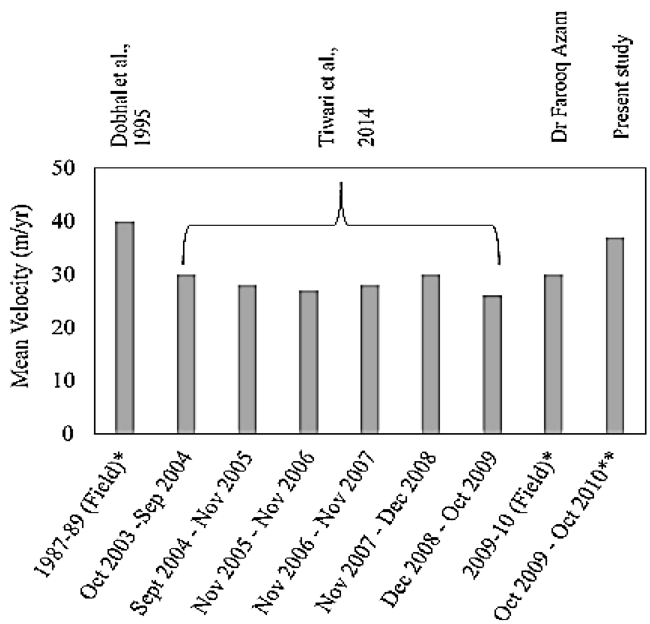

Figure 5.8 Glacier wide mean surface velocity trend of Chhota Shigri Glacier (field and estimated) for period 1987-2010. The glacier surface velocity estimates (period Oct 2003-Oct 2009) are taken from Tiwari et al., 2014. *Field measurements are taken from Dobhal et al., (1995) (period 1987-89) and Dr Farooq Azam (period 2009-10). **Estimated mean glacier surface velocity by the proposed method (Oct 2009 - Oct 2010).

The knowledge of Chhota Shigri Glacier's surface conditions and flow behavior from field experts has made it possible to further analyze the directional aspects of the velocity estimates. The direction of surface velocity estimates shows an agreement with the aspect direction (Figure 5.9b) along the main trunk of the glacier, which follows Northwest-North-Northeast directions. However, the direction in the tributary in regions I & III (Figure 5.9a) was not well captured, which shall be attributed to large displacements in these regions due to steep slopes. The directional behavior of the estimated surface velocities in region II is interesting (Figure 5.9a), because it highlights the presence of a number of avalanche-prone cliffs to the right, contributing to apparent periodic glacier flow. There are four sites in region II which are affected by avalanches/landslide (see Appendix- A1) as identified from the Google Earth image collections available during the study period. Thus, in region II the dominant direction of the surface velocity is obtained as the Northwest direction instead of the North direction as represented by the aspect map (Figure 5.9b).

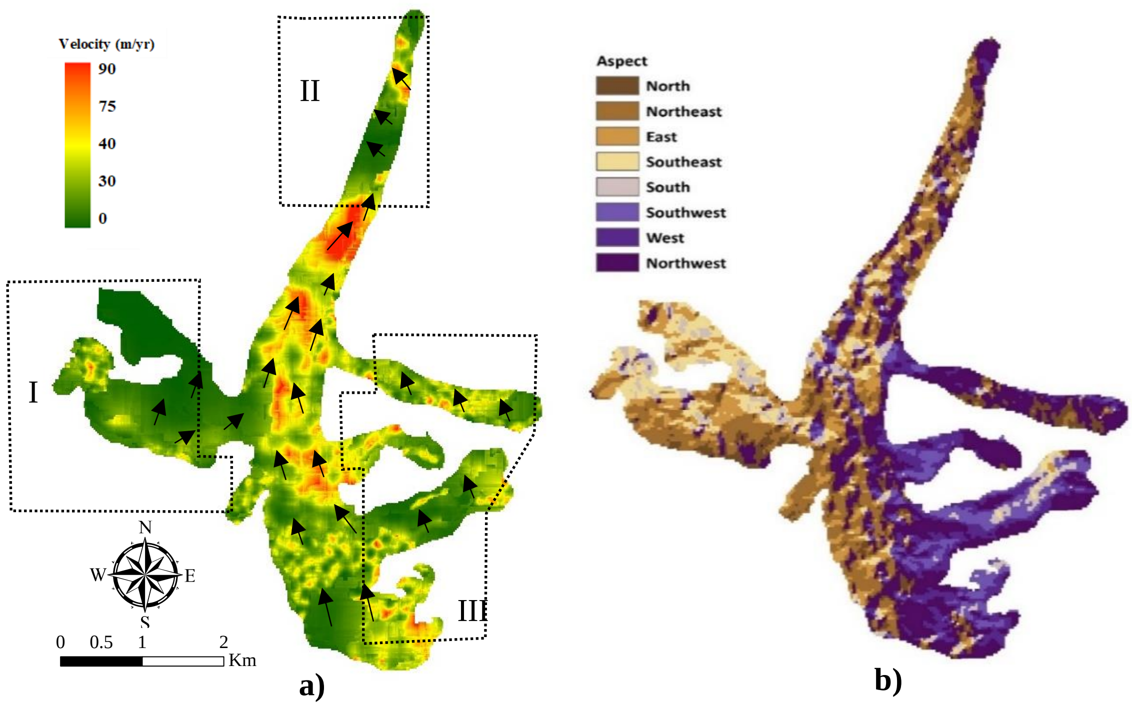

Figure 5.9 a) Direction of the estimated velocity of Chhota Shigri Glacier during the year 2009-10. The direction are shown at 300m spacing. Regions I, II and II indicate the areas with estimated flow direction mismatches the aspect map. b) Aspect map of the glacier.

5.2.2.3 Tasman Glacier

The spatial distributions of the estimated surface velocities for the period 2005–06 and 2007–08 are shown in Figure 5.10. Due to scarce cloud-free optical images during the study period, a common optical image (Dated: Jan 24, 2006) was used to calculate window size for both study periods. A smooth transition of glacier velocity is observed from the glacier head to the terminus. However, a few noisy patches near the confluence zone (Figures. 5.10a–b) can be easily seen, indicating mismatches in the estimated and observed values.

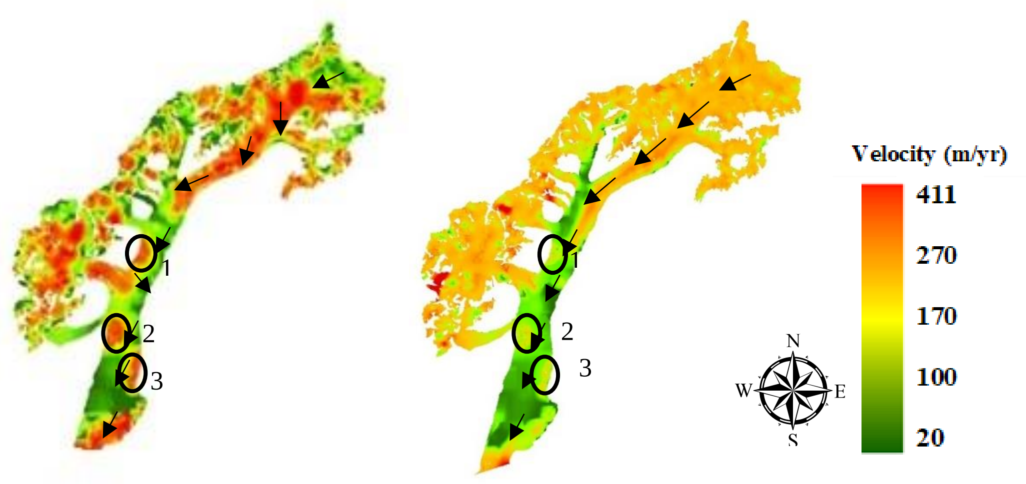

(a) (b)

Figure 5.10 Spatial distribution of velocity estimates of Tasman Glacier for a) period 2005-06 using Envisat C-band VV polarized data and b) period 2007-08 using ALOS PALSAR L-band HH polarized data. Circled areas 1, 2 and 3 (in black) represent erroneous patches with unrealistic high surface velocity values.

A few gaps have been found in the estimates across the debris-covered regions of the glacier. Upon close inspection, these are the same regions in which segmentation has resulted in large segments due to merging of glacier segments with the background area of the glacier, as shown in Figure *5.2*. While setting a limit on the maximum window size led to a large reduction in gaps, it also eliminated high values of surface velocity estimates (>1000 m/yr). The surface velocity estimates of the proposed method were compared with a) a spatially distributed long-term decadal surface velocity map for the period 2000-2011 (Farinotti et al., 2017), derived from field measurements as well as remote sensing based estimates (for more details readers are referred to Purdie et al., 2018) and b) point-wise field measurements collected during 2007-09 (Purdie et al., 2018).

The difference between the obtained surface velocity estimates and the spatially distributed decadal velocity estimates (considered as reference) given by Farinotti et al. (2017) are shown in Figures 5.11a-c. Figure 5.11a shows the difference map for the period 2005-06 where the velocity was estimated without limiting the window size. After limiting the maximum window size, the velocity estimates for the same period were compared with the reference velocity map and the resulting difference map shown in Figure 5.11b.

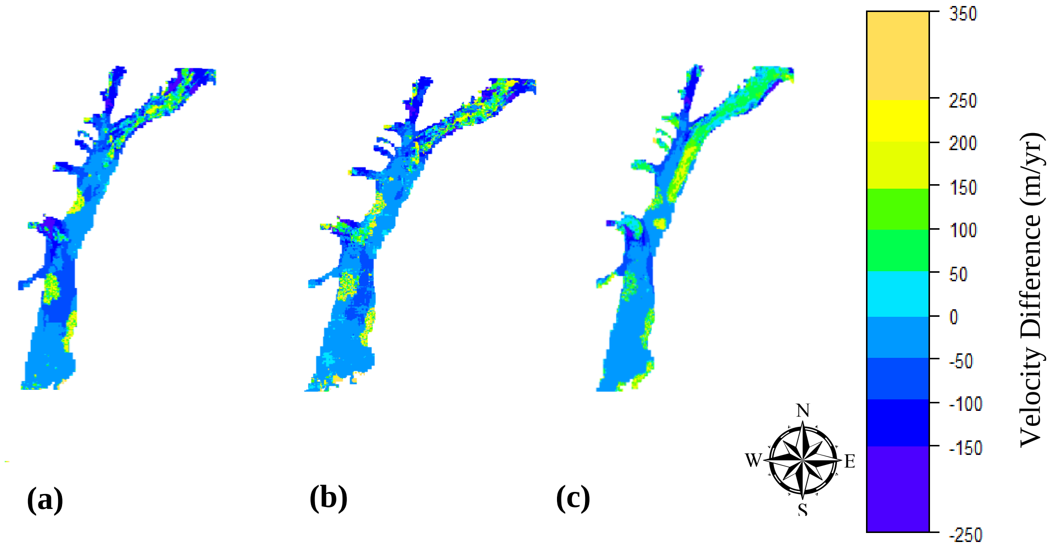

Figure 5.11 Difference between the velocity estimates and reference velocity (source: Farinotti et al., 2017), where the velocity estimates have been calculated for a) 2005-06 using Envisat (C-Band) without limiting the maximum window size, b) 2005-06 using Envisat (C-Band) after limiting the maximum window size. c) 2007-08 using ALOS PALSAR (L-Band) after limiting the maximum window size. Positive values show the overestimation and negative values show underestimation by the proposed approach.

Setting a limit on maximum window size shows significant improvement in the velocity estimates as the velocity difference reduced from ~300 m/yr to ~150 m/yr (Figures. 5.11a and b). Therefore, for the period 2007-08 the surface velocities were estimated only after limiting the maximum window size and plotted. The corresponding difference map with reference velocity is shown in Figure 5.11c. Estimates for 2007-08 (Figure 5.11c) showed a smoother transition between the different velocity ranges, as expected from an ideal glacier flow. This could be due to higher signal penetration of L-band (used for 2007-08 estimates), which gives less noisy velocity estimates when compared to C-band (used for period 2005-06).

It appears that the high difference (e.g., figure 5.11b and c) is more likely due to the noise issues in the original data (pre-processing) than feature tracking mismatch. The reason being, for different data type (C-band: figure 5.11b and L-band: figure 5.11c) the magnitude of errors in estimated velocities vary.

Following this, a point-wise comparison of the proposed method with field measurements (Purdie et al., 2018) is shown in Figure 5.12. For the study period 2005-06, large deviation from field data was observed in the lower zone, which also represents the debris cover region with erroneous patches 1, 2 & 3 (Figure 10a). The estimates for period 2007-08 were consistently closer (for lower as well as middle zones) to the field measurements.

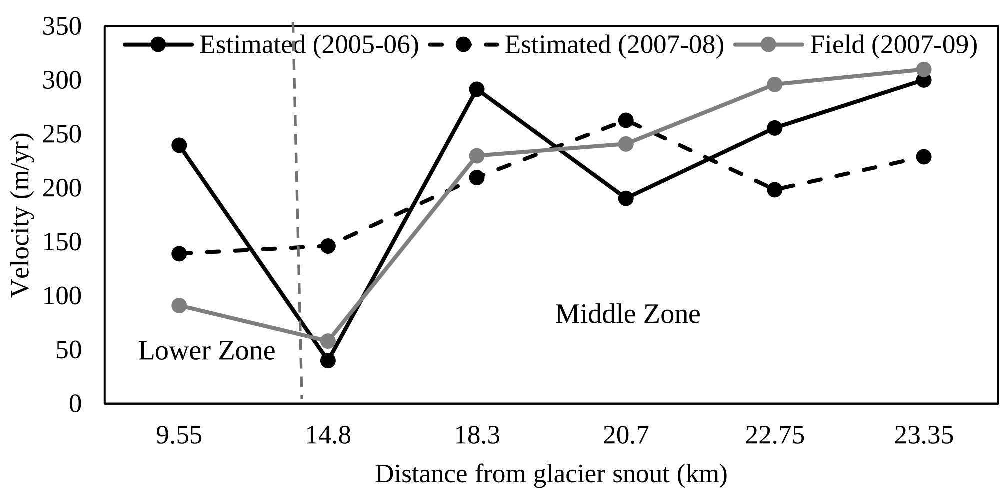

Figure 5.12 Estimated velocities of Tasman Glacier for period 2005-06 and 2007-08 compared with the field measurements close to the study period (source: Purdie et al., 2018).

The overall RMSE for Tasman Glacier (Table 5.1) during 2005-06 and 2007-08 was 71 m/yr and 67.1 m/yr respectively. Overall, the bias of the velocity estimates for period 2005-06 and 2007-08 was 28.81 m/yr and 13.14 m/yr respectively (Table 5.1). The uncertainty in velocity estimates for the period 2005-06 was 5.14 m/yr. For the period 2007-08 the uncertainty in the velocity estimates was 0.14 m/yr. The uncertainty for this period was very low because the uncertainty due only to spatial resolution of SAR imagery has been reported, while the uncertainty due to co-registration error could not be reported. Here, the error in co-registration could not be calculated for the particular image pair because the DEM based co-registration was not performed on the SAR images (Chapter 4), and because the Ground Control Points (GCPs) were not available.

Zone wise statistics of the surface velocity estimates are shown in Figure 5.13. In each zone, estimates for the period 2005-06 showed a higher range of velocity (min-max), pertaining to the presence of noise (Figure 5.10b). The mean in the lower zone (also the debris covered zone) was well represented for both periods 2005-06 and 2007-08. In this zone, the mean estimates for both periods 2005-06 and 2007-08 were closer to observed velocity (Table 5.1: Tasman Glacier), showing the reduced effect of the erroneouos patches (Figure 5.10a and b).

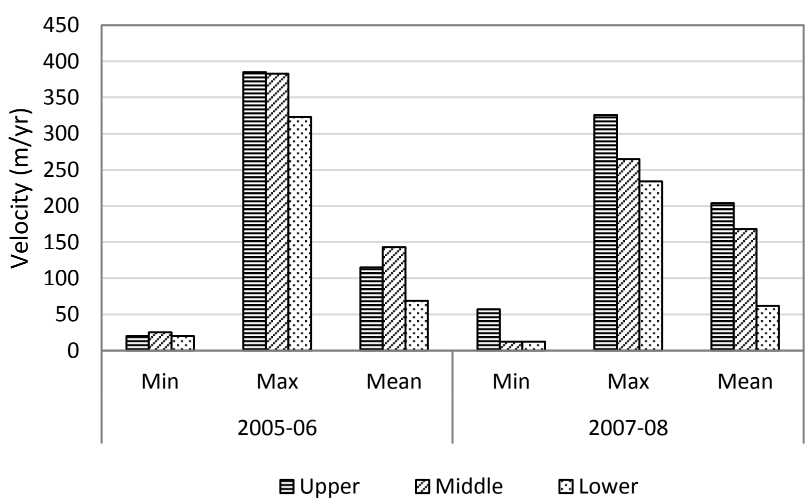

Figure 5.13 Zone wise mean velocity estimates for the Tasman Glacier.

Use of a common optical image for both study periods 2005-06 and 2007-08 has aided to investigate the effect of different SAR data on the proposed feature tracking performance.

The Tasman Glacier is a relatively smooth (less steep) glacier whose surface velocity has been reported to have no measurable change during 2002-05 (Herman et al., 2011).

Assuming that during 2005-2008 there were no significant changes in glacier flow behavior, the effect of SAR wavelength on the feature tracking has been investigated. It is interesting to see that L-band (Figure 5.13: Estimated (2007-08)), which has more penetration through the glacier, captured the surface velocity more accurately as compared to the C-band based estimates (Figure 5.13: Estimated (2005-06)). A higher value of RMSE and bias in the C-band estimates can be attributed to the sensitivity of C-band for surface roughness. The effect of SAR polarization could not be studied due to unavailability of different polarization data in L- and C-Band products for the study period (Table 4.3).

5.2.3 Effect of the Difference between Spatial Resolution of Optical and SAR Data

To study the impact of difference between optical and SAR data resolution on the estimated glacier velocity, two sets of SAR-optical pairs were assessed. The first set (case 1) represents the data for South Glacier during 2005-06 where the optical data resolution was 30 m and SAR resolution was 20 m. The other set (case 2) represents the data for South Glacier during 2014-15 where the resolution of both optical as well SAR was the same i.e. 15 m. Considering that both the SAR data in case 1 and 2 are C-band, if assumed to be the same, and the difference in the quality of velocity estimates (between case 1 and 2) is mainly due to the resolution of optical imagery.

In case 1, the optical imagery of coarser resolution (with respect to SAR data) led to better estimates both in terms of magnitude and direction of estimated velocity (Figure 5.5 a). However, in case 2, the optical imagery of similar resolution (with respect to SAR data) led to poorer velocity estimates both in terms of magnitude and direction (Figure 5.5 b) and Similarly, higher error in the stable region outside the glacier (Table 5.2) was observed for case 2. The difference between these two cases is that due to finer resolution of optical imagery (in case 2), the smaller surface feature may also be visible which can not be seen in the case 1 imagery. However, these smaller features have a higher tendency to change over time and thus leading to error in the estimates. On the other hand the coarser optical imagery may have led to more smooth features which are less likely to introduce error in the estimated velocity. Moreover, the coarser resolution optical imagery and comparatively higher resolution SAR data can be expected to work in sync due to the penetration capability of SAR data which also reduces the effect of surface features leading to error in estimated velocity. Although it is theoretically convincing that a coarser image would produce smooth velocity and fine resolution may introduce errors, an attempt was made in this study to evaluate it in a quantitative manner when there is a difference of spatial resolution in input data (optical and SAR).

5.2.4 Validation Over Stable Terrain

Another component for validation of estimated glacier surface velocity is analysis over stable ground. Here, the ice-free ground outside the glacier is assumed to be stable (Altena et al., 2019; Sattar et al., 2019) and the estimated displacements for each study glacier over this stable region summarized in Table 5.2. The median 95% confidence interval was found to be 3.7 m/yr (for all the three study glaciers combined) in stable areas. This average displacement obtained in the stable area are well within the acceptable limits considering the range of velocity for the study glacier between ~30-150 m/yr. This estimated velocity in the stable area can be due to errors present in 1) the feature tracking method or 2) ionospheric errors in the input dataset (Yan et al., 2013).

Table 5.2 Estimated displacements for each study glacier over stable region.

Glacier	**Study Period**	**Estimated velocity in stable areas (at 95% confidence interval) in m/yr**
South Glacier	2005-06	2.4
	2014-15	3.9
Chhota Shigri Glacier	2009-10	4.2
Tasman Glacier	2005-06	3.9
	2007-08	4.4

The datasets used in the study vary in terms of sensors and processing quality and thus may exhibit different level of ionospheric errors associated with them. The highest estimates were observed for Tasman Glacier for the period 2007-08 (4.4 m/yr) where the L-band SAR data used is expected to contribute to errors due to higher sensitivity to ionospheric errors (Meyer and Nicoll, 2008).

5.2.5 Performance Evaluation against Normalized Cross Correlation (NCC) Method

The performance of the proposed ML-based feature tracking method with spatially varying window size has been compared with the cross-correlation-based method that has a spatially invariable window size. The NCC was chosen to compare the results from the proposed feature tracking algorithm since it is most widely used. Both methods perform image-matching in the spatial domain. The latter is based on the normalized cross-correlation (NCC) image analysis that was implemented in Correlation Image Analysis Software (Heid and Kaab, 2012). The same SAR data pairs (Table 4.3) have been used in both methods. Since the proposed method uses a spatially varying window size for image matching, the NCC-derived estimates have been calculated for different standard window sizes (32 x 32, 64 x 64, and 128 x 128 pixels) and subsequently compared with the proposed method. The search window size was maintained at 100 x 100 pixels for both the NCC and the proposed method. Any gaps in NCC estimates were filled using the Inverse Distance Weighted (IDW) interpolation. This analysis was performed for all three study glaciers for the available dataset (Table 4.3). Although, the NCC estimates at different window size (32 x 32 pixels, 64 x 64 pixels, and 128 x 128 pixels) have been used for comparison (See Appendix- A4), to ease the interpretation only the best performing window size (NCC) for each glacier and the proposed method’s estimates are shown in Figures. 5.13a to c.

A summary of zone wise and overall RMSE of the NCC based approach for the study glaciers is given in Table 5.3. Comparison of the RMSEs from Table 5.1 and Table 5.3 indicates that the middle and upper zone were estimated more accurately by the proposed approach than the NCC based approach, where the NCC approach tends to fail due to low contrast (increased snow cover) on the glacier surface. However, the NCC estimates outperformed the proposed approach in the lower zone of the South Glacier. For the lower zone of the Tasman Glacier, similar conclusions could not be derived because the RMSEs were calculated from only one stake measurement. Here, the proposed method was observed to be sensitive to highly textured areas, especially the lower zone which is a highly textured zone due to debris cover and/or surface melting. This observation is also conveyed in Figures 5.14a to c. Overall, when compared with the best results of the NCC method (which requires calibration), the proposed approach was in close agreement for the South Glacier and performed better in case of Chhota Shigri Glacier and Tasman Glacier (Table 5.1 and Table 5.3).

It is noteworthy that the best window size in the NCC method was different for each glacier (Figs 5.14(a-c)); it can be obtained only in the presence of field measurements; and it is spatially invariant over the glacier surface. Conversely, the window size used in the proposed approach is automatically identified; it does not require field measurements; and it varies over the glacier surface. This demonstrates the advantage of the proposed approach over the NCC-based approach.

Apart from CIAS, another NCC based method (COSI Corr) provides an option of varying the window size, e.g., initial can be 128 and final can be 32 with user-defined step for changing window size. However, this variation (user-defined step) is limited to powers of 2 (2^2, 2^3, 2^4… and so on). Moreover, the output is still generated using a spatially fixed window size which lies between the initial and final window size. Moreover, this method implies application of NCC in the Fourier domain, whereas the proposed feature tracking method works on the spatial domain. If comparing the proposed method (in spatial domain) and NCC (in Fourier domain), the results may differ due to the domain itself. As the aim here is to assess the improvement due to spatially distributed window size, the comparison in different domain (COSI Corr) does not seem useful here and it has not been performed in the study.

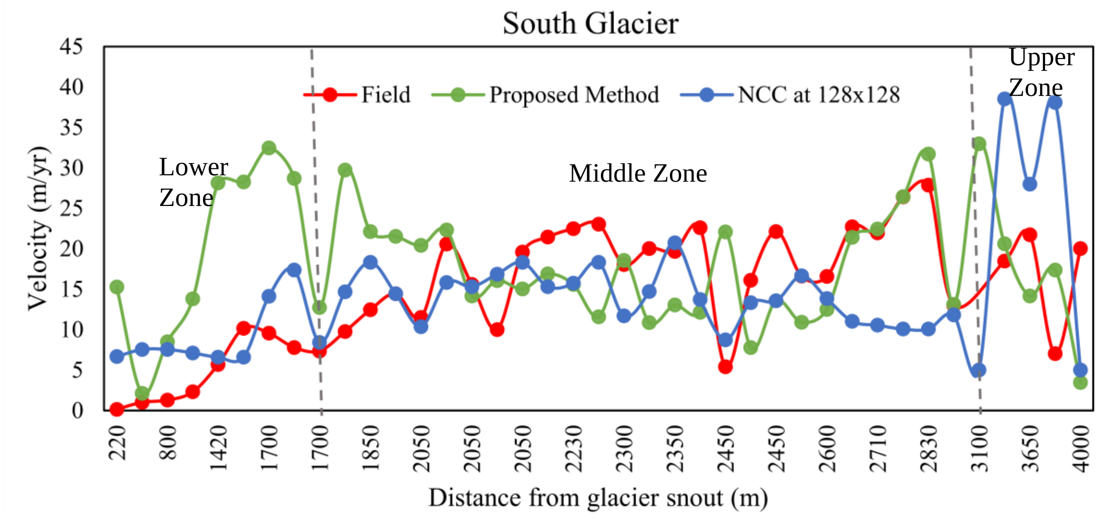
South Glacier
Field
Proposed Method
NCC at 128x128
Lower Zone
Middle Zone
Upper Zone
Velocity (m/yr)
45
40
35
30
25
20
15
10
5
0
220
800
1420
1700
1700
1850
2050
2050
2050
2230
2300
2350
2450
2450
2600
2710
2830
3100
3650
4000
Distance from glacier snout (m)

a)

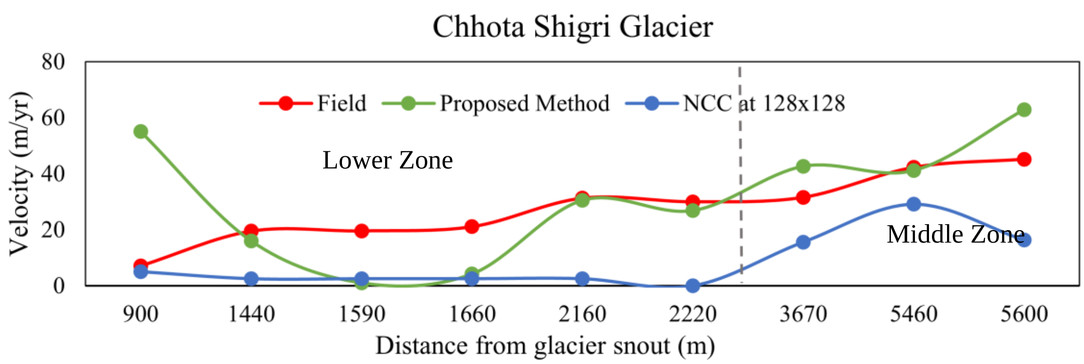
Chhota Shigri Glacier
Field
Proposed Method
NCC at 128x128
Lower Zone
Middle Zone
Velocity (m/yr)
80
60
40
20
0
900
1440
1590
1660
2160
2220
3670
5460
5600
Distance from glacier snout (m)

b)

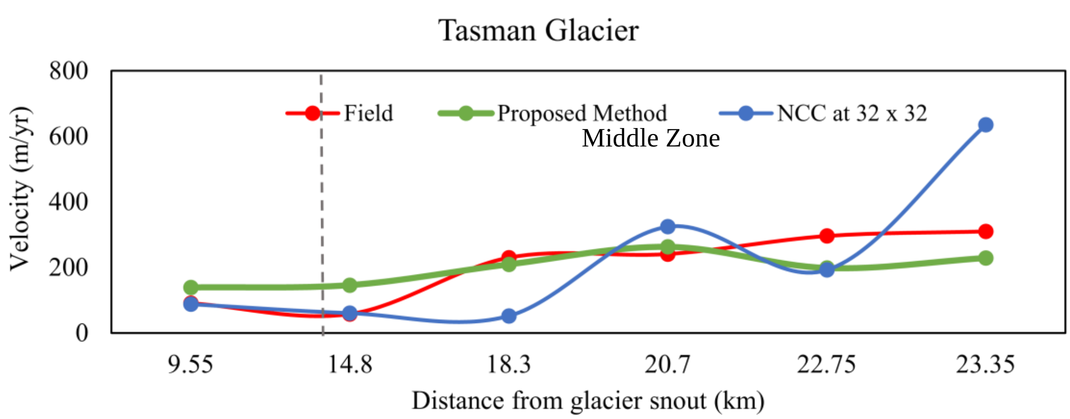
Tasman Glacier
Field
Proposed Method
NCC at 32 x 32
Middle Zone
Velocity (m/yr)
800
600
400
200
0
9.55
14.8
18.3
20.7
22.75
23.35
Distance from glacier snout (km)

c)

Figure 5.14 A comparative plot of proposed velocity estimates and cross correlation based velocity estimates (at best performing window size) of: a) South Glacier for period 2005-06, b) Chhota Shigri Glacier for period 2009-10, and c) Tasman Glacier for period 2007-08.

Table 5.3 Zone wise RMSE of the normalized cross correlation (NCC) based method CIAS (at best performing window size) for the study glaciers.

Glacier	Period	RMSE (NCC) in m/yr			
		Lower Zone	Mid Zone	Upper Zone	Overall
South Glacier	2005-06	5.5	7.3	18.2	9
	2014-15	5.4	14	11	12.8
Chhota Shigri	2009-10	20.5	21	-	20.8
Tasman Glacier	2005-06	2.4*	115.8	-	105
	2007-08	2.9*	175.9	-	160

*RMSE has been calculated from one stake measurement.

5.2.6 Comparison with Spatially Fixed Window Size-Based Maximum Likelihood Feature Tracking

To investigate any possible improvement due to a spatially varying window size, the performance of the proposed ML-based feature tracking method having a spatially varying window size (SVWS) has been compared with the spatially fixed window size (SFWS) implemented with the same ML-based feature tracking method. The same SAR data pairs (Table 4.3) have been used in this analysis. For the latter method (i.e. SFWS) the standard window sizes have been used (32 pixels × 32 pixels and 64 pixels x 64 pix pixels). Unlike the previous comparison made in Section 5.2.3, the SVWS performed consistently better in all three zones for all three study glaciers (Figure 5.15).

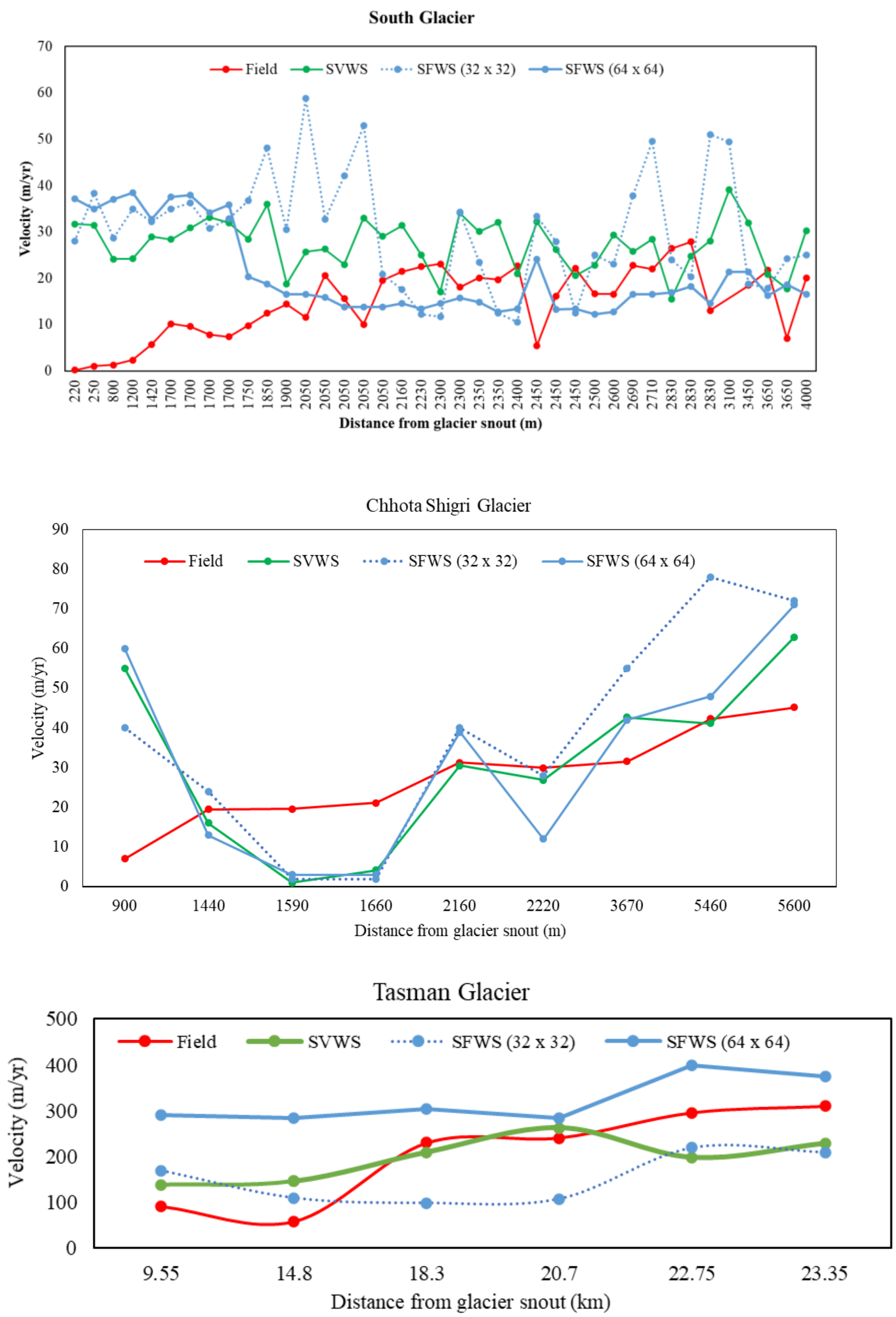

Figure 5.15 A comparative plot of proposed velocity estimates at spatially varying window size (SVWS) and spatially fixed window size (SFWS): a) South Glacier for period 2005-06, b) Chhota Shigri Glacier for period 2009-10, and c) Tasman Glacier for period 2007-08.

For South Glacier, the spatial distribution of field measurements was well spread across the glacier covering each zone (lower, middle, and upper). The smaller window size gave closer estimates to the field measured velocity in the lower zone and the larger ones gave closer estimates to the field measured velocity in the upper zone.

SVWS gave a variety of window sizes in addition to the standard window sizes (32 x 32 pixels or 64 x 64 pixels etc), being what existing feature tracking software (such as COSI-Corr and SARscape) provide, thus facilitating more flexibility in the feature tracking.

5.3 Summary

An automated and spatially varying feature tracking algorithm useful for glacier surface velocity estimation was presented. The proposed algorithm considers both optical (for window size estimation) and SAR data (feature tracking) to estimate glacier surface velocities. The proposed method uses spatially varying window size and is different from the existing variable window size techniques (Heid and Kaab, 2012) where the window size can be varied at different iterations but still the window size is spatially fixed or invariant. The feature tracking algorithm was tested for three study glaciers.

The proposed feature tracking method was evaluated for any possible impact of input data characteristics on the estimated glacier surface velocity. The characteristics of input data taken into consideration were the difference in the spatial resolution of input data and the timestamp of the data.

Comparison of the velocity estimates using proposed method and the normalized cross correlation based revealed improvements due to the proposed method. Zone wise analysis revealed the better performance of the proposed approach in the middle and upper zones while in the lower zone, the method gave relatively higher RMSEs when compared to the best performing NCC (CIAS) estimates. Here, the main advantage of the proposed approach is the automated estimation of spatially varying window size. Thus, by applying this technique will serve a relatively better estimate for glacier specific window sizes could not be obtained. Moreover, when compared with spatially fixed window size based feature tracking, the proposed spatially varying method gave better velocity estimates for each of the three study glaciers.

The feature tracking algorithm focuses on automation rather than computational efficiency. However, computationally, this tracking approach does not pose any severe limitations and it is dependent upon the size of the glacier and the window size generated. For example, with a 4.6 GHz Intel® Core i7- 8700 CPU of 16 GB RAM, the total Central Processing Unit (CPU) time (applicable to both parallel and serial processing) may vary from several minute to few hours because of the spatially varying window size and glacier size. Similar to other NCC based methods, large intra annual changes on the glacier surface and co-registration errors are the factors that limit the accuracy of this feature tracking approach. Nevertheless, the proposed glacier feature tacking method holds potential for regional and global scale feature tracking in glaciers with no prior field information available.

6 Modelling of Glacier Ice Thickness

This chapter presents the ice thickness estimation modelling framework, its application, and assessment. The estimation capabilities have been explored via the performance analysis for four study glaciers. Seeking for the possible improvements towards data scarce as well as data deprived glacier ice thickness modeling, a number of experiments has been designed and evaluated.

6.1 Ice Thickness Modelling Framework

The proposed glacier ice thickness model consists of estimating a distribution of the glacier surface velocity mentioned in Chapter 5, using which the ice flux was computed. The flux was then converted to an ice thickness using Glen's flow law (Glen, 1958) and represented over the entire glacier. The theoretical background is as follows:

According to the principle of mass conservation (Eq. 6.1), the mass-balance distribution *b* (m/yr), should be balanced by the ice-flux divergence ($\frac{dq}{dx}$) where *x* represents distance along the flowline direction. Moreover, the residual should reflect in surface elevation change with time *t* ($\frac{dh}{dt}$) of the glacier.

$$\frac{dq}{dx} = b - \frac{dh}{dt} \tag{6.1}$$

dh/dt is the rate of ice-thickness change expressed in m/yr, *b* is the annual mass gain or loss (mass balance) at the surface in m.w.e and *q* is the ice flux. The ice flux divergence $\frac{dq}{dx}$ (in m/yr) in Eq. 6.1 can also be calculated from Eq. 6.2, where the right hand side term denotes the apparent mass balance (Hooke, 2005).

$$\frac{dq}{dx} = -w_s + u_s tan\alpha \tag{6.2}$$

where w_s=vertical velocity (m/yr), u_s=horizontal velocity (m/yr), α = slope of the glacier surface. The ice thickness at a pixel *i* (h_i) can then be inferred from the mean specific ice fluxes at corresponding pixel *i* ($\overline{q_i}$) by inversion of Glens flow law using Eq. 6.3

$$h_i = \sqrt[n+2]{\frac{\overline{q_i}(n+2)}{2A(f\rho g sin\alpha)^n}} \tag{6.3}$$

where, α is the glacier surface slope, ρ and g are constants and denote the ice density and acceleration due to gravity, respectively. The other parameters A (flow rate factor), n (Glen's law exponent) and f (shape factor) are calibration parameters.

Figure 6.1 shows the proposed methodology for estimation of the spatially distributed glacier ice thickness using remotely sensed inputs. The estimated glacier surface velocity (Chapter 5) was used as one of the inputs to the ice thickness model as u_s. Similarly, another input w_s was estimated following the workflow given in Figure 6.1 and additionally following Yang et al., (2020) to calculate the vertical component of the surface velocity (w_s). Overall, the 3D displacement was determined using the azimuth and line of sight offsets derived from ascending and descending imagery. The 3D displacement was calculated by solving for the equation in matrix form (Yang et al., 2020),

$$\mathrm{BX} = \mathrm{L} \tag{6.4}$$

where B is a function of azimuth angle and look angle of the SAR imagery, X represents the three-dimensional displacement (north, east and vertical direction) and L represents the displacements in line of sight displacement and azimuth displacement for ascending and descending pass.

Following Farinotti et al., (2009), the calculated flux (q_i) was normalized with the local glacier width that is relevant for the ice discharge in order to obtain the mean specific value of the ice flux ($\overline{q_i}$) along the central flowline. The other input i.e. the DEM was taken from the freely available DEMs (Chapter 4) over the study glaciers. The difference in timestamp of input data and the field measured data may introduce some error in the estimates caused by the surface changes occurring during the time period. To eliminate this error, the glacier surface topography (represented by DEMs) has been adjusted to compensate for any temporal changes in the glacier surface elevation. This adjustment was performed using the reported ice thickness change values (in m/yr) for the study glaciers close to the study period.

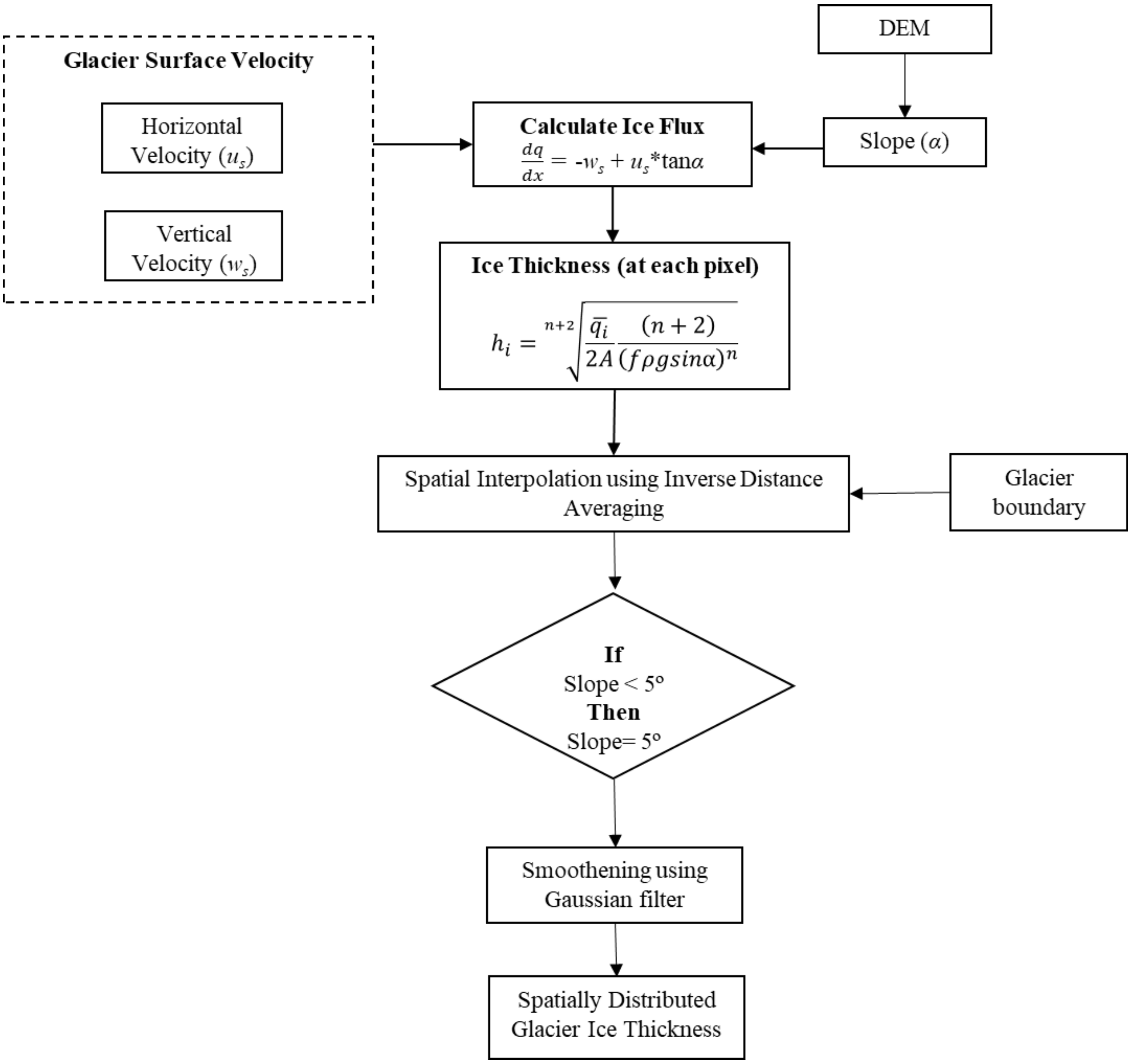

Figure 6.1 Proposed methodology for estimation of spatially distributed glacier ice thickness using remotely sensed inputs.

The physics-based glacier ice thickness models based on Shallow Ice Approximation, such as the one proposed in this study neglects the transverse stresses which come into play near the glacier side walls but do not dominate near the central flowlines. Under this assumption it is valid to say that the model results are expected to agree well near the glacier central flowline. To estimate a glacier wide distributed ice thickness, the ice thickness distribution has been synthesized according to the expected (a parabolic) cross-sectional profile geometry. Following Farinotti et al., (2009), the spatially distributed glacier ice thickness for the study glaciers has been estimated using interpolation technique. Here, the modelled ice thickness at the central flowline was interpolated to get spatially distributed glacier ice thickness. An inverse distance averaging technique was used for interpolation, weighting the individual interpolation nodes with the inverse of the squared distance from the considered point. Here, the glacier outline is used as a boundary condition with zero ice thickness. The local surface slope is filtered with a lower slope limit of 5° to prevent an overestimation of ice thicknesses in very flat zones. Finally, the calculated ice thickness is smoothed with a Gaussian filter to remove any outliers.

6.1.1 Model Parameters

In this section, the characteristics and commonly observed range of values of the three model parameters are described.

6.1.1.1 Flow Rate Factor (A)

The flow rate factor A appears in the Glen's flow law where shear stress τ is related to shear strain rate by a power law. It depends on temperature, crystal fabric, water content, and other variables, A can be represented by the relation

$$A = A_* \exp(-\frac{Q_c}{R}\left[\frac{1}{T_h} - \frac{1}{T_*}\right]). \qquad (6.4)$$

Where $T_* = 263+7\times10^{-8} P$; $T_h = T + 7\times10^{-8} P$; $Q_c = Q_-$ if $T_h < T_*$; $Q_c = Q_+$ if $T_h > T_*$.

Here T denotes Kelvin temperature. The coefficient A_* is the pre-factor, and Q_- the low-temperature activation energy for creep distinct from the effective activation energy above -10 ºC, is referred to as Q_+. A_* is the value of A at -10 ºC and Q_+ the apparent activation energy in warm ice (T > -10 ºC), are calibration parameters which have been identified through several modelling (for glaciers and ice sheets) based studies (Cuffey and Paterson 2010).

Comparisons between experimental data (Barnes et al., 1971; Goldsby and Kohlstedt 2001) suggest that the activation energy for ice creep increases at temperatures above −10 ºC. As temperature increases, grain boundaries become wider and contain more liquid; these changes facilitate grain-level sliding, diffusion along grain boundaries, and grain-boundary migration.

However, field data show a large variability of A not accounted for by temperature.

Hydrostatic pressure depresses the melting point of ice. The laboratory experiments on the total effect of pressure (Weertman 1973b; Durham et al., 1997) imply the similar dependency of *A* on pressure as for the temperature shift. Therefore, it can be assumed, as also suggested by Rigsby (1958), that hydrostatic pressure does not affect the creep relation except through its influence on the melting point.

The water content can influence the viscosity of temperate glaciers significantly (Vallon et al., 1976, Duval 1977). Water softens polycrystalline ice by facilitating adjustments between neighbouring grains with different orientations through processes like grain-boundary sliding and melting and refreezing. Within temperate glaciers the water content varies because of differences in porosity, melt rate, and drainage. According to Duval's relation (Duval 1977), formulated through laboratory experiments on samples taken from a temperate glacier, a factor-of-three increase of *A* corresponds to a change of water content from zero to 1.1%.

The commonly used value for glacier (recommended values of *A* at n=3) fall in range of 10^{-24} Pa^{-3} s^{-1} (Cuffey and Paterson, 2010). The results through the calibrations of full-stress models against large-scale flow suggests, at n=3, the value of *A* to be 2.4×10^{-24} Pa^{-3} s^{-1}. The temperate glaciers considered for the calibration represent glaciers from Iceland, Alps, Scandinavia, and Alaska. Moreover, a compiled list of *A* values derived from field analysis and laboratory experiments (Budd and Jacka 1989) at different temperatures can be found in Cuffey and Paterson (2010). The value of $A = 3.24\times10^{-24}$ Pa^{-3} s^{-1} and $A = 2.32\times10^{-24}$ Pa^{-3} s^{-1} is usually adopted for glacier ice thickness modelling based studies (Farinotti et al., 2009; Gantayat et al., 2014) referring to temperate and valley glaciers respectively. However, few studies have reported different values of *A* which vary significantly from the recommended values. For instance, a rate factor of ~10^{-26} Pa^{-3} s^{-1} (Chandler et al., 2008) and 1.6×10^{-24} Pa^{-3} s^{-1} (Zekollari et al., 2013) has been also reported by via simulation of ice flow with a higher-order 3-D model for glaciers in Alps.

6.1.1.2 Glen's Law Exponent (n)

The Glens law exponent n is degree of non-linearity in the stress strain relation given by Glen (1958). Through analyses of the covariation of strain rate and stress in glaciers the values of *n* range from 1.5 to 4.2 (Weertman 1973b, Table 3.2; Weertman 1983, Table 3.1), with a mean of about 3. It shall be noted that in all such studies, stress is not measured but inferred from the balance of forces. Studies carried out in Antarctic ice indicate an *n* value in the range 2 to 3. On the other hand, in grounded glaciers (originating as well as terminating on land) flowing by simple shear deformation on inclined planes (such as valley glaciers), the strain rate varies over depth with a pattern that depends on n. For these glaciers, the data collected by Raymond (1980) best describes a value of n = 3 to 4.

6.1.1.3 Shape Factor (f)

The shape factor parameter is a non-measurable, dimensionless physical parameter that depends upon glacier cross-section profile and valley shape (Cuffey and Paterson 2010). It inherently accounts for the drag due to side walls and glacier bed on the ice flow. Nye (1965) gave a quantitative way to apprehend this parameter where *f* is defined as a function of glacier width (w_{cs}) and ice-thickness (h_{cs}) along the central flowline by the relation

$$f_{cs} = \frac{2}{\pi} \arctan\left(\frac{w_{cs}}{2h_{cs}}\right). \tag{6.5}$$

In this case, *f* assumes a value between 0 (channel of infinite depth) and 1 (channel of infinite width) (Nye, 1965). The value of *f* generally ranges between 0.60 and 0.90 for valley glaciers (Cuffey and Paterson 2010).

6.1.2 Sensitivity Analysis

As a preliminary step to provide insights, such as identifying sensitive and insensitive parameters, before attempting calibration and application, it is considered essential to know the sensitivity of simulations to the ice thickness model parameters. In this regard, to identify the parameters to which the modelled ice thickness is sensitive, the sensitivity has been evaluated using Average Linear Sensitivity (ALS) method (Nearing et al., 1989) which is found to be suitable to assess models having parameters values of different orders of magnitude. This is a local sensitivity approach, and it is estimated by changing the value of the parameter under examination, while all other parameters are kept constant. The ALS index is calculated using the relation,

$$ALS = \frac{\frac{(h_2 - h_1)}{h}}{\frac{(I_2 - I_1)}{\bar{I}}}. \tag{6.6}$$

Where, I_1 and I_2 are the minimum and maximum values of the parameter under consideration, and h_1 and h_2 are the values of model output (here ice thickness *h*) for the corresponding input values. $\bar{I}$ is the mean of I_1 and I_2, and *h* is the mean of h_1 and h_2. The sign of ALS represents the nature of correlation between the model output and the individual parameter. Following Nearing et al., (1989), the sensitivity to model parameters are categorized as high moderate or less sensitive where the output (i.e. ice thickness) is highly sensitive to a parameter if ALS≥1, moderately sensitive when $0.5 \leq$ ALS < 1 and less sensitive when ALS < 0.5.

6.1.3 Model Calibration

The ice thickness model parameters (*A, f, n*) are calibrated using Shuffle Complex Evolution (SCE) method (Duan et al., 1992) to find the glacier specific optimal set of model parameters where evolution of model parameters is achieved through multiple complex shuffling based on the simplex search method (Nelder and Mead, 1965).

6.2 Results and Discussion

In this section, the application and performance evaluation of proposed ice thickness model application named GATHI **(G**l**A**cier ice **THI**ckness distribution using remote sensing) is discussed. The word '*gathi*' in Hindi means '*speed*' which also reflects the velocity based approach to the proposed ice thickness model. Following the sensitivity analysis of the modelled ice thickness estimates towards model inputs, the performance of the ice thickness estimation model was subsequently assessed through application in four study glaciers. To explore the applicability of the ice thickness model to glaciers without any field ice thickness measurements available, two different scenarios were considered. In scenario 1, the transferability of the model parameter from one glacier (with available field observations) to other glaciers sharing similar characteristics (with no available field measurements) was explored. In scenario 2, considering that the geometry-based parameter *f* cannot be replicated from one glacier to other, potential for field-data-independent calibration (Ramsankaran et al., 2018) was explored. Furthermore, to explore the effect of calibration data on the model, the model's sensitivity was evaluated towards observation's spatial and quantity-related characteristics. This evaluation was performed through set of 10 experiments. Lastly, a comparison with some of the existing models applied at global scale is also discussed.

6.2.1 Ice Thickness Sensitivity to Input Parameters

Figure 6.2 shows the sensitivity of the ice thickness towards the three model parameters. The range of the model parameters used for this analysis have been taken from reported values where *n* is varied from 3 to 4, *f* from 0.6 to 0.9, *A* from $1.6*10^{-26}$ Pa^{-3} s^{-1} to $3.2*10^{-24}$ Pa^{-3} s^{-1}. From Figure 6.2 it is observed that the model is extremely sensitive to the Glen's law exponent (*n*), moderately sensitive to shape factor (*f*) and less sensitive to flow rate factor (*A*).

Furthermore, the sensitivity at different range of each model parameter (at 10%, 20% variation from base value) is investigated. It was found that the modelled ice thickness is more sensitive to lower values of shape factor (at -10% or -20% from base value) than the higher values (at +10% or +20% from base value). Which implies that for lower values of *f* (which corresponds to narrow and deeper regions of the glacier) the modelled ice thickness can be expected to show large deviations. Similar variations in sensitivity of ice thickness towards other parameters (*n* and *A*) were not observed. Through sensitivity analysis using ALS index, the modelled ice thickness is found to be sensitive towards the model parameters (based on material properties: *A* and *n*; based on geometry of glacier: *f*) at different level of sensitivity and thus required to be calibrated.

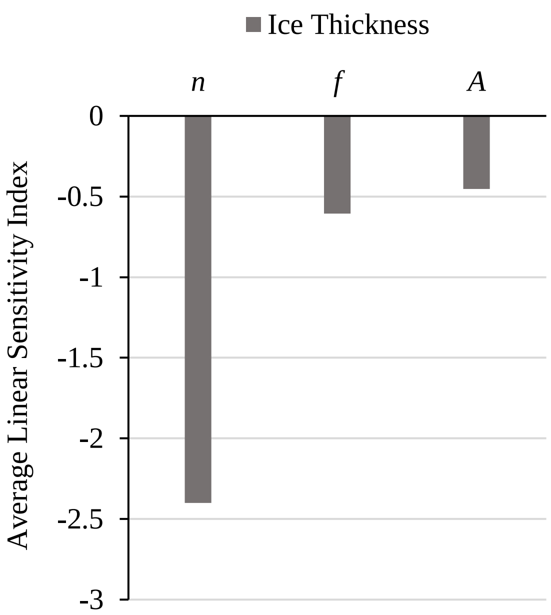

Figure 6.2 Average linear sensitivity plot of the ice thickness model input parameters**.**

6.2.2 Ice Thickness Sensitivity to Remotely Sensed Glacier Surface Velocity

The sensitivity of the estimated ice thickness due to the estimated glacier surface velocity was assessed by varying the input velocity by +10%, +20%, -10%, and -20% respectively. Unlike the model parameters which are constant across the glacier, the input glacier velocity varies spatially. Thus, the change in estimated ice thickness due to change in input velocity was observed to vary across the glacier. The percent change in ice thickness due to +10% change in the input velocity showed a mean of 8.2%. Similarly, percentage change in estimated ice thickness due to change in input velocity by +20%, -10% and -20% showed a mean of 10%, 7.4% and 9.1% respectively. In all the above, the range of the percentage change in estimated ice thickness remained constant with maximum of 140%. Minimum values were observed near the glacier central flowline whereas higher values were observed near the glacier boundary which shows that the estimated ice thickness is more sensitive at these locations.

6.2.3 Spatial Distribution of Ice Thickness Estimates

The model parameters are calibrated using all the available ice thickness data for a glacier irrespective of the spatial distribution. For each of the study glaciers, the calibrated model parameter is found to be different from the commonly used values. Specifically, glacier specific calibrated parameters are $n = 3.1$, $A = 3.28*10^{-24}$ Pa^{-3} s^{-1}, $f = 0.64$ (South Glacier); $n = 3.6$, $A = 1.5*10^{-24}$ Pa^{-3} s^{-1}, $f = 0.65$ (Chhota Shigri Glacier); $n = 3.4$, $A = 5.6*10^{-24}$ Pa^{-3} s^{-1}, $f = 0.78$ (Patsio Glacier); $n = 3.2$, $A = 5.1*10^{-24}$ Pa^{-3} s^{-1}, $f = 0.65$ (Tasman Glacier). Through the calibrated model the achieved accuracy for study glaciers is 0m (South Glacier), ~10m (Chhota Shigri Glacier and Patsio Glacier) and ~120m (Tasman Glacier). Where the accuracy is represented by the mean error.

6.2.3.1 South Glacier

Spatially distributed ice-thickness estimates of the South Glacier obtained from the proposed model simulations using calibrated model is shown in Figure 6.3a. The horizontal and vertical velocity used as input are given in Chapter 5 (for period 2014-15) and Appendix-A5 respectively. To compare with the measured ice thickness observed in 2011, the DEM has been adjusted considering a surface elevation change of -0.5 m/yr reported by Wheler (2009) for South Glacier. It can be observed that the ice-thickness is not uniform across the glacier, which varies from 0 to 220 m. Zero ice-thickness is observed at boundary pixels and maximum ice-thickness of 220 m is observed at central flow line that lies near to the reported Equilibrium Line Altitude (ELA) of 1050 m (De Pauli and Flowers, 2009). This is a significant observation to mention, which indicates the correctness of the model results in view of the fact that the maximum ice thickness generally occurs near to ELA (Hooke 2005). It is also observed that ice-thickness along the central flowline of the glacier is having local maxima. This is realistic because along the central flow line the rate of glacier flow is faster, leading to higher mass contributions and thus, resulting in higher ice-thickness. Likewise, it is found that the derived ice-thickness pattern across the glacier agrees well with the empirical relation between the width and ice-thickness of a glacier which says that wider the glacier, more the depth (Frey et al., 2010).

Figure 6.3b shows the proposed model estimates of ice thickness at the central flowline (CFL) and at different cross sections (CS1-CS16) of the glacier. At these profiles, the available observed ice thickness data available at glacier ice thickness database is also shown. The RMSEs obtained for each cross section are CS1: 27m, CS2: 56m, CS3: 63m, CS4: 29, CS5: 31m, CS6: 38m, CS7: 24m, CS8: 42m, CS9: 24m, CS10: 21m, CS11: 28m, CS12: 26m, CS11: 27m, CS14: 31m, CS15: 37m, CS16: 12m. The obtained RMSE along the CFL is 40m. The estimated ice thickness showed good agreement in the middle region of the glacier (mean RMSE ~25m). However, at lower elevations near the snout, the estimated ice-thickness is found to be in the order of 50-70 m. The obtained RMSE at upper parts of the glacier (CS1 to CS7) are found to be similar to the reported estimates by HF model (Model1: Farinotti et al., 2019) which is a similar ice-flux based method where flux is calculated using mass balance gradient instead of glacier surface velocity. However, the RMSEs at lower reaches are found to be slightly higher than the estimates reported by HF model. The probable reason behind this can be the suggested surge conditions (De Paoli and Flowers, 2009) at the lower region of the glacier which affects the glacier velocity estimates.

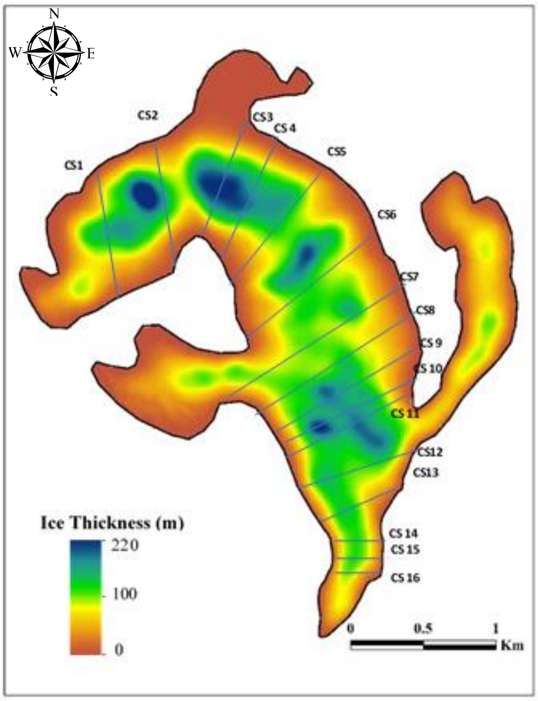
N
W
E
S
CS1
CS2
CS3
CS 4
CS5
CS6
CS7
CS8
CS 9
CS 10
CS 11
CS12
CS13
CS 14
CS 15
CS 16
Ice Thickness (m)
220
100
0
0
0.5
1
Km

(a)

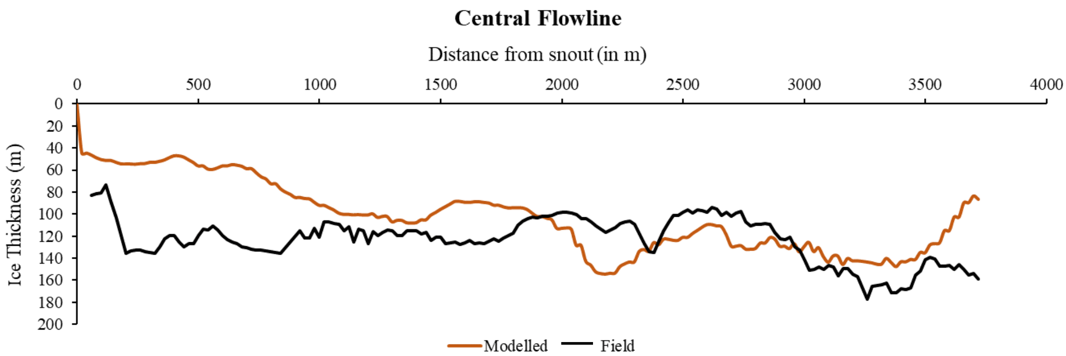
Central Flowline
Distance from snout (in m)
0
500
1000
1500
2000
2500
3000
3500
4000
Ice Thickness (m)
0
20
40
60
80
100
120
140
160
180
200
Modelled
Field

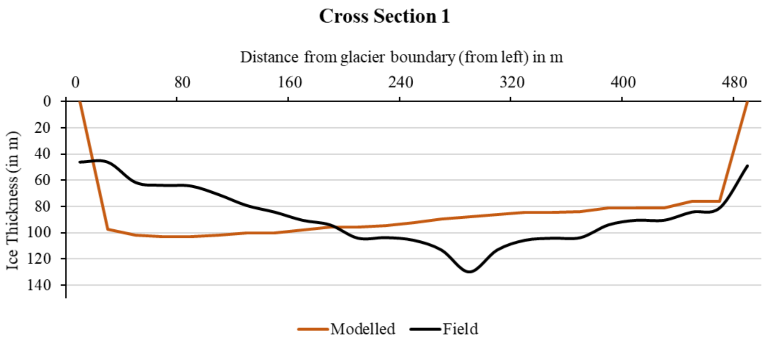
Cross Section 1
Distance from glacier boundary (from left) in m
0
80
160
240
320
400
480
0
20
40
60
80
100
120
140
Ice Thickness (in m)
Modelled
Field

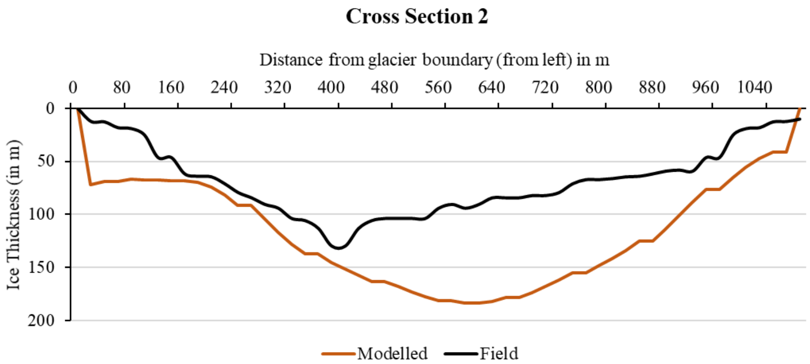
Cross Section 2
Distance from glacier boundary (from left) in m
0
80
160
240
320
400
480
560
640
720
800
880
960
1040
0
50
100
150
200
Ice Thickness (in m)
Modelled
Field

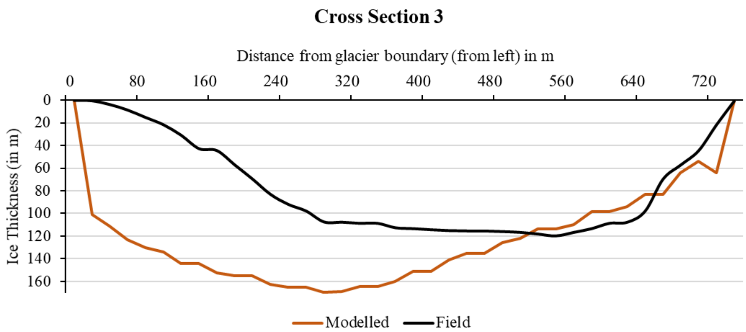
Cross Section 3
Distance from glacier boundary (from left) in m
0
80
160
240
320
400
480
560
640
720
0
20
40
60
80
100
120
140
160
Ice Thickness (in m)
Modelled
Field

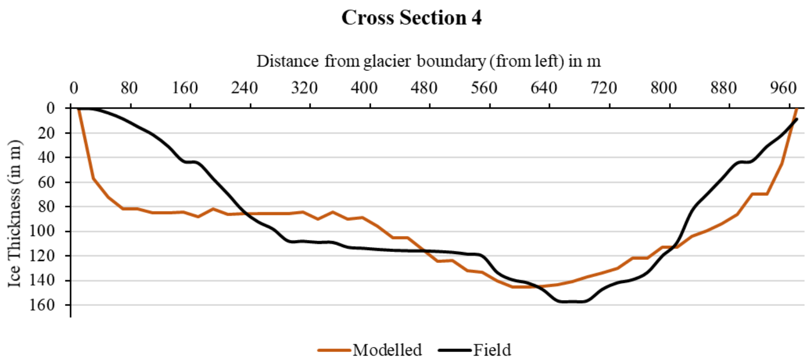
Cross Section 4
Distance from glacier boundary (from left) in m
0
80
160
240
320
400
480
560
640
720
800
880
960
0
20
40
60
80
100
120
140
160
Ice Thickness (in m)
Modelled
Field

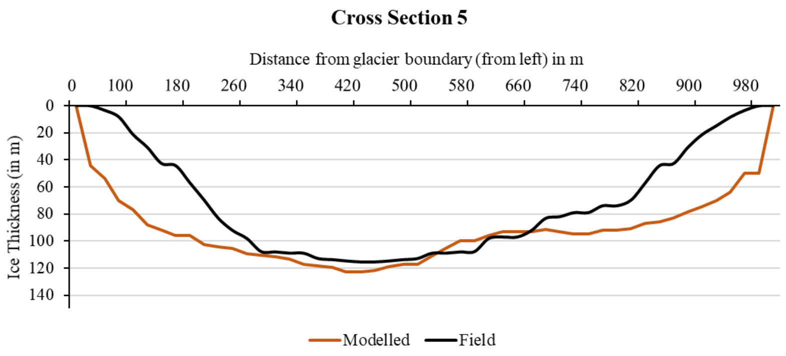
Cross Section 5
Distance from glacier boundary (from left) in m
0 100 180 260 340 420 500 580 660 740 820 900 980
Ice Thickness (in m)
0 20 40 60 80 100 120 140
Modelled
Field

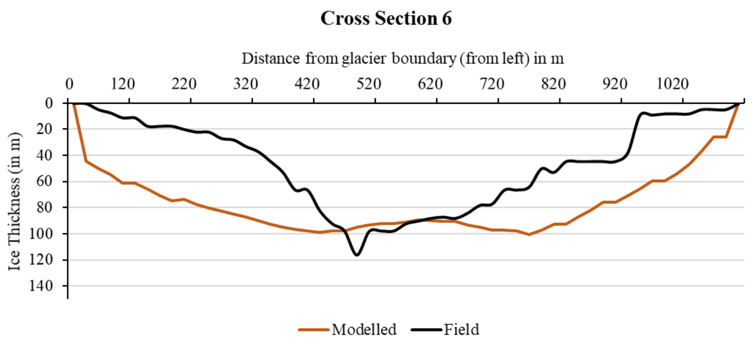
Cross Section 6
Distance from glacier boundary (from left) in m
0 120 220 320 420 520 620 720 820 920 1020
Ice Thickness (in m)
0 20 40 60 80 100 120 140
Modelled
Field

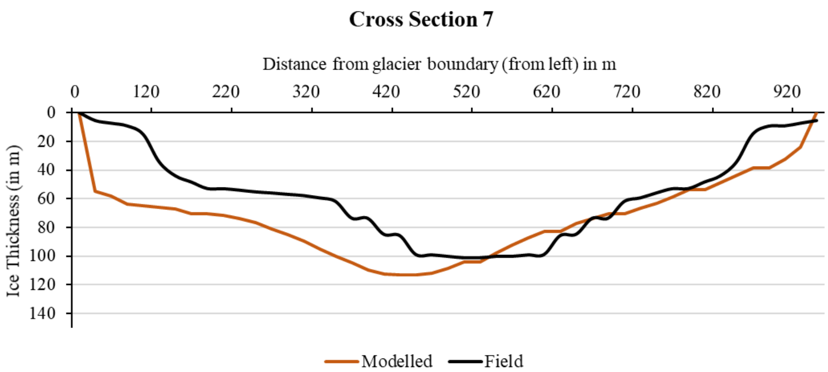
Cross Section 7
Distance from glacier boundary (from left) in m
0 120 220 320 420 520 620 720 820 920
Ice Thickness (in m)
0 20 40 60 80 100 120 140
Modelled
Field

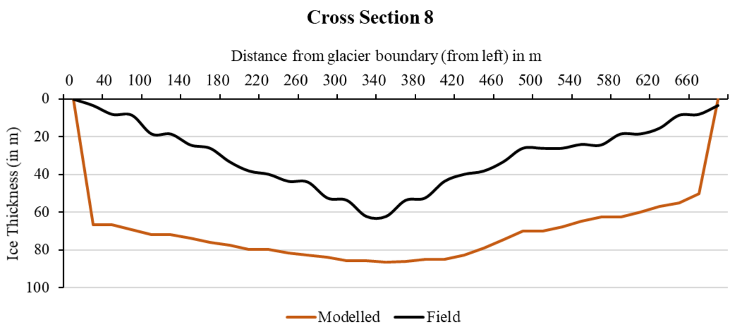
Cross Section 8
Distance from glacier boundary (from left) in m
0 40 100 140 180 220 260 300 340 380 420 460 500 540 580 620 660
Ice Thickness (in m)
0 20 40 60 80 100
Modelled
Field

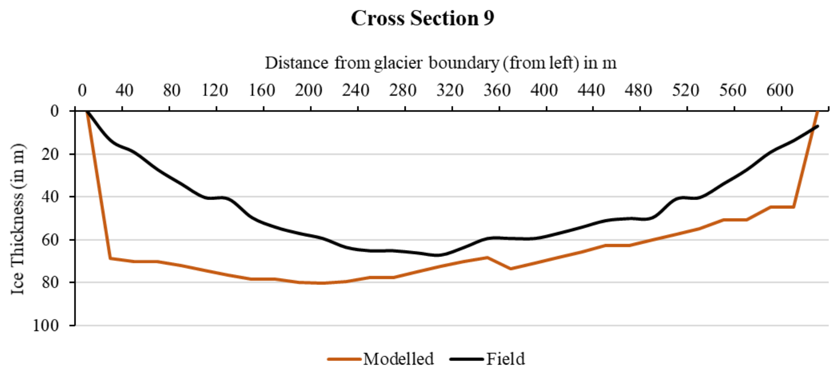
Cross Section 9
Distance from glacier boundary (from left) in m
0 40 80 120 160 200 240 280 320 360 400 440 480 520 560 600
Ice Thickness (in m)
0 20 40 60 80 100
Modelled
Field

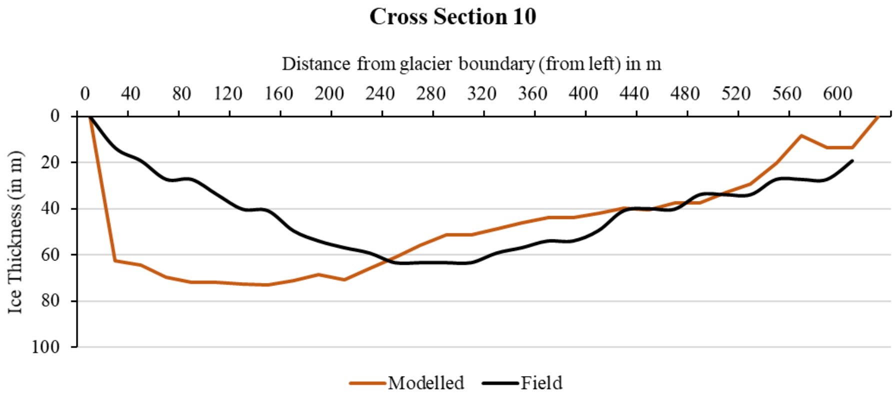
Cross Section 10
Distance from glacier boundary (from left) in m
0 40 80 120 160 200 240 280 320 360 400 440 480 520 560 600
Ice Thickness (in m)
0 20 40 60 80 100
Modelled
Field

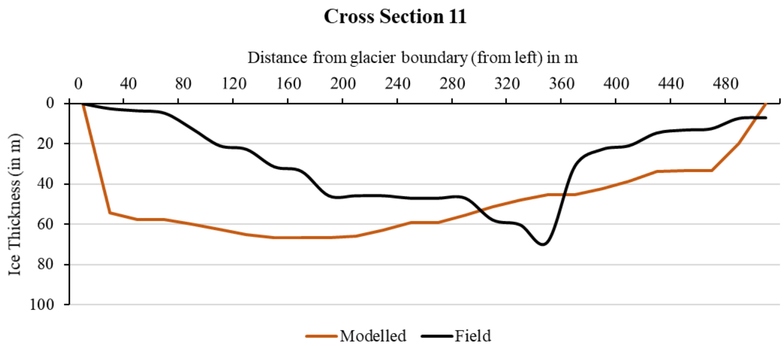
Cross Section 11
Distance from glacier boundary (from left) in m
0 40 80 120 160 200 240 280 320 360 400 440 480
Ice Thickness (in m)
0 20 40 60 80 100
Modelled
Field

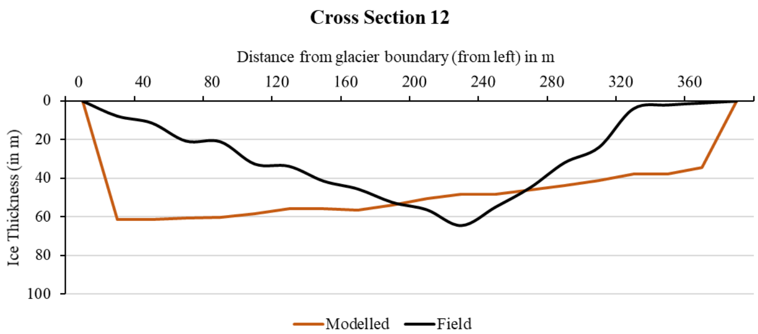
Cross Section 12
Distance from glacier boundary (from left) in m
0 40 80 120 160 200 240 280 320 360
Ice Thickness (in m)
0 20 40 60 80 100
Modelled
Field

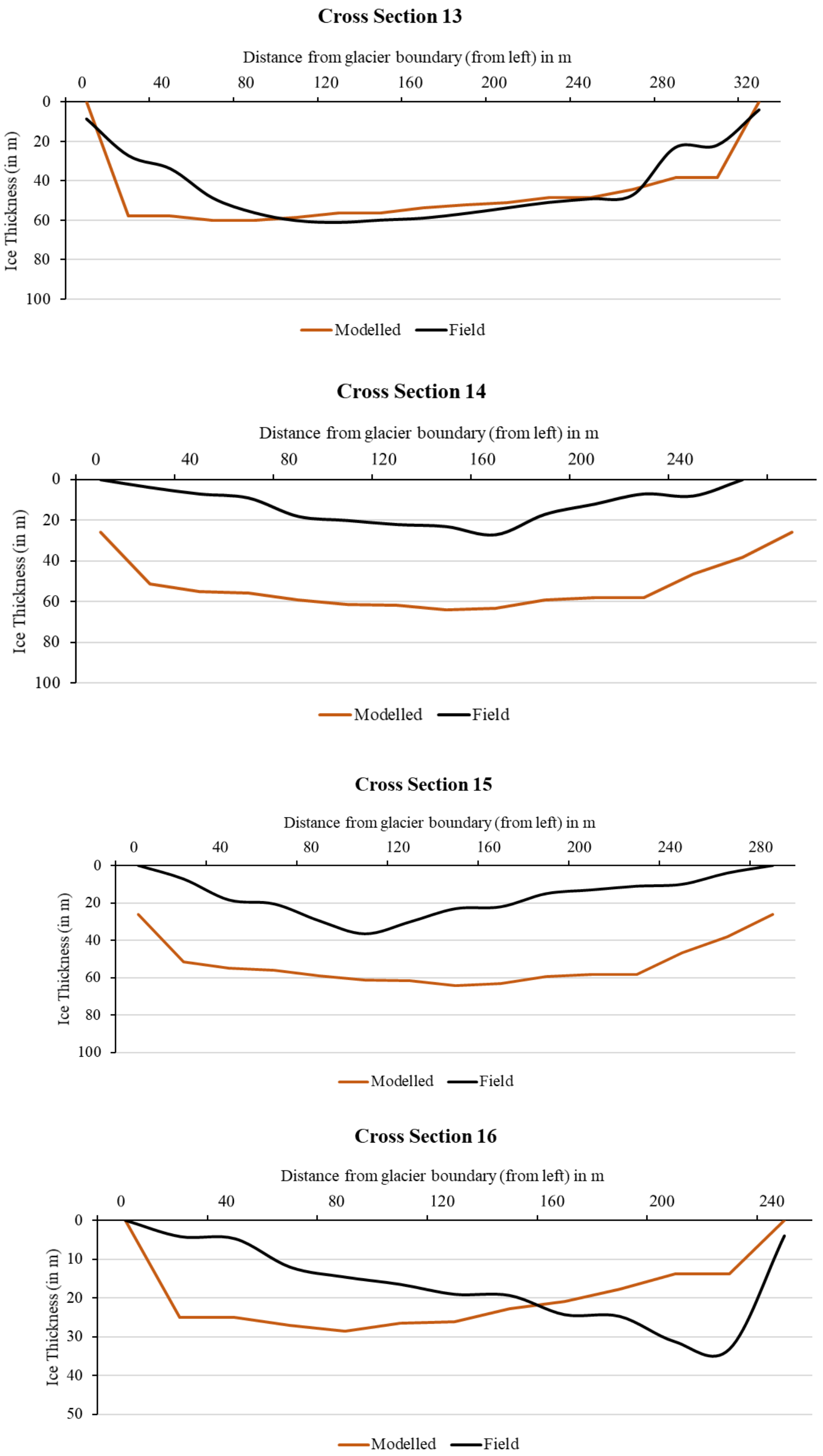

(b)

Figure 6.3 a) Spatial distribution of estimated glacier ice thickness of South Glacier. b) Estimated glacier ice thickness along the central flowline and various cross section profiles of the glacier.

6.2.3.2 Chhota Shigri Glacier

The Spatially distributed ice-thickness estimates of the Chhota Shigri Glacier obtained from the proposed model simulations using calibrated parameterization is shown in Figure 6.4a. The horizontal and vertical velocity used as input are given in Chapter 5 and Appendix-A5 respectively. From Figure 6.4a it can be observed that the ice-thickness varies from 0 to 330 m and exhibits maximum ice-thickness at central flow line that lies near to the reported Equilibrium Line Altitude (ELA) of 4950 m a.s.l. (Azam et al., 2012). This location of maximum ice thickness corresponds closely to other existing studies on this glacier (Ramsankaran et al., 2018; Farinotti et al., 2019).

Figure 6.4b shows the proposed model estimates of ice thickness at the central flowline (CFL) and at different cross sections (CS1-CS5) of the glacier. The RMSEs obtained for each cross section are CS1: 36m, CS2: 49m, CS3: 46m, CS4: 48, CS5: 29m. At these profiles, the available observed ice thickness data reported by Azam et al., (2012) is also shown. The estimated ice thickness agrees closely with the observed ice thickness along CS5 however it is overestimated for the remaining profiles by average deviation of 42m. This deviation however is slightly less when compared with the HF method (Model1: Farinotti et al., 2019) which underestimates the ice thickness at CS1 and CS2 by ~49m. This difference in the estimates could be due to the fact that the present model estimates consider the surface elevation changes between time period of estimates and the time period of the field measurement.

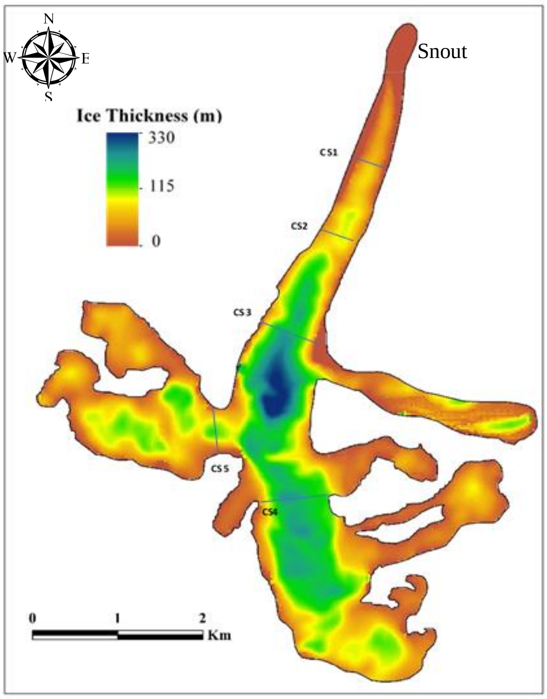

(a)

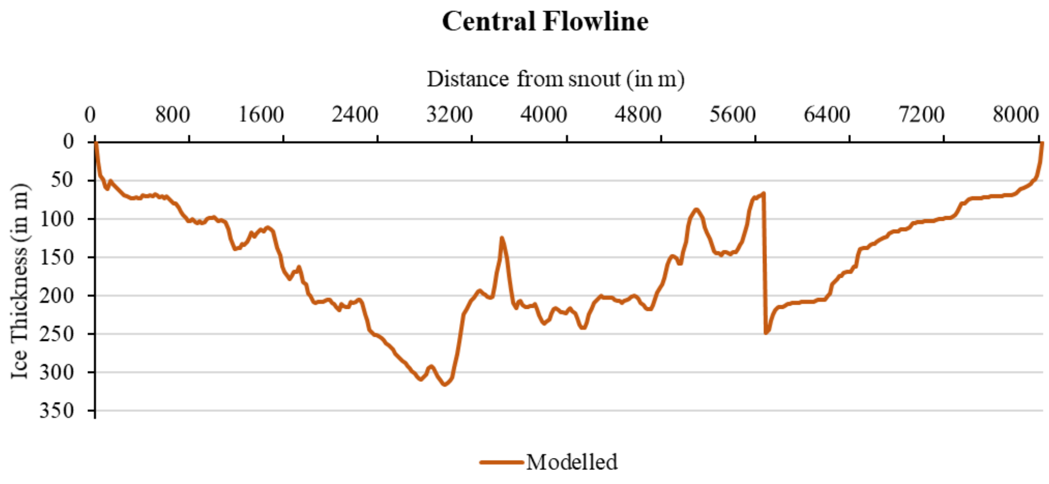
Central Flowline
Distance from snout (in m)
0
800
1600
2400
3200
4000
4800
5600
6400
7200
8000
Ice Thickness (in m)
0
50
100
150
200
250
300
350
Modelled

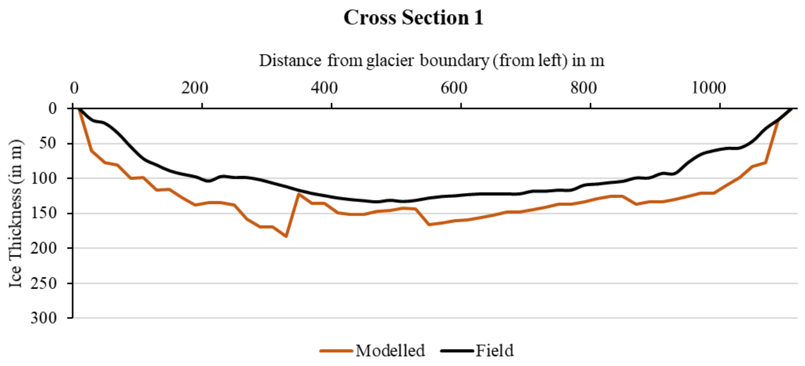
Cross Section 1
Distance from glacier boundary (from left) in m
0
200
400
600
800
1000
Ice Thickness (in m)
0
50
100
150
200
250
300
Modelled
Field

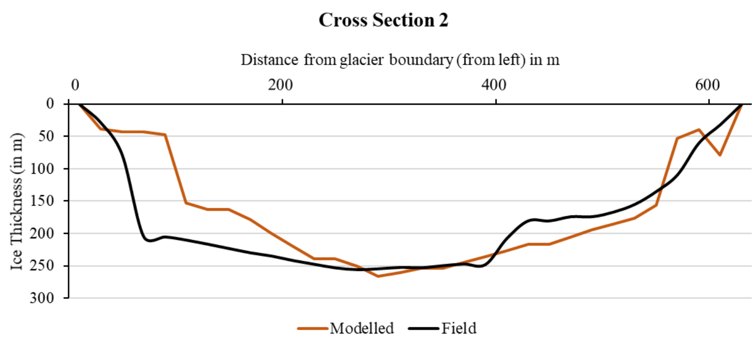
Cross Section 2
Distance from glacier boundary (from left) in m
0
200
400
600
Ice Thickness (in m)
0
50
100
150
200
250
300
Modelled
Field

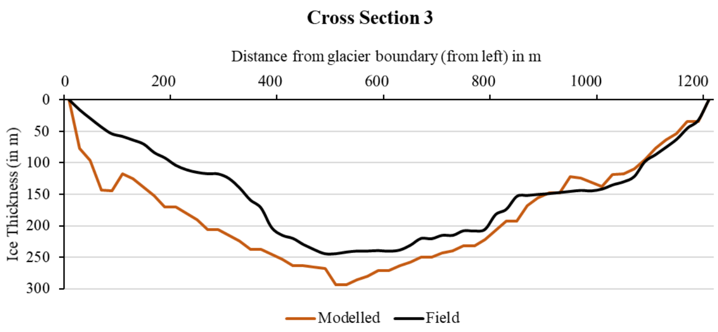
Cross Section 3
Distance from glacier boundary (from left) in m
0
200
400
600
800
1000
1200
Ice Thickness (in m)
0
50
100
150
200
250
300
Modelled
Field

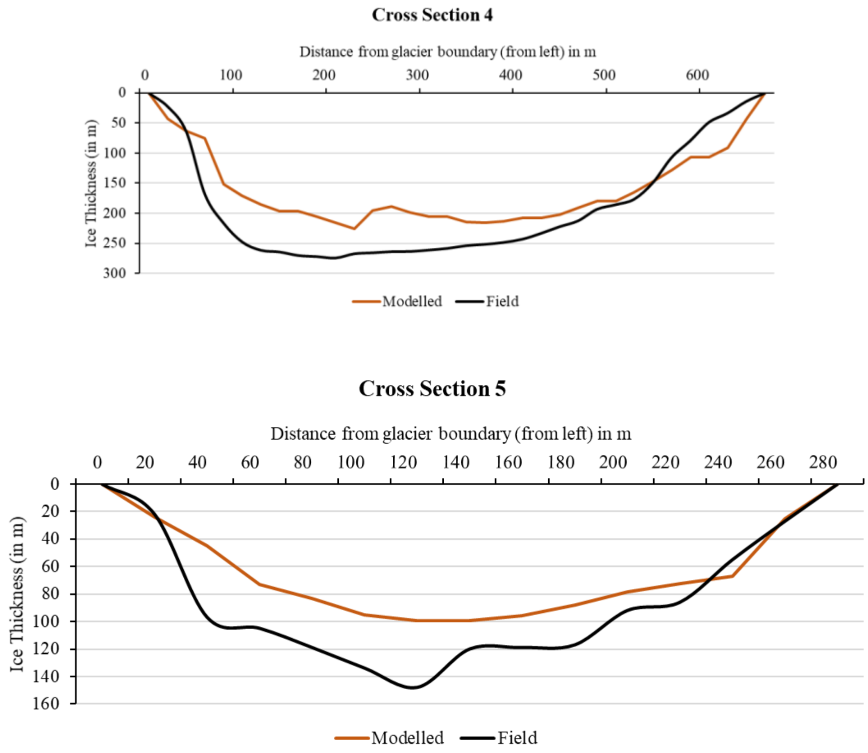

(b)

Figure 6.4 a) Spatial distribution of estimated glacier ice thickness of Chhota Shigri Glacier. b) Estimated glacier ice thickness along the central flowline and various cross section profiles of the glacier.

6.2.3.3 Patsio Glacier

Spatially distributed ice-thickness estimates of the Patsio Glacier obtained from the proposed model using calibrated parameterization is shown in Figure 6.5a. The horizontal and vertical velocity used as input are given in Appendix-A6 and Appendix-A5 respectively. Here the velocity could not be validated since there is no field data available for surface velocity of Patsio Glacier. From Figure 6.5a, it can be observed that the ice-thickness is not uniform across the glacier, which varies from 0 to 165 m. The maximum ice-thickness of 220 m is observed at central flow line that lies near to the middle of the glacier with widest cross section.

Figure 6.5b shows the proposed model estimates of ice thickness at the central flowline (CFL) and at different cross sections (CS1-CS3) of the glacier. At these profiles, the measured GPR based ice thickness data collected during the study is also shown. The RMSEs obtained for each cross section are CS1: 23m, CS2: 20m, CS3: 22m. The obtained

RMSE along the CFL is 31m. At lower elevations near the snout, the estimated ice-thickness is found to be in the order of 40 m as reported by existing studies and the field measurement performed in this study (Kumar et al., 2020). Likewise, the reported estimates by HF model (Model1: Farinotti et al., 2019) show similar RMSEs (of 22m) for these cross sections.

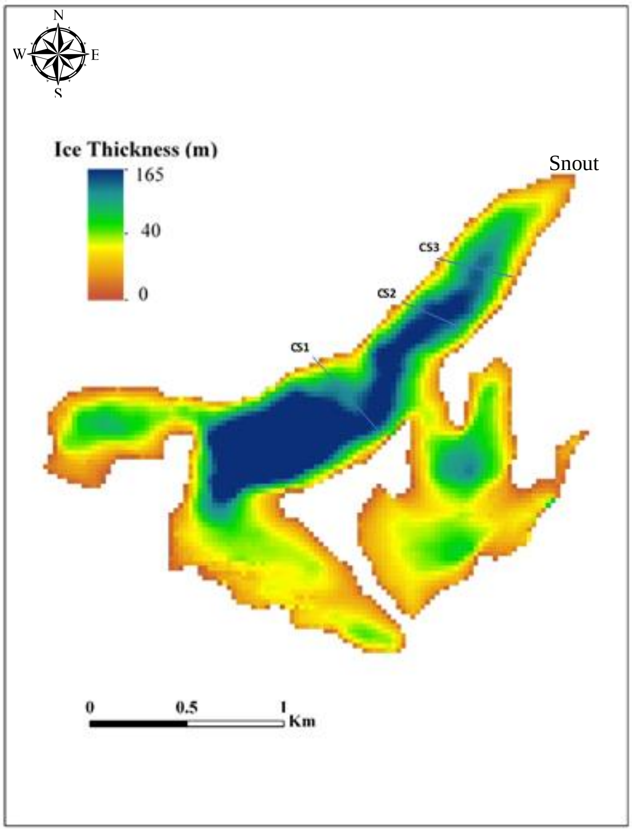

(a)

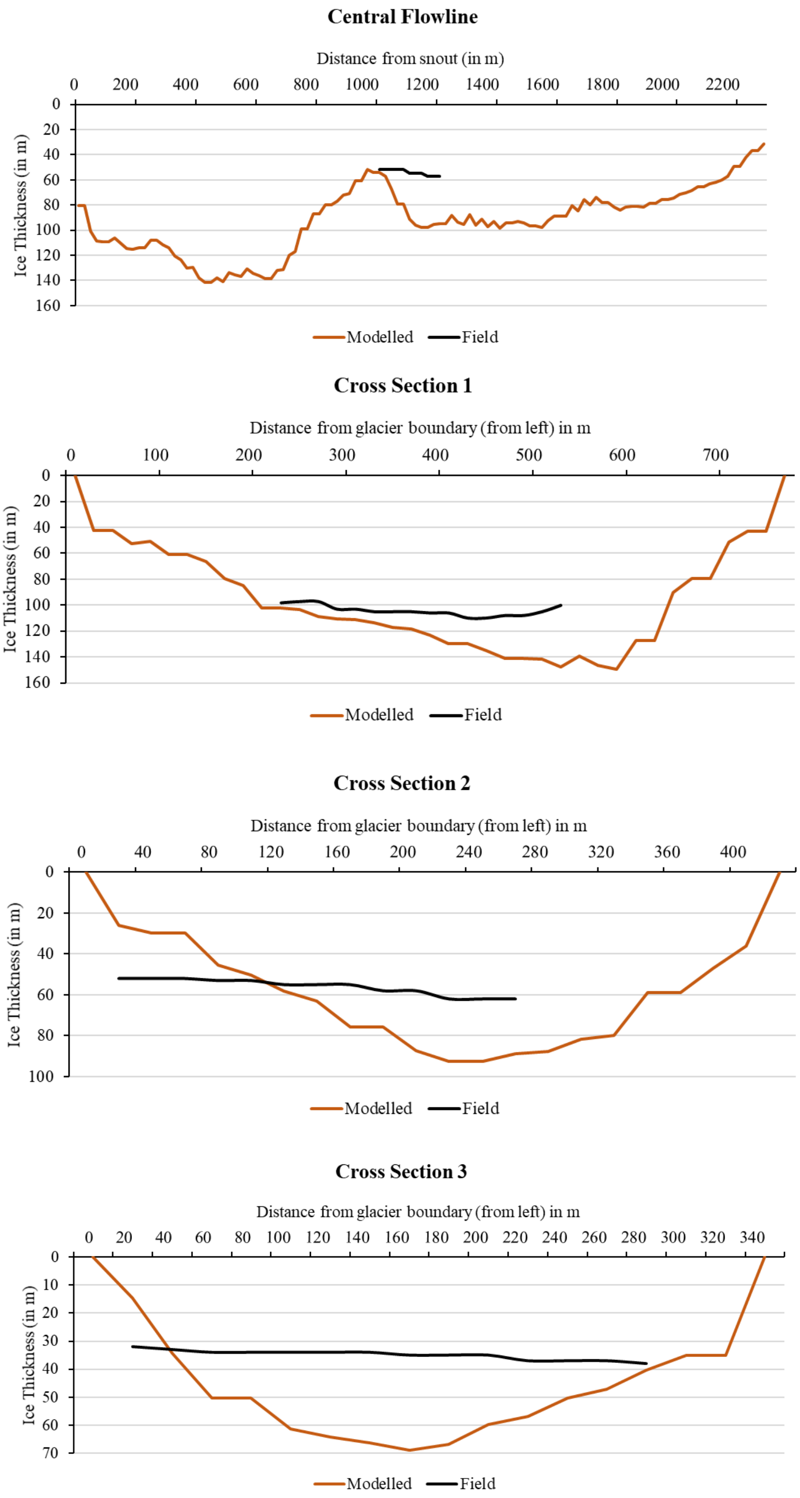

(b)

Figure 6.5 a) Spatial distribution of estimated glacier ice thickness of Patsio Glacier. b) Estimated glacier ice thickness along the central flowline and various cross section profiles of the glacier.

6.2.3.4 Tasman Glacier

Spatially distributed ice-thickness estimates of the Tasman Glacier obtained from the proposed model simulations using calibrated parameterization is shown in Figure 6.6. The horizontal and vertical velocity used as input are given in Chapter 5 (for period 2005-06) and Appendix-A5 respectively. It can be observed that the ice-thickness is not uniform across the glacier, which varies from 0 to 790 m. Maximum ice-thickness of is observed at central flow line that lies near to the reported Equilibrium Line Altitude (ELA) (Hart 2014) which is closer to CS2 (Figure 6.6a).

Figure 6.6b shows the proposed model estimates of ice thickness at the central flowline (CFL) and at two cross sections (CS1 and CS2) of the glacier. RMSEs of 242m (each) is observed at these two profiles when compared with available ice thickness data. Overestimation is observed at CS2 while at CS1 an underestimation was observed.

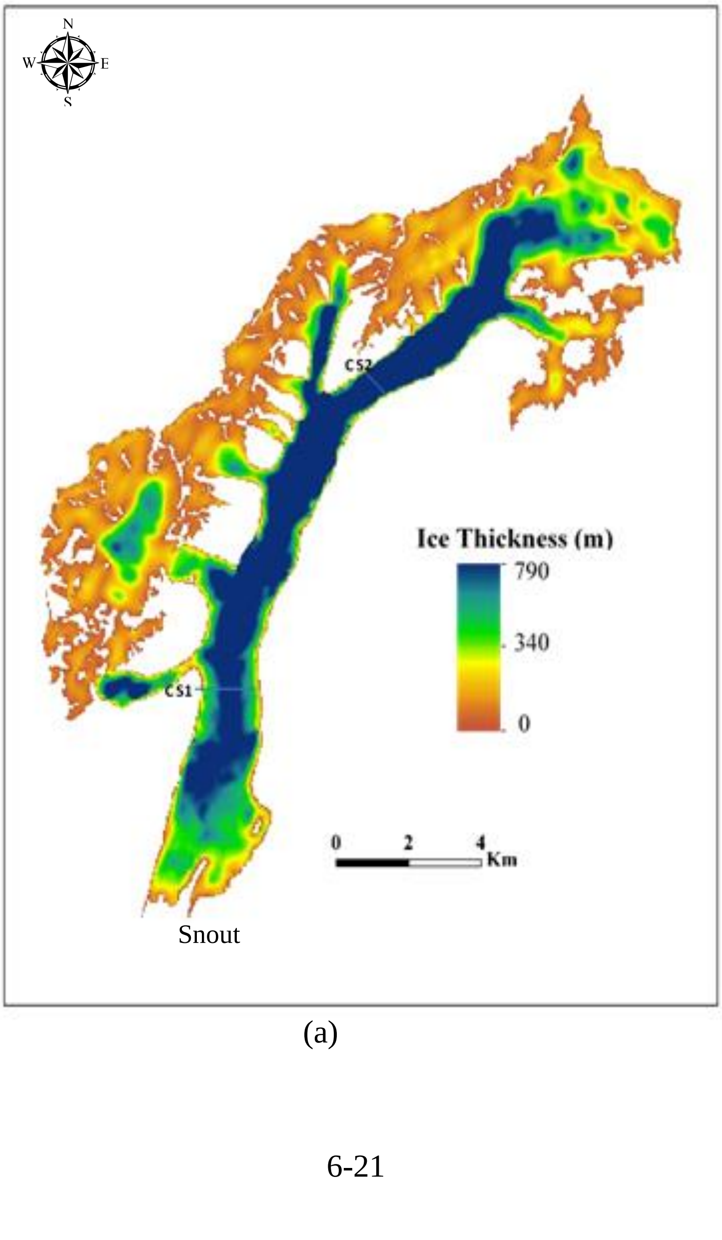

(a)

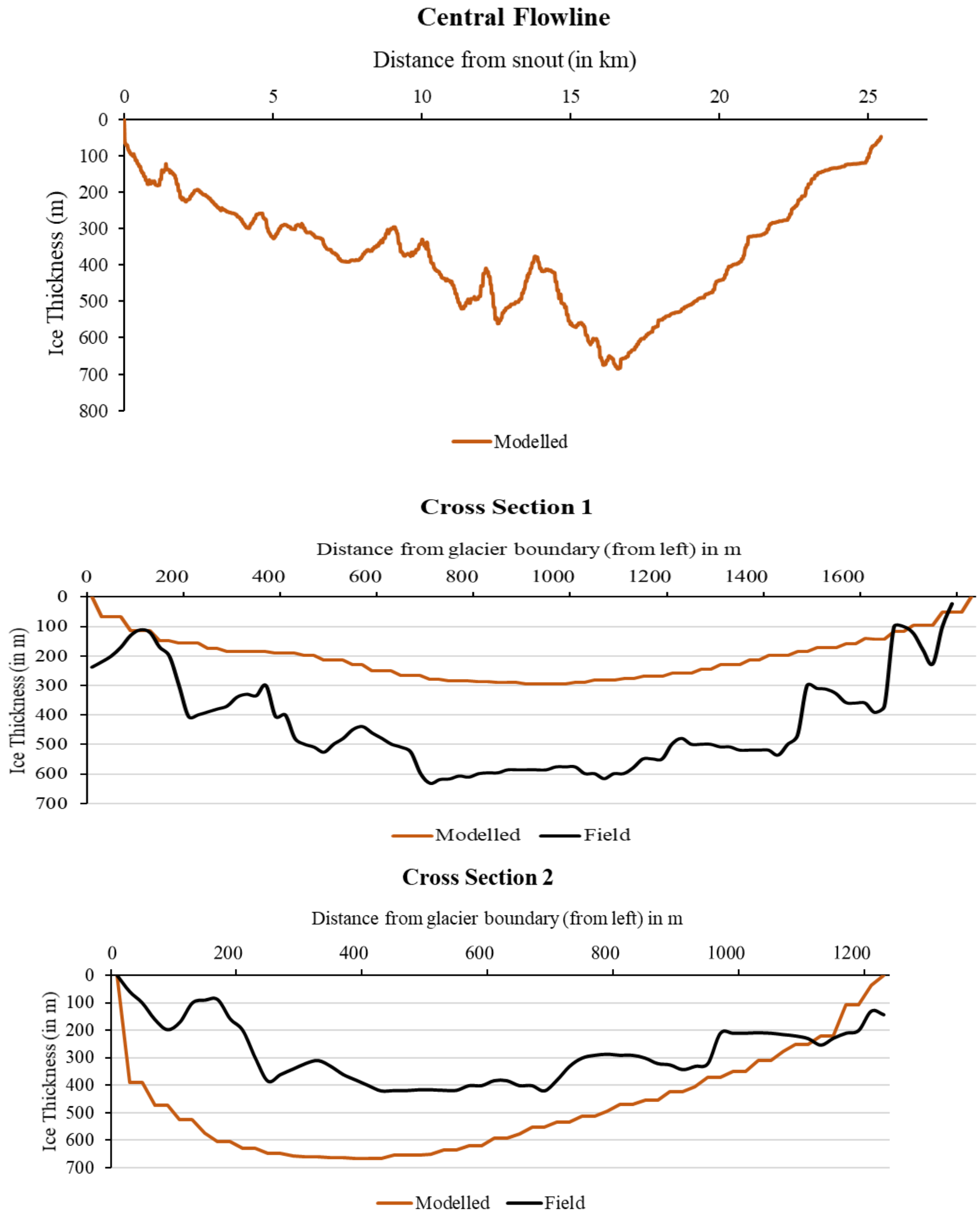

(b)

Figure 6.6 a) Spatial distribution of estimated glacier ice thickness of Tasman Glacier. b) Estimated glacier ice thickness along the central flowline and various cross section profiles of the glacier.

Firstly, cross glacier profiles for the Tasman Glacier are complicated by multiple tributaries delivering mass into the Tasman Glacier catchment (for example, Rudolf and Darwin Glaciers). Secondly, an important control on maximum ice thickness in the model is the surface slope. The relation between estimated ice thickness and the input surface slope indicates that for small surface slopes ice thickness (*h*) is increased in order to maintain the same ice volume. As the slope approaches zero *h* tends to infinity. For the Tasman Glacier, surface slopes near the terminus are low which induces this overestimation. Moreover, these estimates are found to be better than that of HF model (Model 1: Farinotti et al., 2019) which is observed to have higher overestimation for the glacier. This indicates that the model parametrization through the glacier surface velocity (present model) outperforms the parameterization through mass balance gradient (Model 1: Farinotti et al., 2019). The simple assumption that the ice flux is distributed linearly with distance from the margin in each elevation band may be inaccurate. That is, the linear assumption doesn't provide enough ice flux in the glacier center and so underestimates ice thickness there. One more reason for the deviation from model1 (Farinotti et al., 2019) is that the DEM used in this model for this glacier represents the surface topography for year from 2000 which is different from the time period of the observed ice thickness (refer to chapter 4). Thus, the surface topography obtained from the DEM was adjusted to incorporate the average surface elevation change (also equivalent to average mass loss in m) (Watson, 1995) between the modelled and observed period.

A similar positive bias in the estimated ice thickness is observed in all the study glaciers. The positive bias in input estimated glacier velocities seems less likely to be the reason for positive bias is found in the estimated glacier thickness, since the bias in estimated velocity is positive throughout while the bias in estimated ice thickness shows both trends (positive as well as negative). The incompetence in correctly estimating ice fluxes from the apparent mass balance may be due to the steady state assumption (Rabatel et al., 2018). This implies that if the glacier is not in steady state, the ice flux calculations will be affected so will the ice thickness estimates.

6.2.4 Model Application

In this section, the capability of the ice thickness model application is explored for glaciers without any field ice thickness measurements available. For such cases, the transferability of the model parameter from one glacier (with available field observations) to other glacier sharing similar characteristics (with no available field measurements) is explored. Similar experiments with the shape factor parameter could not be synthesized because of its dependency on the glacier geometry (width to thickness ratio) which is rather glacier specific and requires ice thickness measurements. Furthermore, considering that the geometry-based parameter *f* cannot be replicated from one glacier to other, potential for its field-data-independent calibration is explored.

6.2.4.1 Scenario 1

In this scenario, the transferability of calibrated model parameters among similar glaciers is explored. For this analysis, all the four study glaciers are considered which can be categorized as temperate type glaciers thus sharing similar temperature conditions. Due to similar temperature conditions, it can be fairly assumed that the material properties of ice (which is predominantly dependent on temperature) is same for all glaciers. Following this hypothesis, the Glen's flow law parameters *A* and *n* can be expected to be constant among the temperate type glaciers. In this sub-scenario, the aim is to investigate whether the calibrated model parameters (A and n) can be used for other glaciers with similar material properties (here temperate type glaciers). Keeping shape factor (*f*) as fixed (at the standard value of 0.8), the other model parameters are calibrated using the SCE calibration approach. It was found that the calibrated Glen's flow law parameters (A $=3.8*10^{-24}$ and n =3) are same for all the four study glaciers. These observations suggest that for the ice thickness model application, the calibrated parameters A ($=3.8*10^{-24}$) and n (=3) can be assumed to be constant for a temperate type glacier.

6.2.4.2 Scenario 2

Unlike the model parameters *A* and *n* which are dependent on material properties of glacier ice, the shape factor parameter depends on the glacier geometry (ratio of glacier width and thickness at a particular cross-section) and is glacier specific. In case of application to data scarce glaciers, this parameter is estimated using a self-calibration approach (Ramsankaran *et al.*, 2018) which does not require field measurements. Firstly, the spatially distributed average ice-thickness (h_{avg}) of the glacier has been calculated from model run by varying shape factor values ranging between 0.6 and 0.9 at an interval of 0.01 (and using calibrated values for *A* and *n* from scenario 1). Following this, shape factor at different cross-sections (f_{cs}) using Eq 6.5 has been calculated using the maximum h_{avg} at each cross-section i.e. h_{avg_cs} and width of corresponding cross-section, w_{cs}. Based on the above obtained shape factor at each cross-section, glacier-wide average shape factor f_{avg} (considered as optimal shape factor) has been calculated by simple averaging.

Table 6.1 summarizes the estimated (f_{cs_avg}) and observed ($f_{cs\_avg\_observed}$) glacier-wide average shape factor for each study glacier.

Table 6.1 Summary of estimated and observed glacier wide average shape factor for study glaciers. The estimated average ice thickness (h_{avg_cs}) and shape factor at each cross-section have been used to calculate the estimate of average shape factor (f_{cs_avg}).

	Profile No.	w_{cs}	h_{avg_cs}	f_{cs}	f_{cs_avg}	$f_{cs\_avg\_observed}$
South Glacier	1	338	146	0.55	0.82	0.87
	2	730	106	0.82		
	3	1085	101	0.88		
	4	1137	91	0.90		
	5	1022	93	0.89		
	6	727	96	0.84		
	7	810	89	0.86		
Chhota Shigri Glacier	1	404	165	0.56	0.65	0.68
	2	831	288	0.61		
	3	1144	244	0.74		
	4	1059	242	0.73		
	5	676	242	0.60		
Patsio Glacier	1	360	55	0.81	0.77	0.76
	2	370	70	0.77		
	3	560	120	0.74		
Tasman Glacier	1	1248	508	0.57	0.66	0.61
	2	1770	363	0.75		

Figure 6.7 shows the cross-section used for calculating cross-sectional shape factor. The cross-sections to estimate the shape factor were taken every 100m for South Glacier. For remaining glaciers, only those cross-sections were used which had observed ice thickness information. For all the study glaciers the mean estimated f_{cs_avg} is found to be close with

the mean observed shape factor $f_{cs\_avg\_observed}$. The error in estimated ice thickness was reduced by 5-17% (of mean observed ice thickness) when calibrated shape factor was used instead of the uncalibrated shape factor. Here the other two model parameters (A and n) were kept constant.

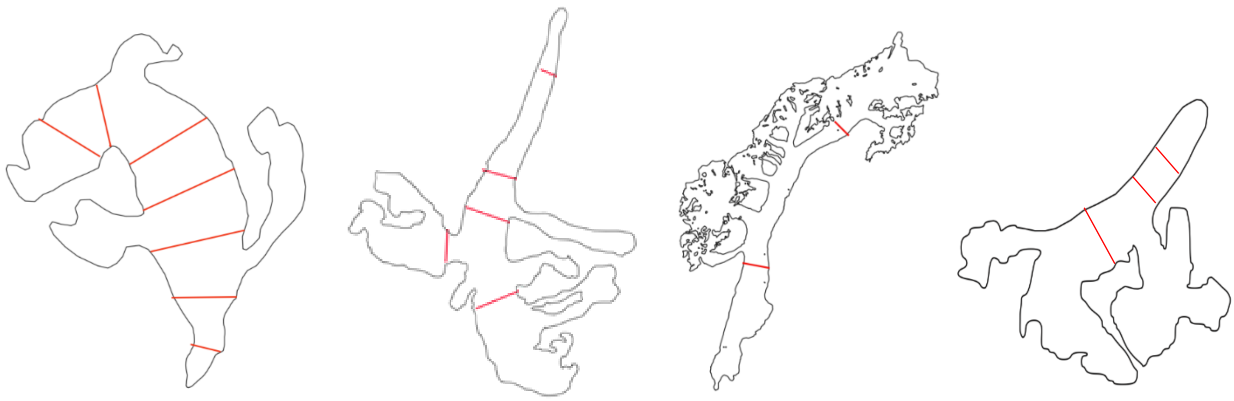

a) **b)** **c)** **d)**

Figure 6.7 Cross-sections used for calculating average shape factor of a) South Glacier, b) Chhota Shigri Glacier, c) Tasman Glacier and d) Patsio Glacier.

6.2.5 Model Sensitivity to Varying Data Availability

This section presents the results obtained through different experiments designed to explore the capability of the ice thickness model to extract information from limited subsets of ice thickness observations. These set of dedicated experiments, also investigate whether the spatial distribution of the field measured ice thickness has a noticeable influence on the model results, possibly leading to recommendations for the configuration of future data acquisitions. The main idea was to perform a set of experiments in which different subsets of the thickness observations are available for model calibration, and in which the ice thickness of the remaining profiles had to be estimated. Individual experiments are described in the following subsections. These analyses provide answer to the question: whether the proposed model capable of extracting information from sparse ice thickness observations or not?

Experiment Design:

A total of 10 experiments were defined. In each of these experiments, a different subset of profiles was defined investigating the effect of some peculiar layouts for the spatial distribution of the profiles available for calibration (Ex01 to Ex04), as well as the effect of the amount of data available for calibration (Ex05 to Ex10). The remaining profiles were only used for the validation of the results. These experimental designs and the performance metrics used are identical to those used in the ITMIX2 experiment (Farinotti et al., 2020) however is implemented on a single model (rather than 13 models) and smaller set of study glaciers, that is, four glaciers (instead of 23). Figure 6.8 visualizes the different layouts for the example of South Glacier.

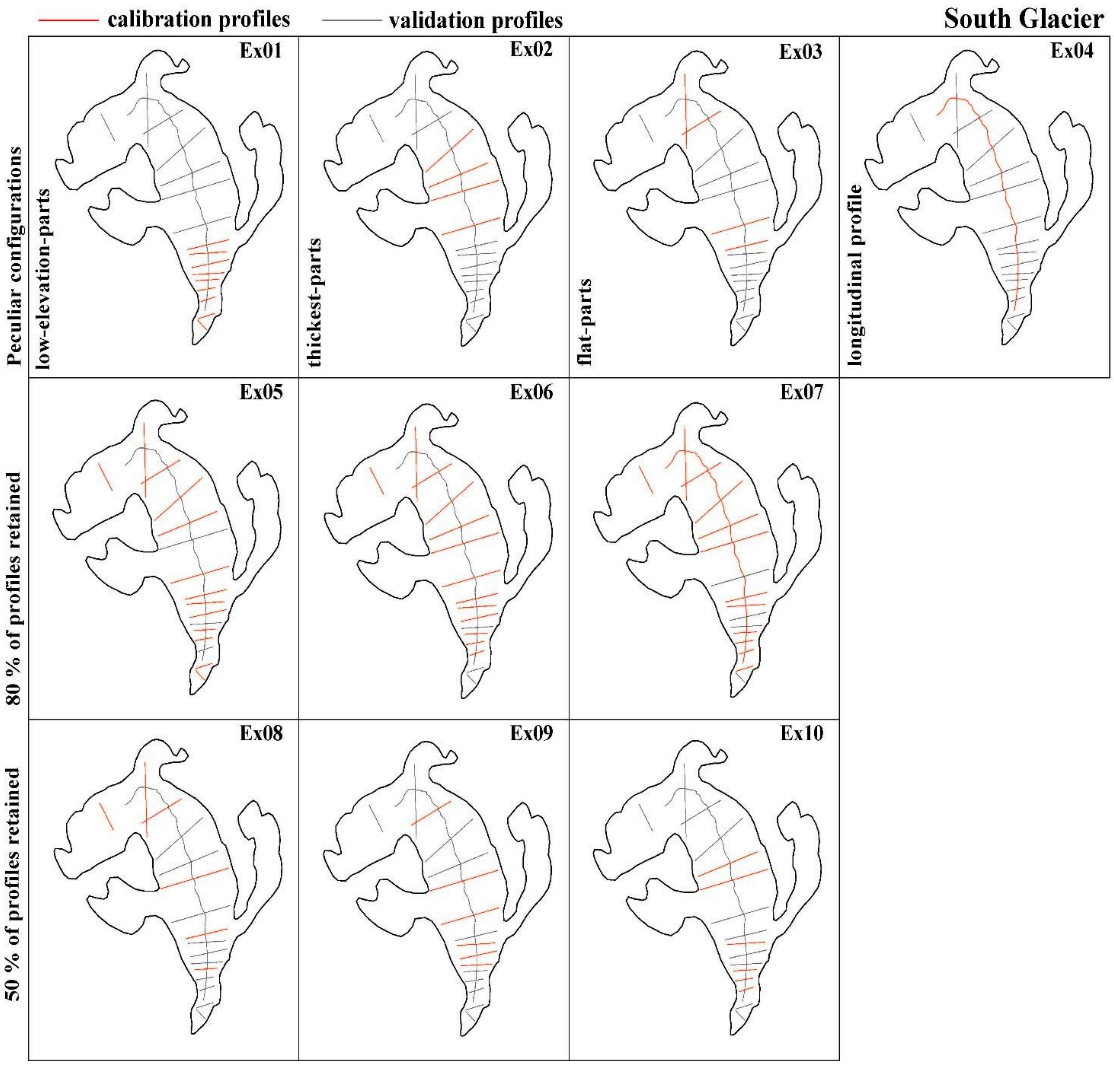

Figure 6.8 Profile layout for the 10 experiments considered in this study. Profiles indicate locations for which measured ice thickness is available. For each experiment (exp01 to exp10), a given subset of profiles was available for model calibration (red) whilst the remaining subset was used for validation (grey). Experiments 01 to 04 refer to peculiar configurations (see note within each panel) whilst experiments 05 to 10 consist of random selections of a given subset of profiles. The example refers to South Glacier.

Experiment 01: (low-elevation-parts) considers the scenario in which the available profiles are gathered towards the glacier's lowermost elevations. Such a configuration is sometimes encountered for ground-based ice thickness surveys (for example Hagg et al., 2013; Feiger et al., 2018) when the access to higher elevations is hampered by logistics or safety constraints. For any glacier, the experiment was produced by selecting those profiles that are located in the lowest quarter of the glacier's elevation range.

Experiment 02: (thickest-parts) represents the configuration in which the available profiles are located in the thickest parts of the glacier. To do so, all profiles were ranked according to the maximal ice thickness measured within each profile, and the first quarter of the so-ranked profiles was chosen.

Experiment 03: (flat-parts) in this configuration, the available profiles are located in the flat parts of the glacier. Here, due to easier logistics and accessibility, ground-based ice thickness surveys are common. The local surface slope used in the experiment was calculated using the available DEMs. It should be noted that the longitudinal profile was excluded from this analysis since it covers the whole range of slope profiles over the glacier.

Experiment 04: (longitudinal profile) only provided the longitudinal profile for calibration. This configuration is sometimes encountered for airborne surveys of valley glaciers (for example Gourlet et al., 2016), when aircraft's inability to move prevents the movement along the cross sections.

Experiments 05-07 (80% of total available profiles) are three different layouts in which 80% of the available profiles are randomly chosen for calibration. Similarly, Experiments 08-10 (50% of total available profiles) are three random arrangements of layouts constituting 50% of the available profiles. Further smaller subsets (such as 20% of total available profiles) of the available profiles were not considered here due to very small number of samples (i.e. less than or equal to one profile).

In all the following analyses, the model performance for a given experiment was evaluated against those ice thickness observations that were not used for calibration. Deviations are expressed as "model minus observation", so the negative values indicate that the model underestimates the ice thickness and vice versa. Since no information was available on the quality of the ice thickness observations, the observations are all considered to be error free for the calculations. It should be noted that the observations of a glacier often come from an individual field survey and thus the systematic errors are difficult to eliminate. To enable direct comparison between modelled thicknesses (which are gridded) and observed thicknesses (which can be available at any point location), the observed thicknesses are first rasterized on the modelling grid. For every grid-cell, this is done by computing the arithmetic average of all observations that fall within that cell. To allow for comparaison between glaciers of different size and ice thickness, the error/deviations are expressed as percentage deviations from the mean thickness. Table 6.2 summarizes the experiments implemented for each glacier and lists the mean ice thickness ($\bar{h}$) of the glaciers used to analyse the results.

Table 6.2 Overview of the experiments per glacier. For any glacier, "x" indicates that the particular experiments were performed. $\boldsymbol{\bar{h}}$ is the mean glacier ice thickness considered for the analysis.

	$\bar{h}$ (m)	Ex01	Ex02	Ex03	Ex04	Ex05-07	Ex08-10	Total no. of Experiments
South Glacier	60.9	x	x	x	x	x	x	10
Patsio Glacier	50	x	x	x	x	x	x	10
Chhota Shigri Glacier	102.7	x	x	x	x	x	x	10
Tasman Glacier	163.1	x	x	x			x	06

6.2.5.1 Overall Performance

The overall performance of the model from these 10 experiments can be characterised by three indicators: (1) the spread σ_n between individual solutions at profiles that were not used for calibration, (2) the deviation Δh_n between modelled and observed ice thickness at profiles that were not used for calibration, and (3) the deviation Δh_c between modelled and observed ice thickness for profiles that were available for calibration.

The first indicator σ_n, quantifies the degree to which similar solutions are produced when different calibration data are provided. The value of σ_n was computed for each location, which is determined by the difference between modelled ice thickness h_m and observed ice thickness h_o (for all experiments) during which that point was not available for calibration (that is a set of up to 10 values), divide by the mean ice thickness $\bar{h}$ of the considered glacier, and compute the standard deviation of the so-obtained differences,

$$\sigma_n = \text{stddev}\,\langle\frac{h_m - h_o}{\bar{h}}\rangle. \tag{6.7}$$

High values suggest that a given model is very sensitive to these data, with very different results being provided depending on which subset of profiles was used for calibration. Extremely low values, instead, indicate that the calibration procedure is insensitive to the input. Moderate values might thus be preferential as they hint at a compromise between model robustness and sensitivity.

Figure 6.9a shows the distribution of σ_n when the quantity is pooled across all the glaciers. The value of σ_n was found to be 35% the mean ice thickness which is similar to that observed for models Morlighem and Farinotti. This value is higher when compared with that of comparatively more rigorous models such as Brinkerhoff, Gantayat, GilletChaulet, Rabatel, VanPeltLeclerq and Werder (Farinotti et al., 2020), which all have σ_n medians below 13%. A possible reason behind this low median σ_n can be the fact that these models contain more than one level of error minimization steps through use of ice thickness, velocity, and mass balance datasets. The distribution of Δh_c, centred around zero (Figure 6.9b: Calibration) indicates a systematic overestimation of the actual thickness. The distribution of Δh_c also reveals that the model allow the thickness to fluctuate around the measured thickness (the interquartile range is in the order of 30% to 40%) rather than aiming at matching the calibration data exactly. The present model exhibits interquartile range of Δh_c which is higher when compared to data intensive models which aim at matching the calibration data exactly. This is the expression of a compromise between agreement with observations which can be affected by unknown uncertainties and biases and internal model consistency which is governed by the conservation of mass. This observation also suggests that even a limited subset of ice thickness observations is effective in constraining the mean ice thickness and glacier volume predicted by the model. Finally, the indicator Δh_n quantifies the model capabilities of correctly predicting the ice thickness at unmeasured locations. The distribution of Δh_n is shown in (Figure 6.9b: Validation) and reveals that the median deviations remain nearly unchanged and is centred around zero. This observation can be interpreted as a confirmation that the implemented calibration procedure is unbiased.

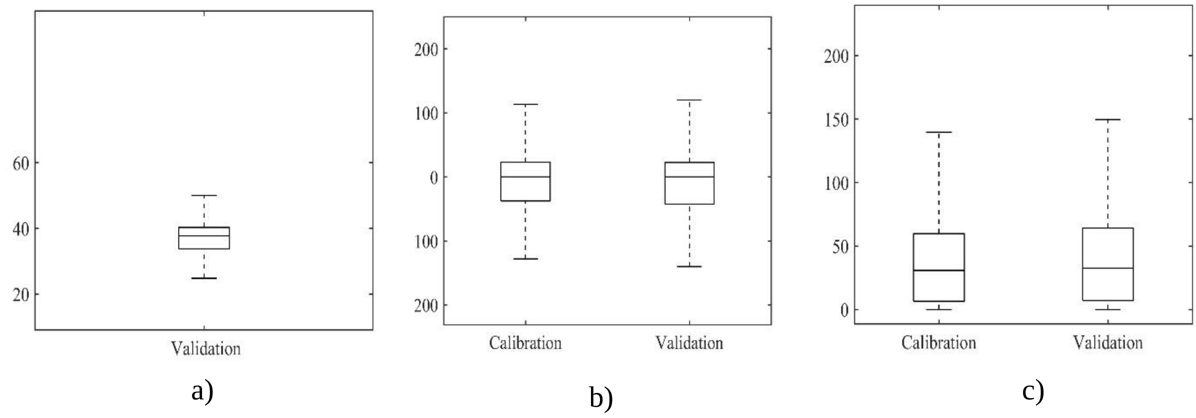

Figure 6.9 (a) Standard deviation of the difference between modelled and observed ice thickness at the locations of profiles that were used for model validation. (b) Deviations (dev) between modelled and observed ice thickness for the locations used for model calibration and validation. (c) same as (b) but deviations are expressed in absolute terms. Boxplots show the 95% confidence interval (whiskers), the interquartile range (box), and the median (lines within box). All values are expressed relatively to the mean ice thickness of the corresponding glacier.

6.2.5.2 Influence of the Distribution of Ice Thickness Observations

The effect that the spatial distribution of the ice thickness observations has on the model performance is quantified through experiments Ex01 to Ex04. Figure 6.10 (a-b) shows the deviation between modelled and observed ice thickness at profile locations that were not used for calibration.

The experimental configurations using low-elevation parts (Ex01) and thickest parts (Ex02) show somewhat higher absolute deviations than the situations in which the available observations are biased towards flattest parts (Ex03) and longitudinal profile only (Ex04) of the glaciers (Figure 6.10a). The effect is particularly visible where the median absolute deviation for Ex04 is lowest. The error introduced by using low-elevation parts (Ex01) can be mainly due to an overestimated shape factor which is representative of the lower region (commonly the shallow most region and high shape factor) of glacier while other part of the glacier (with lower value of shape factor) are mis represented. Together, the result indicates that, although it is convenient from the logistical point of view, survey configurations in which low elevations are sampled should be avoided, or at least complemented with measurements gathered along glacier flowline.

Figure 6.10b shows the under and over estimation observed for the four experiments. Ex01, Ex02 and Ex04 show an underestimation by the model for the validation region of the study glaciers. Ex03 on the other hand shows a remarkably opposite behavior and shows and overestimation. This is perhaps due to the fact that the flattest part in the sampling also covers the part where measured ice thickness is the highest for the glaciers and thus overestimated ice thickness is observed for the validation region.

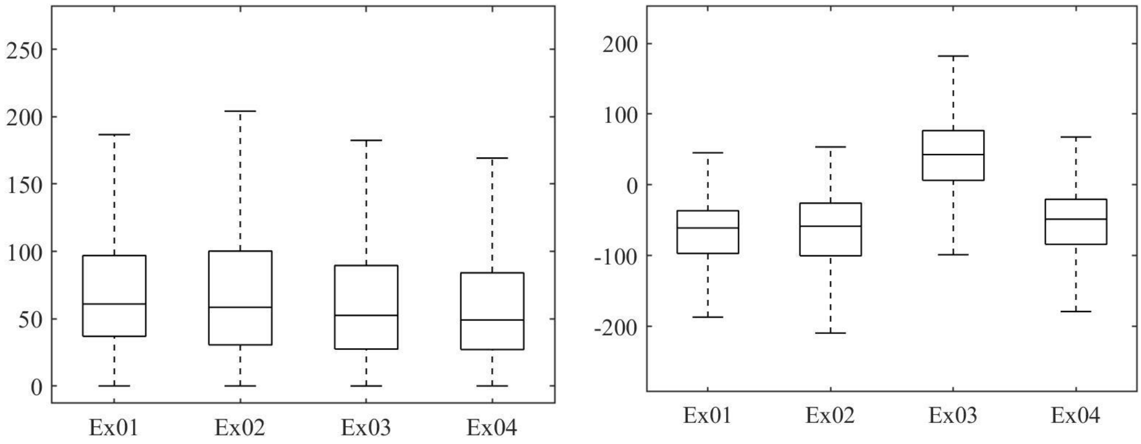

a) b)

Figure 6.10 Distribution of model absolute deviation (a) and actual deviation (b) when the ice thickness observations used for calibration show a peculiar spatial distribution. The individual boxplots perceive the situations in which the observations are biased towards low elevations (Ex01), the thickest parts (Ex02), the flattest parts (Ex03) of the glacier. In Ex04, only observations along a longitudinal profile are provided for calibration. Values are given relatively to the mean glacier thickness.

6.2.5.3 Influence of the Availability of Ice Thickness Observations

The available ice thickness observations are generally sparse which raises an important question is how the ice thickness model performs to the amount of ice thickness data available for calibration. Figure 6.11 shows how the absolute deviation between modelled and observed ice thickness evolves for Ex05 to Ex10, i.e. during the experiments in which the availability of profiles used for model calibration is reduced. As expected, the deviations increase when fewer observations are available. The results show that the median absolute deviations increase from 31% of the mean ice thickness when 80% of the measured profiles are retained for calibration (experiments 05-07), to 38% when 50% of the profiles are retained (experiments 08-10). This show a less pronounced decrease in performance when fewer data are available. This displays less sensitivity to the availability of observations. Note, however, a substantial increase in outliers when reducing the data availability from 80% of profiles retained to 50%; the 95% confidence interval increases from 87.8% the mean ice thickness to 161.3%. The consistency between various experiments could be both due to model stability (i.e. the model's capability of extracting information from limited ice thickness observations) or due to the model's calibration strategy not being able to take various profile configurations fully into account.

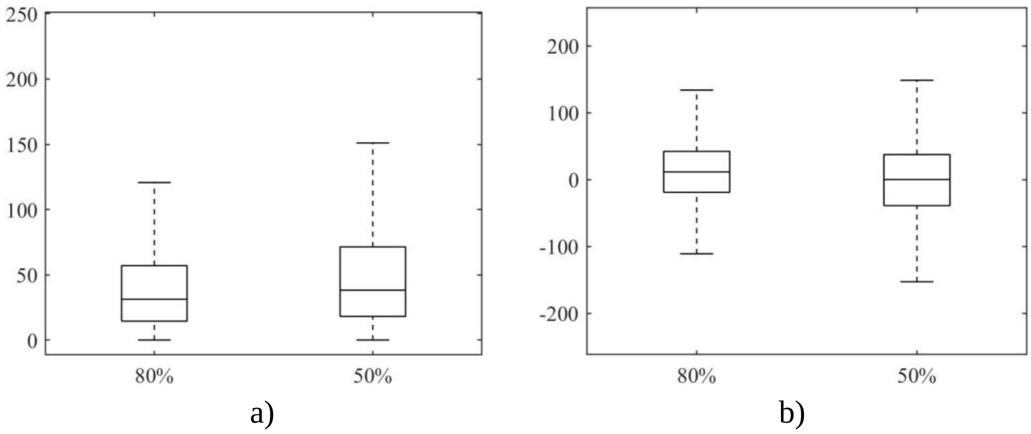

Figure 6.11 a) Absolute deviation and b) actual deviation between modelled and observed ice thickness resulting from Ex05 to Ex10.

Aiming at characterising the degree to which the proposed ice thickness model can benefit from sparse in-situ thickness observations. Considering the 10 different experiments conducted over set of four glaciers to infer the effect that both availability and spatial distribution of ice thickness observations have on model performance. The main results of the experiments can be summarised as follows:

- The model showed significant variabilities in the results of different experiments in the order of 57% the mean ice thickness which corresponds to flexibility of the calibration procedure adopted here. Whilst low variabilities are an indication for model robustness, it also seems to reflect lack of flexibility in the calibration procedure.
- It is observed that a few observations are sufficient to correctly capture the mean glacier thickness (Figure 6.9). This can be observed from the bias in model which does not shift between the experiments when the amount of observations are varied and reduced upto 20%. This is of particular importance to the researchers

or end users who depend on the glaciers' total stored volume instead of spatial distribution of ice thickness.

- The spatial distribution of the ice thickness observations has only a small amount of effect on the estimated ice thickness (Figure 6.10). The only configuration that should be avoided is the one in which calibration is done using the observations from the lowest parts of a glacier. Although convenient due to the logistics reasons,, this configuration tends to over-sample thin glacier parts thus resulting in a bias towards overestimated ice thickness. On the contrary, a preferential sampling along the glacier flowline prevents large deviations, successfully constraining the total glacier volume.

6.3 Comparison with Existing Approaches

The proposed ice thickness model estimates were compared with the existing variants of models that have been applied globally (Farinotti et al., 2019). Considering an operational scenario where complete and accurate knowledge of model parameters may not be available. The estimated ice thickness following scenario 2 (fixed *A*, *n* and glacier specific calibrated *f*) was used for this comparison. Furthermore, these results were compared with the existing approaches to ice thickness estimation implemented at global scale (Farinotti et al., 2019). Figure 6.12 shows the boxplots of the errors in the estimates (mean deviation from observed ice thickness) for these models. Deviations are expressed as 'model minus observation', where negative values indicate underestimation of ice thickness. The estimated ice thickness by the proposed model of each study glacier was compared with the models included by Huss and Farinotti (2012): Model 1, Frey et al., (2014) : Model 2, Maussion et al., (2019) : Model 3, Fürst et al., (2017): Model 4 and Ramsankaran et al., (2018) : Model 5. All the models infer the ice thickness distribution from surface characteristics (such as elevation and slope), an estimate of the glacier mass balance and principles of ice flow dynamics. A description of the individual models used for comparison are described as follows:

Model 1 (Huss and Farinotti 2012) - The ice volume flux across individual cross sections is estimated by integrating the surface mass balance of the corresponding area. The method eliminates the necessity of a steady-state assumption while estimating the difference of mass balance and ice thickness change collectively rather than imposing constraints on the two terms separately. All calculations are performed on elevation bands. Mean elevation-band thickness is then extrapolated to a spatially distributed field by considering local surface slope and the distance from the glacier margin.

Model 2 (Frey et al., 2014) – also referred to as GlabTop2, the final ice thickness distribution is derived from interpolation of the randomly selected points and the condition of zero ice thickness at the glacier margin. The procedure by which the random points are selected has an influence on the shape of the obtained bedrock topography.

Model 3 (Maussion et al., 2019) - The major difference between Maussion and the approaches Model 1 is that the surface mass balance is not prescribed as a linear function of elevation but with a temperature-index model which is derived from climate data (Marzeion et al., 2012).

Model 4 (Fürst et al., 2017) - The forward model is based on Elmer/Ice (Gagliardini et al., 2013) and the mass conservation approach of Morlighem et al., (2011). It is a minimization based approach, where the cost function is not linked to surface elevations but the function penalizes negative ice thickness values, the mismatch between modelled and observed surface velocities, the mismatch between modelled and observed surface mass balance, and strong spatial variations in ice thickness or surface velocities.

Common to all five models, all ice thickness estimates refer to the glacier outlines taken from the RGI version 6.0. For every glacier, the surface topography was extracted from the hole-filled Shuttle Radar Topography Mission (SRTM) DEM version 4 (Patsio Glacier, Chhota Shigri Glacier, Tasman Glacier) and the Arctic DEM version 2.0 (South Glacier). More detailed description of the above five models is given in Farinotti et al., (2019). To have a more reliable comparison between these five models and the proposed one, same DEMs were used to estimate ice thickness from the proposed ice thickness model. Figure 6.12(a-d) show the boxplot of the error in estimated ice thickness for each glacier by the proposed model and the five above mentioned models. A side-by-side comparison figure was not given for model inter-comparison since a more quantitative statistical comparison was given which was adapted (and is widely accepted in glaciology community) in recent study (Farinotti et al., 2019) where different types of glaciers (with different amount of validation data available) are used in the comparison. From both the distribution of error and their corresponding median, it is evident that no single model is found to give best estimates consistently for all the study glaciers. The proposed model can be seen to be least biased specially for Tasman Glacier (Figure 6.12d). When compared with Model 1 (Farinotti et al., 2009), the proposed model gave slightly less error for Chhota Shigri and Patsio Glacier (Figure 6.12b and c). However, higher error was observed for South Glacier with overestimation in the estimated ice thickness. This could be due to the previously reported surge conditions for South Glacier (Pauli and Flowers 2009) which introduces error in the ice flux derived from glacier surface velocity which leads to overestimating the flux and thus ice thickness. On the other hand, the error in Tasman Glacier is significantly less when compared with Model 1 estimates. One of the factors responsible could be the glacier profiles for the Tasman Glacier are complicated by multiple tributaries delivering mass into the Tasman Glacier catchment (for example, Rudolf and Darwin Glaciers). The simple assumption in the Model1 that the ice flux is distributed linearly with distance from the margin in each elevation band may be inaccurate. Whereas such linear assumption is not present in the proposed model. Considering, a rigorous parameterization that was carried out for Model1, utilizing the available field measurements (Farinotti et al., 2019) in the same region, the proposed model offers a simple approach to model parameterization and performed better for Tasman Glacier. More specifically, the former model undertook the parameterization by minimizing the misfit (i) the region-by-region average of the mean deviations of all points of the glacier, (ii) the glacier-area-weighted average of the mean deviation over all points of the glacier, (iii) the average of the difference between calculated and reported mean ice thickness, and (iv) the glacier-area-weighted average of the difference between calculated and reported mean ice thickness. However, the proposed model adopted simpler as well as glacier specific shape factor parametrization approach with universally calibrated Glen's flow parameters (*A* and *n*) as described in Section 6.2.3 scenario 2, and the inputs used were captured through remote sensing which gave a better representation of glacier dynamics.

In general, the error distribution obtained from the GATHI model (Figure 6.12) was found to be comparable to the other models for three study glaciers (South Glacier, Chhota Shigri Glacier and Patsio Glacier). Whereas, the GATHI model was seen to be least biased (among the other models) for Tasman Glacier. Apart from the difference in modelling approach, one of the possible reasons for relatively lesser performance could be the large difference in the timestamp of model inputs and validation data used for these five models.

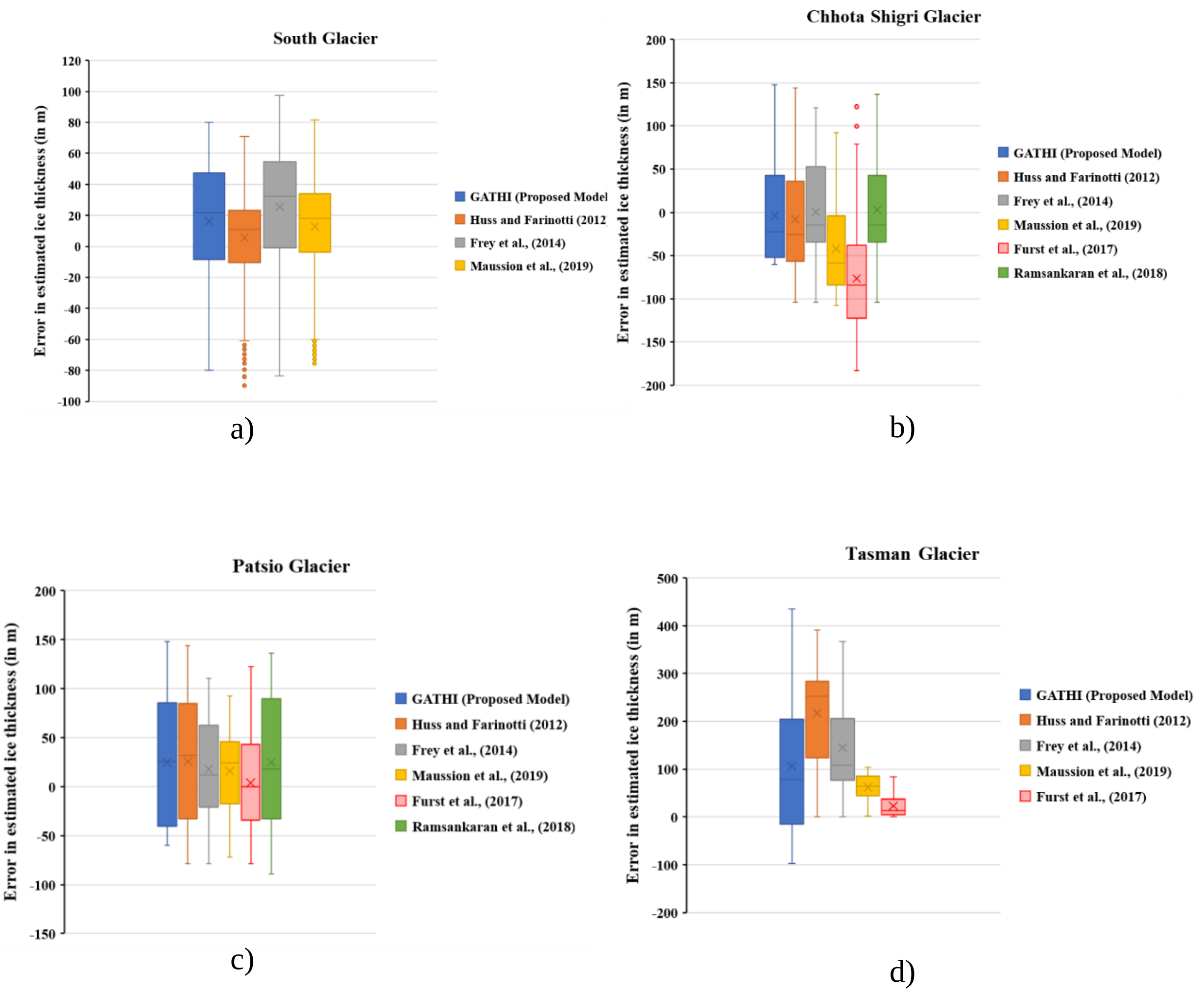

Figure 6.12 Comparative boxplot of the error (in m) from the proposed model (GATHI) and the modelled estimates taken from Farinotti et al., (2019) for a) South Glacier, b) Chhota Shigri Glacier, c) Patsio Glacier, and d) Tasman Glacier.

6.4 Sources of Error

The uncertainties often lead to biased estimates even for calibrated ice thickness models, especially when appropriate calibration data for model are rarely available (Helton et al. 2010). The uncertainties involved in a modelling process can be classified by the source model component (Liu and Gupta, 2007).

1. Modelling errors: Models use various assumptions and approximations to characterize a complex real-world system which introduces some inherent error in the system. The computational implementation which requires discretization (over space) also contributes

to this error. If the model conceptualization is inadequate, that is, physically significant processes are ignored, major errors may follow.

Specifically, for the present study, the modelled ice thickness is affected due to inherent assumptions such as Shallow Ice Approximation and the ice flux calculated from apparent mass balance.

2. Parameter errors: Parameters represent system properties continuously varying over space and time. Due to the spatiotemporal aggregation of parameters required for practical uses, the real world heterogeneity is inadequately represented quite often. Additionally, most parameter values cannot be directly measured in the field (such as basal shear stress) or vary continuously (temperature conditions and ice properties) making measurements expensive. For instance, ice density is very hard to monitor in the field. The indirect estimation methods employed, such as expert knowledge or model calibration, introduce uncertainty due to the ambiguity of the optimal parameter choice (Beven, 2007). For example, while modelling the ice thickness, the shape factor parameter which represents the nature of cross section at a given location, is aggregated (over the glacier) and a generalized value is used. This aggregated value can lead to over or under estimation of the ice thickness.

3. Data or measurement errors: The uncertainty caused by model inputs fall into this category. They can be attributed to errors in the measuring device or the incompatibility of the observation scale and corresponding model estimates which may require spatio-temporal aggregation or interpolation (Waller et al., 2018). The errors associated with the location of the field measured data collected can also add to uncertainty in the ice thickness estimates for a given location (Martín-Español et al., 2016). For example, an over estimation in input velocity can lead to over-estimated ice thickness distribution. Similarly, errors in the used DEMs can propagate as the input slope and thus affect the output i.e. estimated ice thickness.

6.5 Chapter Summary

This chapter presented an overview of the proposed ice thickness modelling framework developed in this thesis for glacier ice thickness estimation using remote sensing inputs. First, the concept of mass continuity was briefly introduced. Following this, the ice thickness modelling was presented in detail. Starting with sensitivity analysis of ice thickness towards model parameters, the subsequent sections evaluated the performance of the ice thickness estimation model through application on four study glaciers. The capability of the ice thickness model application was explored via two different scenarios for glaciers without any field ice thickness measurements available. the transferability of the model parameter from one glacier (with available field observations) to other glacier sharing similar characteristics (with no available field measurements) is explored. Furthermore, considering that the geometry-based parameter *f* cannot be replicated from one glacier to other, potential for its field-data-independent calibration is explored. Accordingly, this self-calibration of the shape factor parameter showed varied level of improvements for the study glaciers in the mean error (upto 12% of mean thickness) over the commonly adapted shape factor value. Furthermore, to explore the effect of calibration data on the model, the model's sensitivity was evaluated towards observation spatial and quantity-related characteristics. This evaluation was performed through set of 10 experiments. Overall, the effect of the spatial distribution and amount of the field measurement available for calibration was seen on model performance. This evaluation revealed that the model is sensitive to data availability with most useful results observed when for Ex04 where the calibration was performed using data along the flowline. Lastly a comparison with existing models applied at global scale was discussed.

7 SUMMARY, CONCLUSION AND FUTURE PERSPECTIVES

The principal aim of this thesis was to develop a simple model for estimation of distributed glacier ice thickness by using purely remote sensing dataset and eliminate the use of field measurements. An effort was made to introduce field-data-independence at every major step. The proposed methodology for glacier velocity as well as ice thickness estimation were developed and tested over four study glaciers. Specifically, the following objectives were addressed:

- Development of a remote sensing based automated feature tracking algorithm to estimate glacier surface velocity.
- Development of a physics-based glacier ice thickness model to estimate spatially distributed ice-thickness using remote sensing inputs.

Next section outlines the progress made towards achieving this goal and major conclusions drawn aligned with the above-mentioned objectives.

7.1 Summary and Major Conclusions

7.1.1 Glacier Surface Velocity Estimation

A new algorithm for glacier feature tracking named as SWIFT (**S**patially varying **WI**ndow based maximum likelihood **F**eature **T**racking) has been developed where an automatic window size estimation technique is introduced. This algorithm utilises both optical data (to determine the window size) and SAR data (to perform feature tracking). The proposed glacier feature tracking algorithm uses a spatially varying window size unlike other existing softwares like SNAP, SARscape, CIAS and COSI-Corr that cannot provide the flexibility of spatially varying window sizes, being one of the main contributions by this study. Moreover, this method for estimation of window size can be implemented in combination with other existing feature tracking methods. The proposed glacier surface velocity tracking algorithm has been tested for three different glaciers (South Glacier, Chhota Shigri Glacier and Tasman Glacier). The obtained results from the performance evaluation through variety of experiments are discussed as follows:

a) Performance evaluation against normalized cross correlation method (NCC)

The NCC was chosen to compare the results from the proposed feature tracking algorithm since it is most widely used. Zone wise analysis for each glacier was carried out by comparing the velocity estimates from the proposed approach and the best performing NCC based estimates. Here, the best performing NCC based estimates were obtained by calibration of window size using field measured velocity data. Results revealed the better performance of the proposed feature tracking approach in the middle and upper zones. Whereas in the lower zone, the proposed method gave relatively higher RMSEs. Here, the main advantage of the proposed approach is the estimation of a spatially varying window size without using field data. The results indicate that this proposed technique can provide a better estimate for a glacier where glacier specific window sizes could not be obtained. The present method uses spatially varying window size and is different from the existing variable window size techniques (Heid and Kaab, 2012) where the window size is varied at iterations but still the window size is spatially constant. This window size selection technique is independent of glacier type or its environment setting, thus this technique can be applied to the glaciers in any setting.

b) Impact of the timestamp of optical data used

An assessment was carried out for potentially alternate timestamp of optical data that could be used (when the data is not available for given study period) in the velocity estimation. Results obtained for South Glacier demonstrates that the proposed method is robust towards the choice of optical data given that the timestamp of the optical data is at annual separation from the study period. Here, an implicit assumption was made that there is negligible or no change in the glacier surface within a year. Whereas large temporal differences (~10 years from the study period) led to larger errors in the estimated velocities. This is probably due to noticeable changes occurring over the glacier surface during such large time period which invalidates the aforementioned assumption.

c) Impact of SAR data bandwidth

An analysis of the impact of SAR data bandwidth on the estimated velocities confirmed the appropriateness of longer wavelength data such as L-band. The results obtained for Tasman Glacier indicated that L-band (with HH Pol) performed better than C-band (with VV Pol) in debris covered region with less gaps in velocity estimates and glacier wide higher accuracy. However, due to limited polarity of data available, the effect due to different polarization in SAR data could not be explored in this study.

d) Effect of the difference between spatial resolution of SAR and optical data

An analysis was performed to examine the impact on glacier velocity estimation due to difference in the spatial resolution of the SAR and optical imagery. For this analysis, South Glacier was considered because the required combination of the SAR and optical data pair were available for the glacier. In the first case, the optical imagery of coarser resolution with respect to SAR data (optical data: ASTER; SAR data: ENVISAT) led to better estimates both in terms of magnitude and direction of the estimated surface velocity. However, in the second case, the optical imagery of similar resolution with respect to SAR data (optical data: Landsat 8; SAR data: Sentinel 1) led to comparatively poorer velocity estimates both in terms of magnitude and direction of the estimated velocity. The relatively better performance in Case-1 could be due to the fact that the optical data at coarser resolution is relatively free from smaller glacier surface features which could be considered as noise. Similarly, the finer resolution SAR data due to its surface penetration capability can also be considered to be free from the smaller glacier surface features which may lead to noise. Thus, this SAR and optical data pair (Case-1) can synergistically lead to better estimate.

e) Comparison with spatially fixed window size-based maximum likelihood feature tracking

The performance of the proposed feature tracking method which uses a spatially varying window size (SVWS) was compared with the estimates obtained when spatially fixed window size (SFWS) was used. Both SVWS and SFWS were implemented with the proposed maximum likelihood-based feature tracking method. For the latter case (i.e. SFWS) the standard window sizes have been used (i.e., 32 pixels × 32 pixels and 64 pixels × 64 pixels). The obtained results indicate that the SVWS based implementation performs consistently better for all the three study glaciers.

The proposed feature tracking algorithm focuses on automation rather than computational efficiency. However, computationally, this tracking approach does not pose any severe limitations and it is dependent upon the size of the glacier and the window size generated.

For example, with a 4.6 GHz Intel® Core i7- 8700 CPU of 16GB RAM, the total Central Processing Unit (CPU) time (applicable to both parallel and serial processing) may vary from several minute to few hours because of the spatially varying window size and glacier size. Similar to other NCC based methods, large intra annual changes on the glacier surface limit the accuracy of this feature tracking approach. Nevertheless, the proposed glacier feature tracking method holds potential for feature tracking in glaciers with no prior field information available.

7.1.2 Ice thickness Modelling using Remotely Sensed Glacier Surface Velocity

The proposed ice thickness model is named GATHI **(G**l**A**cier ice **THI**ckness distribution using remote sensing) which requires only remotely sensed inputs such as surface velocity and DEM. Following the sensitivity analysis of the modelled ice thickness estimates towards model inputs, the performance of the ice thickness estimation model was subsequently assessed through application in four study glaciers. To explore the applicability of the ice thickness model to glaciers without any field ice thickness measurements available, two different scenarios were considered. In scenario 1, the transferability of the model parameter from one glacier (with available field observations) to other glaciers sharing similar characteristics (with no available field measurements) was explored. In scenario 2, considering that the geometry-based parameter f cannot be replicated from one glacier to other, potential for field-data-independent calibration (Ramsankaran et al., 2018) was explored. Furthermore, to explore the effect of calibration data on the model, the model's sensitivity was evaluated towards observation's spatial and quantity-related characteristics. This evaluation was performed through set of 10 experiments. Lastly, a comparison with some of the existing models applied at global scale was also discussed. The obtained results are discussed as follows:

a) Model application to glaciers where no field measured ice thickness is available

Interesting similarities in the model parameters were noticed while investigating the transferability of calibrated model parameters among similar glaciers under scenario 1. For this analysis, all the four study glaciers were considered which can be categorized as temperate type glaciers thus sharing similar temperature conditions. Due to similar temperature conditions, it can be fairly assumed that the material properties of ice (which is predominantly dependent on temperature) is same for these glaciers. Following this hypothesis, the two Glen's flow law parameters used in the proposed GATHI model (*A* and *n*) can be expected to be constant among the temperate type glaciers. This was confirmed when the obtained calibrated Glen's flow parameters ($A = 3.8*10^{-24}$ and $n = 3$) were same for all the four study glaciers. Here, the other parameter *f* (which is dependent on glacier geometry) was kept constant at the standard value of 0.8. These observations revealed that for the ice thickness model application, the calibrated parameters $A = 3.8*10^{-24}$ and $n = 3$ can be assumed to be constant for temperate type glaciers. Results obtained from scenario 2 showed that the field-data-independent calibration led to noticeable improvement in mean error of the ice thickness. The error in estimated ice thickness was reduced by 5-17% (of mean observed ice thickness) when calibrated shape factor was used instead of the uncalibrated shape factor. Here the other two model parameters (*A* and *n*) were kept constant.

b) Effect of calibration data on the ice thickness model performance

Different experiments were designed in this study to explore the capability of the ice thickness model to extract information from limited subsets of ice thickness observations. These set of dedicated experiments, also investigate whether the spatial distribution of the field measured ice thickness has a noticeable influence on the model results, possibly leading to recommendations for the configuration of future data acquisitions. The main idea was to perform a set of experiments in which different subsets of the thickness observations are available for model calibration, and in which the ice thickness of the remaining profiles had to be estimated. Altogether, the result indicates that, although it is convenient from the logistical point of view, survey configurations in which low elevations are sampled should be avoided, or at least complemented with measurements gathered along glacier flowline.

c) Comparison with the existing models applied at global scale

The error in the estimated ice thickness for each glacier by the proposed GATHI model was compared with five models (Model-1: Huss and Farinotti (2012), Model-2: Frey et al., (2014), Model-3: Maussion et al., (2019), Model-4: Furst et al., (2017), Model-5: Ramsankaran et al., (2018) used in Farinotti et al., (2019) for global scale ice thickness estimation. From both the distribution of error and their corresponding median values, no single model was found to give best estimates consistently for all the study glaciers, which is consistent with conclusions given by Farinotti et al., (2019). In general, the error distribution obtained from the GATHI model was found to be comparable to the other models for three study glaciers (South Glacier, Chhota Shigri Glacier and Patsio Glacier). Whereas, the GATHI model was seen to be least biased (among the other models) for Tasman Glacier. Apart from the difference in modelling approach, one of the possible reasons for relatively lesser performance could be the large difference in the timestamp of model inputs and validation data used for these five models.

7.2 Limitations of the Work

Considering the challenges in field-based observations, following limitations are encountered in the present study.

- Due to limitations in the available SAR data such as polarization, the effect of SAR polarization over the glacier feature tracking approach could not be explored in this study.
- The developed approach for feature tracking was compared with the NCC method which forms the basis of the existing softwares such as CIAS, COSI CORR, SARscape and SNAP, however a one-to-one comparison with all the existing software has not been performed in this study.
- The observed ice thickness data used for validation that has been taken from the most compiled freely accessible **Gla**cier ice **Thi**ckness **Da**tabase (GlaThiDa). However, no specific information was available on the accuracy of these ice thickness observations. Thus, the observations are all considered to be error free for the calculations. While average deviations over multiple points remain unaffected; it is acknowledged that error-free observations are not realistic. This is because the observations of a given glacier often stem from an individual field campaign, and systematic interpretation of errors are thus difficult to exclude.
- By definition, the shape factor varies over a glacier. However, in the present study to maintain simplicity, the proposed GATHI model considers a single value of shape factor for a glacier.

7.3 Major Contributions from this Thesis

The present study resulted in the following contributions to the field of remote sensing of glaciers.

- Developed an algorithm useful for glacier velocity estimation which provides flexibility in terms of spatially varying window size unlike other existing softwares.
- Developed an automated window size determination technique useful for feature tracking, to estimates surface velocity of the glaciers where no field measured data is available.
- Developed a physics-based ice thickness model (GATHI) which requires only remote sensing inputs such as annual glacier surface velocity and DEM.
- Collected the ice thickness data for Patsio Glacier in a data scarce region like Himalaya shall be useful as validation data for future glacier ice thickness modelling studies.

7.4 Future Perspectives

This section lists some of the immediate future directions in which the research initiated in this thesis could be advanced:

- The developed feature tracking algorithm can be rigorously tested for glaciers with varying level of debris cover and glaciers in the polar region such as marine terminating glaciers. This will help us in assessing the potential of global scale applicability of the developed glacier surface velocity estimation algorithm.
- Automation of the proposed feature tracking algorithm should be explored to make it more efficient for large area.
- The model structure of the ice thickness estimation model can be further improved by considering the effect of debris cover in the model. This work will dramatically improve the applicability of ice thickness model for debris covered glaciers.
- The present study has been carried out for four glaciers representing different glacier characteristics (size, orientation) and different climatic regions. A few more glaciers from the same region would certainly add to the validation. A more rigorous testing at a regional scale shall be conducted in this regard. Moreover, further experiments need to be carried out to examine the implementation capability of the proposed ice thickness model at regional scale considering the factors such as availability of data and computational efficiency.

- Including a spatially distributed shape factor instead of a glacier wide average value, which is realistic representation of different cross sections, should be explored in future research to improve upon the ice thickness estimation.

PUBLICATIONS BY THE CANDIDATE TILL DATE

Kumari, S., Ramsankaran, R.A.A.J. and Walker, J.P., 2019, July. Impact of Window Size in Remote Sensing Based Glacier Feature Tracking–a Study on Chhota Shigri Glacier, Western Himalayas, India. In *IGARSS 2019-2019 IEEE International Geoscience and Remote Sensing Symposium* (pp. 4175-4178). IEEE.

REFERENCES

Ahn, Y. and Howat, I.M., 2011. Efficient automated glacier surface velocity measurement from repeat images using multi-image/multichip and null exclusion feature tracking. *IEEE Transactions on Geoscience and Remote Sensing*, *49*(8), pp.2838-2846.

Allen, S.K., Schneider, D. and Owens, I.F., 2009. First approaches towards modelling glacial hazards in the Mount Cook region of New Zealand's Southern Alps. *Natural Hazards and Earth System Sciences*, *9*(2), pp.481-499.

Altena, B., Scambos, T., Fahnestock, M. and Kääb, A., 2019. Extracting recent short-term glacier velocity evolution over southern Alaska and the Yukon from a large collection of Landsat data. *The Cryosphere*, *13*(3), pp.795-814.

Altena, B. and Kääb, A., 2020. Ensemble matching of repeat satellite images applied to measure fast-changing ice flow, verified with mountain climber trajectories on Khumbu icefall, Mount Everest. *Journal of Glaciology*, 66(260), pp.905-915.

Andersen, M.L., Stenseng, L., Skourup, H., Colgan, W., Khan, S.A., Kristensen, S.S., Andersen, S.B., Box, J.E., Ahlstrøm, A.P., Fettweis, X. and Forsberg, R., 2015. Basin-scale partitioning of Greenland ice sheet mass balance components (2007–2011). *Earth and Planetary Science Letters*, *409*, pp.89-95.

Azam, M.F., Wagnon, P., Ramanathan, A., Vincent, C., Sharma, P., Arnaud, Y., Linda, A., Pottakkal, J.G., Chevallier, P., Singh, V.B. and Berthier, E., 2012. From balance to imbalance: a shift in the dynamic behaviour of Chhota Shigri glacier, western Himalaya, India. *Journal of Glaciology*, *58*(208), pp.315-324.

Bahr, D.B., Pfeffer, W.T. and Kaser, G., 2015. A review of volume-area scaling of glaciers. *Reviews of Geophysics*, *53*(1), pp.95-140.

Barnes, P., Tabor, D. and Walker, J.C.F., 1971. The friction and creep of polycrystalline ice. *Proceedings of the Royal Society of London. A. Mathematical and Physical Sciences*, *324*(1557), pp.127-155.

Beniston, M., Farinotti, D., Stoffel, M., Andreassen, L.M., Coppola, E., Eckert, N., Fantini, A., Giacona, F., Hauck, C., Huss, M. and Huwald, H., 2018. The European mountain cryosphere: a review of its current state, trends, and future challenges. *The Cryosphere*, *12*(2), pp.759-794.

Beven, K., Smith, P. and Freer, J., 2007. Comment on "Hydrological forecasting uncertainty assessment: Incoherence of the GLUE methodology" by Pietro Mantovan and Ezio Todini. Journal of Hydrology, 338(3-4), pp.315-318.

Binder, D., Brückl, E., Roch, K.H., Behm, M., Schöner, W. and Hynek, B., 2009. Determination of total ice volume and ice-thickness distribution of two glaciers in the Hohe Tauern region, Eastern Alps, from GPR data. *Annals of Glaciology*, *50*(51), pp.71-79.

Blatter, H., 1995. Velocity and stress fields in grounded glaciers: a simple algorithm for including deviatoric stress gradients. *Journal of Glaciology*, *41*(138), pp.333-344.

Brinkerhoff, D.J., Aschwanden, A. and Truffer, M., 2016. Bayesian inference of subglacial topography using mass conservation. *Frontiers in Earth Science*, *4*, p.8.

Bohleber, P., Sold, L., Hardy, D.R., Schwikowski, M., Klenk, P., Fischer, A., Sirguey, P., Cullen, N.J., Potocki, M., Hoffmann, H. and Mayewski, P., 2017. Ground-penetrating radar reveals ice thickness and undisturbed englacial layers at Kilimanjaro's Northern Ice Field. *The Cryosphere*, *11*(1), pp.469-482.

Bolch, T., Kulkarni, A., Kääb, A., Huggel, C., Paul, F., Cogley, J.G., Frey, H., Kargel, J.S., Fujita, K., Scheel, M. and Bajracharya, S., 2012. The state and fate of Himalayan glaciers. *Science*, *336*(6079), pp.310-314.

Budd, W.F. and Allison, I.F., 1975. An empirical scheme for estimating the dynamics of unmeasured glaciers. In *Proceedings of the Moscow Symposium "Snow and Ice* (pp. 246-256).

Cai, C., Rignot, E., Menemenlis, D. and Nakayama, Y., 2017. Observations and modeling of ocean-induced melt beneath Petermann Glacier Ice Shelf in northwestern Greenland. *Geophysical Research Letters*, *44*(16), pp.8396-8403.

Calvo, E., Pelejero, C., Pena, L.D., Cacho, I. and Logan, G.A., 2011. Eastern Equatorial Pacific productivity and related-CO2 changes since the last glacial period. *Proceedings of the National Academy of Sciences*, *108*(14), pp.5537-5541.

Carr, S.J., Lukas, S. and Mills, S.C., 2010. Glacier reconstruction and mass-balance modelling as a geomorphic and palaeoclimatic tool. *Earth Surface Processes and Landforms*, *35*(9), pp.1103-1115.

Casey, J.A., Howell, S.E., Tivy, A. and Haas, C., 2016. Separability of sea ice types from wide swath C- and L-band synthetic aperture radar imagery acquired during the melt season. *Remote sensing of environment*, *174*, pp.314-328.

Clague, J.J. and Evans, S.G., 2000. A review of catastrophic drainage of moraine-dammed lakes in British Columbia. *Quaternary Science Reviews*, *19*(17-18), pp.1763-1783.

Clarke, G.K., Anslow, F.S., Jarosch, A.H., Radić, V., Menounos, B., Bolch, T. and Berthier, E., 2013. Ice volume and subglacial topography for western Canadian glaciers from mass balance fields, thinning rates, and a bed stress model. *Journal of Climate*, *26*(12), pp.4282-4303.

Clarke, G.K., Berthier, E., Schoof, C.G. and Jarosch, A.H., 2009. Neural networks applied to estimating subglacial topography and glacier volume. *Journal of Climate*, *22*(8), pp.2146-2160.

Chae, S.H., Lee, W.J., Jung, H.S. and Zhang, L., 2017. Ionospheric correction of L-band SAR offset measurements for the precise observation of glacier velocity variations on Novaya Zemlya. *IEEE Journal of Selected Topics in Applied Earth Observations and Remote Sensing*, *10*(8), pp.3591-3603.

Chandler, D., Hubbard, B., Hubbard, A., Murray, T. and Rippin, D., 2008. Optimising ice flow law parameters using borehole deformation measurements and numerical modelling. Geophysical Research Letters, 35(12).

Chen, W., Zhang, K. and Liu, Q., 2016. Robust visual tracking via patch based kernel correlation filters with adaptive multiple feature ensemble. Neurocomputing, 214, pp.607-617.

Ciappa, A., Pietranera, L. and Battazza, F., 2010. Perito Moreno Glacier (Argentina) flow estimation by COSMO SkyMed sequence of high-resolution SAR-X imagery. *Remote Sensing of Environment*, *114*(9), pp.2088-2096.

Cuffey, K.M. and Paterson, W.S.B., 2010. *The physics of glaciers*. Academic Press.

De Paoli, L. and Flowers, G.E., 2009. Dynamics of a small surge-type glacier using one-dimensional geophysical inversion. *Journal of Glaciology*, *55*(194), pp.1101-1112.

Debella-Gilo, M. and Kääb, A., 2010, May. Sub-pixel precision algorithms for normalised cross-correlation based image matching of mass movements. In *EGU General Assembly Conference Abstracts* (p. 520).

Debella-Gilo, M. and Kääb, A., 2012. Measurement of surface displacement and deformation of mass movements using least squares matching of repeat high resolution satellite and aerial images. *Remote sensing*, *4*(1), pp.43-67.

Definiens Developer 7 Reference Book, pp. 15-24, 2007.

Degenhardt Jr, J.J., 2009. Development of tongue-shaped and multilobate rock glaciers in alpine environments–Interpretations from ground penetrating radar surveys. *Geomorphology*, *109*(3-4), pp.94-107.

Deledalle, C.A., Nicolas, J.M., Tupin, F., Denis, L., Fallourd, R. and Trouvé, E., 2010, July. Glaciermonitoring: Correlation versus texture tracking. In *2010 IEEE International Geoscience and Remote Sensing Symposium* (pp. 513-516). IEEE.

Denis, M., Guiraud, M., Konaté, M. and Buoncristiani, J.F., 2010. Subglacial deformation and water-pressure cycles as a key for understanding ice stream dynamics: evidence from the Late Ordovician succession of the Djado Basin (Niger). *International Journal of Earth Sciences*, *99*(6), pp.1399-1425.

Derauw, D., 1999, November. DInSAR and coherence tracking applied to glaciology: The example of Shirase Glacier. In *Proc. FRINGE* (Vol. 99).

Drăguţ, L., Tiede, D. and Levick, S.R., 2010. ESP: a tool to estimate scale parameter for multiresolution image segmentation of remotely sensed data. International Journal of Geographical Information Science, 24(6), pp.859-871.

Duan, Q., Sorooshian, S. and Gupta, V., 1992. Effective and efficient global optimization for conceptual rainfall-runoff models. *Water resources research*, *28*(4), pp.1015-1031.

Duan, K., Yao, T., Wang, N. and Liu, H., 2012. Numerical simulation of Urumqi Glacier No. 1 in the eastern Tianshan, central Asia from 2005 to 2070. *Chinese Science Bulletin*, *57*(34), pp.4505-4509.

Dunse, T., Greve, R., Schuler, T.V. and Hagen, J.O., 2011. Permanent fast flow versus cyclic surge behaviour: numerical simulations of the Austfonna ice cap, Svalbard. *Journal of Glaciology*, *57*(202), pp.247-259.

Durham, W.B., Kirby, S.H. and Stern, L.A., 1997. Creep of water ices at planetary conditions: A compilation. Journal of Geophysical Research: Planets, 102(E7), pp.16293-16302.

Duval, P., 1977. The role of the water content on the creep rate of polycrystalline ice. *IAHS Publ*, *118*, pp.29-33.

Euillades, L.D., Euillades, P.A., Riveros, N.C., Masiokas, M.H., Ruiz, L., Pitte, P., Elefante, S., Casu, F. and Balbarani, S., 2016. Detection of glaciers displacement time-series using SAR. *Remote sensing of Environment*, *184*, pp.188-198.

Erten, E., Reigber, A., Hellwich, O. and Prats, P., 2009. Glacier velocity monitoring by maximum likelihood texture tracking. *IEEE Transactions on Geoscience and Remote Sensing*, *47*(2), pp.394-405.

Evans, S.G. and Clague, J.J., 1994. Recent climatic change and catastrophic geomorphic processes in mountain environments. In *Geomorphology and Natural Hazards* (pp. 107-128). Elsevier.

Fahnestock, M., Scambos, T., Moon, T., Gardner, A., Haran, T. and Klinger, M., 2016. Rapid large-area mapping of ice flow using Landsat 8. *Remote Sensing of Environment*, *185*, pp.84-94.

Farinotti, D., Brinkerhoff, D.J., Fürst, J.J., Gantayat, P., Gillet-Chaulet, F., Huss, M., Leclercq, P.W., Maurer, H., Morlighem, M., Pandit, A. and Rabatel, A., 2020. Results from the Ice Thickness Models Intercomparison eXperiment phase 2 (ITMIX2). *Frontiers in Earth Science*, *8*, p.484.

Farinotti, D., Huss, M., Bauder, A., Funk, M. and Truffer, M., 2009. A method to estimate the ice volume and ice-thickness distribution of alpine glaciers. *Journal of Glaciology*, *55*(191), pp.422-430.

Farinotti, D., Brinkerhoff, D.J., Clarke, G.K., Fürst, J.J., Frey, H., Gantayat, P., Gillet-Chaulet, F., Girard, C., Huss, M., Leclercq, P.W. and Linsbauer, A., 2017. How accurate are estimates of glacier ice thickness? Results from ITMIX, the Ice Thickness Models Intercomparison eXperiment. *The Cryosphere*, *11*(2), pp.949-970.

Farinotti, D., Huss, M., Fürst, J.J., Landmann, J., Machguth, H., Maussion, F. and Pandit, A., 2019. A consensus estimate for the ice thickness distribution of all glaciers on Earth. *Nature Geoscience*, *12*(3), pp.168-173.

Fastook, J.L., Brecher, H.H. and Hughes, T.J., 1995. Derived bedrock elevations, strain rates and stresses from measured surface elevations and velocities: Jakobshavns Isbræ, Greenland. *Journal of Glaciology*, *41*(137), pp.161-173.

Feiger, N., Huss, M., Leinss, S., Sold, L. and Farinotti, D., 2018. The bedrock topography of Gries-and Findelengletscher. *Geographica Helvetica*, *73*(1), pp.1-9.

Fischer, A., 2009. Calculation of glacier volume from sparse ice-thickness data, applied to Schaufelferner, Austria. *Journal of Glaciology*, *55*(191), pp.453-460.

Fitch, A.J., Kadyrov, A., Christmas, W.J. and Kittler, J., 2002, September. Orientation Correlation. In *BMVC* (pp. 1-10).

Flowers, G.E., Roux, N., Pimentel, S. and Schoof, C.G., 2011. Present dynamics and future prognosis of a slowly surging glacier. *The Cryosphere*, *5*(1), pp.299-313.

Frey, H., Huggel, C., Chisolm, R.E., Baer, P., McArdell, B., Cochachin, A. and Portocarrero, C., 2018. Multi-source glacial lake outburst flood hazard assessment and mapping for Huaraz, Cordillera Blanca, Peru. *Frontiers in Earth Science*, *6*, p.210.

Frey, H., Haeberli, W., Linsbauer, A., Huggel, C. and Paul, F., 2010. A multi-level strategy for anticipating future glacier lake formation and associated hazard potentials. *Natural Hazards and Earth System Sciences*, *10*(2), pp.339-352.

Frey, H., Machguth, H., Huss, M., Huggel, C., Bajracharya, S., Bolch, T., Kulkarni, A., Linsbauer, A., Salzmann, N. and Stoffel, M., 2014. Estimating the volume of glaciers in the Himalayan–Karakoram region using different methods. *The Cryosphere*, 8(6), pp.2313-2333.

Fürst, J.J., Gillet-Chaulet, F., Benham, T.J., Dowdeswell, J.A., Grabiec, M., Navarro, F., Pettersson, R., Moholdt, G., Nuth, C., Sass, B. and Aas, K., 2017. Application of a two-step approach for mapping ice thickness to various glacier types on Svalbard. *The Cryosphere*, *11*(5), pp.2003-2032.

Fürst, J.J., Rybak, O., Goelzer, H., Smedt, B.D., Groen, P.D. and Huybrechts, P., 2011. Improved convergence and stability properties in a three-dimensional higher-order ice sheet model. Geoscientific Model Development, 4(4), pp.1133-1149.

Gabbi, J., Farinotti, D., Bauder, A. and Maurer, H., 2012. Ice volume distribution and implications on runoff projections in a glacierized catchment. *Hydrology and Earth System Sciences*, *16*(12), pp.4543-4556.

Gantayat, P., Kulkarni, A.V. and Srinivasan, J., 2014. Estimation of ice thickness using surface velocities and slope: case study at Gangotri Glacier, India. *Journal of Glaciology*, *60*(220), pp.277-282.

Gantayat, P., Kulkarni, A.V., Srinivasan, J. and Schmeits, M.J., 2017. Numerical modelling of past retreat and future evolution of Chhota Shigri glacier in Western Indian Himalaya. *Annals of Glaciology*, *58*(75pt2), pp.136-144.

Gärtner-Roer, I., Naegeli, K., Huss, M., Knecht, T., Machguth, H. and Zemp, M., 2014. A database of worldwide glacier thickness observations. *Global and Planetary Change*, *122*, pp.330-344.

Gagliardini, O., Zwinger, T., Gillet-Chaulet, F., Durand, G., Favier, L., Fleurian, B.D., Greve, R., Malinen, M., Martín, C., Råback, P. and Ruokolainen, J., 2013. Capabilities and performance of Elmer/Ice, a new-generation ice sheet model. *Geoscientific Model Development*, *6*(4), pp.1299-1318.

Gergan, J.T., Dobhal, D.P. and Kaushik, R., 1999. Ground penetrating radar ice thickness measurements of Dokriani bamak (glacier), Garhwal Himalaya. *Current Science*, pp.169-173.

Glen, J.W., 1952. Experiments on the deformation of ice. *Journal of Glaciology*, *2*(12), pp.111-114.

Glen, J.W., 1955. The creep of polycrystalline ice. *Proceedings of the Royal Society of London. Series A. Mathematical and Physical Sciences*, *228*(1175), pp.519-538.

Glen, J.W., 1958. The flow law of ice: A discussion of the assumptions made in glacier theory, their experimental foundations and consequences. *IASH Publ*, *47*(171), p.e183.

Goldsby, D.L. and Kohlstedt, D.L., 2001. Superplastic deformation of ice: Experimental observations. *Journal of Geophysical Research: Solid Earth*, *106*(B6), pp.11017-11030.

Gourlet, P., Rignot, E., Rivera, A. and Casassa, G., 2016. Ice thickness of the northern half of the Patagonia Icefields of South America from high‐resolution airborne gravity surveys. *Geophysical Research Letters*, *43*(1), pp.241-249.

Gresho, P.M. and Sani, R.L., 2000. Incompressible flow and the finite element method. Volume 1: Advection-diffusion and isothermal laminar flow.

Haeberli, W. and Hölzle, M., 1995. Application of inventory data for estimating characteristics of and regional climate-change effects on mountain glaciers: a pilot study with the European Alps. *Annals of glaciology*, *21*, pp.206-212.

Hagg, W., Mayer, C., Lambrecht, A., Kriegel, D. and Azizov, E., 2013. Glacier changes in the big Naryn basin, Central Tian Shan. *Global and Planetary Change*, *110*, pp.40-50.

Haq, M.A., Jain, K. and Menon, K.P.R., 2014. Modelling of Gangotri glacier thickness and volume using an artificial neural network. *International Journal of Remote Sensing*, *35*(16), pp.6035-6042.

Haug, T., Kääb, A. and Skvarca, P., 2010. Monitoring ice shelf velocities from repeat MODIS and Landsat data–a method study on the Larsen C ice shelf, Antarctic Peninsula, and 10 other ice shelves around Antarctica. *The Cryosphere*, *4*(2), pp.161-178.

Heid, T., 2011. Deriving glacier surface velocities from repeat optical images.

Heid, T. and Kääb, A., 2012. Evaluation of existing image matching methods for deriving glacier surface displacements globally from optical satellite imagery. *Remote Sensing of Environment*, *118*, pp.339-355.

Helfricht, K., Huss, M., Fischer, A. and Otto, J.C., 2019. Calibrated ice thickness estimate for all glaciers in Austria. *Frontiers in Earth Science*, *7*, p.68.

Helton, J.C., Johnson, J.D., Oberkampf, W.L. and Sallaberry, C.J., 2010. Representation of analysis results involving aleatory and epistemic uncertainty. International Journal of General Systems, 39(6), pp.605-646.

Herman, F., Anderson, B. and Leprince, S., 2011. Mountain glacier velocity variation during a retreat/advance cycle quantified using sub-pixel analysis of ASTER images. *Journal of Glaciology*, *57*(202), pp.197-207.

Hooke, R.LeB. 2005. *Principles of glacier mechanics*. Second edition. Cambridge, etc., Cambridge University Press.

Huang, L. and Li, Z., 2011. Comparison of SAR and optical data in deriving glacier velocity with feature tracking. *International journal of remote sensing*, *32*(10), pp.2681-2698.

Huss, M., Farinotti, D., Bauder, A. and Funk, M., 2008. Modelling runoff from highly glacierized alpine drainage basins in a changing climate. *Hydrological processes*, *22*(19), pp.3888-3902.

Huss, M. and Hock, R., 2015. A new model for global glacier change and sea-level rise. *Frontiers in Earth Science*, *3*, p.54. Huss, M. and Farinotti, D., 2012. Distributed ice thickness and volume of all glaciers around the globe. *Journal of Geophysical Research: Earth Surface*, 117(F4).

Hindmarsh, R.C.A., 2004. A numerical comparison of approximations to the Stokes equations used in ice sheet and glacier modeling. *Journal of Geophysical Research: Earth Surface*, *109*(F1).

Hutchinson, M.F., 1989. A new procedure for gridding elevation and stream line data with automatic removal of spurious pits. *Journal of hydrology*, *106*(3-4), pp.211-232.

IPCC, 2014. Climate Change 2014: Synthesis Report. Contribution of Working Groups I, II and III to the Fifth Assessment Report of the Intergovernmental Panel on Climate Change [Core Writing Team, R.K. Pachauri and L.A. Meyer (eds.)]. IPCC, Geneva, Switzerland,151.Available at https://www.ipcc.ch/pdf/assessmentreport/ar5/syr/AR5_SYR_FINAL_SPM.pdf. Accessed 17 December 2017.

Isaac, T., Petra, N., Stadler, G. and Ghattas, O., 2015. Scalable and efficient algorithms for the propagation of uncertainty from data through inference to prediction for large-scale problems, with application to flow of the Antarctic ice sheet. Journal of Computational Physics, 296, pp.348-368.

Jacka, T.H. and Budd, W.F., 1989. Isotropic and anisotropic flow relations for ice dynamics. *Annals of glaciology*, *12*, pp.81-84.

Johnson, P.G. and Kasper, J.N., 1992. The development of an ice-dammed lake: The contemporary and older sedimentary record. *Arctic and Alpine Research*, *24*(4), pp.304-313.

Jarosch, A.H., Schoof, C.G. and Anslow, F.S., 2013. Restoring mass conservation to shallow ice flow models over complex terrain. *The Cryosphere*, *7*(1), pp.229-240.

Joughin, I., Smith, B.E. and Holland, D.M., 2010. Sensitivity of 21st century sea level to ocean-induced thinning of Pine Island Glacier, Antarctica. *Geophysical Research Letters*, *37*(20).

Jouvet, G., Huss, M., Blatter, H., Picasso, M. and Rappaz, J., 2009. Numerical simulation of Rhonegletscher from 1874 to 2100. *Journal of Computational Physics*, *228*(17), pp.6426-6439.

Jouvet, G., Huss, M., Funk, M. and Blatter, H., 2011. Modelling the retreat of Grosser Aletschgletscher, Switzerland, in a changing climate. *Journal of Glaciology*, *57*(206), pp.1033-1045.

Kääb, A., Huggel, C., Paul, F., Wessels, R., Raup, B., Kieffer, H. and Kargel, J., 2002, March. Glacier monitoring from ASTER imagery: accuracy and applications. In *Proceedings of EARSeL-LISSIG-workshop observing our cryosphere from space* (Vol. 2, pp. 43-53).

Kanade, T. and Okutomi, M., 1994. A stereo matching algorithm with an adaptive window: Theory and experiment. IEEE transactions on pattern analysis and machine intelligence, 16(9), pp.920-932.

Kumar, A., Negi, H.S., Kumar, K., Kanda, N., Singh, K.K., Pandit, A. and Ramsankaran, R., 2020. Estimation of recent changes in thickness and mass balance of the Patsio glacier in the Great Himalayan region using geodetic technique and ancillary data. *Geocarto International*, *35*(1), pp.47-63.

Kumar, V., Venkataramana, G. and Høgda, K.A., 2011. Glacier surface velocity estimation using SAR interferometry technique applying ascending and descending passes in Himalayas. *International Journal of Applied Earth Observation and Geoinformation*, *13*(4), pp.545-551.

Lambeck, K., Rouby, H., Purcell, A., Sun, Y. and Sambridge, M., 2014. Sea level and global ice volumes from the Last Glacial Maximum to the Holocene. Proceedings of the National Academy of Sciences, 111(43), pp.15296-15303.

Lapazaran, J.J., Otero, J., Martín-Español, A. and Navarro, F.J., 2016. On the errors involved in ice-thickness estimates I: ground-penetrating radar measurement errors. *Journal of Glaciology*, *62*(236), pp.1008-1020.

Leclercq, P.W., Weidick, A., Paul, F., Bolch, T., Citterio, M. and Oerlemans, J., 2012. Brief communication" Historical glacier length changes in West Greenland". *The Cryosphere*, *6*(6), pp.1339-1343.

Le Meur, E., Gerbaux, M., Schäfer, M. and Vincent, C., 2007. Disappearance of an Alpine glacier over the 21st Century simulated from modeling its future surface mass balance. *Earth and Planetary Science Letters*, *261*(3-4), pp.367-374.

Le Meur, E. and Vincent, C., 2003. A two-dimensional shallow ice-flow model of Glacier de Saint-Sorlin, France. *Journal of Glaciology*, *49*(167), pp.527-538.

Li, H., Ng, F., Li, Z., Qin, D. and Cheng, G., 2012. An extended “perfect-plasticity” method for estimating ice thickness along the flow line of mountain glaciers. *Journal of Geophysical Research: Earth Surface*, *117*(F1).

Li, S., Leinss, S. and Hajnsek, I., 2021. Cross-Correlation Stacking for Robust Offset Tracking Using SAR Image Time-Series. *IEEE Journal of Selected Topics in Applied Earth Observations and Remote Sensing*, 14, pp.4765-4778.

Linsbauer, A., Paul, F. and Haeberli, W., 2012. Modeling glacier thickness distribution and bed topography over entire mountain ranges with GlabTop: Application of a fast and robust approach. *Journal of Geophysical Research: Earth Surface*, *117*(F3).

Linsbauer, A., Frey, H., Haeberli, W., Machguth, H., Azam, M.F. and Allen, S., 2016. Modelling glacier-bed overdeepenings and possible future lakes for the glaciers in the Himalaya—Karakoram region. *Annals of Glaciology*, *57*(71), pp.119-130.

Linsbauer, A., Paul, F., Hoelzle, M., Frey, H., Haeberli, W. and Purves, R.S., 2009. The Swiss Alps without glaciers–a GIS-based modelling approach for reconstruction of glacier beds.

Linsbauer, A., Paul, F. and Haeberli, W., 2012. Modeling glacier thickness distribution and bed topography over entire mountain ranges with GlabTop: Application of a fast and robust approach. *Journal of Geophysical Research: Earth Surface*, *117*(F3).

Liu, Y. and Gupta, H.V., 2007. Uncertainty in hydrologic modeling: Toward an integrated data assimilation framework. *Water resources research*, 43(7).

Lliboutry, L., Arnao, B.M., Pautre, A. and Schneider, B., 1977. Glaciological problems set by the control of dangerous lakes in Cordillera Blanca, Peru. I. Historical failures of morainic dams, their causes and prevention. *Journal of Glaciology*, *18*(79), pp.239-254.

MacDougall, A.H., 2010. *Distributed energy-balance glacier melt-modelling in the Donjek Range of the St. Elias Mountains, Yukon Territory, Canada: Model transferability in space and time* (Doctoral dissertation, Science: Department of Earth Sciences).

MacAyeal, D.R., 1989. Large-scale ice flow over a viscous basal sediment: Theory and application to ice stream B, Antarctica. *Journal of Geophysical Research: Solid Earth*, *94*(B4), pp.4071-4087.

Maisch, M. and Haeberli, W., 1982. Interpretation geometrischer Parameter von Spätglazialgletschern im Gebiet Mittelbünden, Schweizer Alpen. *Beiträge zur Quartärforschung in der Schweiz. Zürich, Geographisches Institut der Universität*, pp.111-126.

Martín-Español, Alba, Andrew Zammit-Mangion, Peter J. Clarke, Thomas Flament, Veit Helm, Matt A. King, Scott B. Luthcke et al. "Spatial and temporal Antarctic Ice Sheet mass trends, glacio-isostatic adjustment, and surface processes from a joint inversion of satellite altimeter, gravity, and GPS data." *Journal of Geophysical Research: Earth Surface* 121, no. 2 (2016): 182-200.

Maussion, F., Butenko, A., Champollion, N., Dusch, M., Eis, J., Fourteau, K., Gregor, P., Jarosch, A.H., Landmann, J., Oesterle, F. and Recinos, B., 2019. The open global glacier model (OGGM) v1. 1. Geoscientific Model Development, 12(3), pp.909-931.

McNabb, R.W., Hock, R., O'Neel, S., Rasmussen, L.A., Ahn, Y., Braun, M., Conway, H., Herreid, S., Joughin, I., Pfeffer, W.T. and Smith, B.E., 2012. Using surface velocities to calculate ice thickness and bed topography: a case study at Columbia Glacier, Alaska, USA. *Journal of Glaciology*, *58*(212), pp.1151-1164.

Messerli, A. and Grinsted, A., 2015. Image georectification and feature tracking toolbox: ImGRAFT. *Geoscientific Instrumentation, Methods and Data Systems*, *4*(1), pp.23-34.

Michel, L., Picasso, M., Farinotti, D., Bauder, A., Funk, M. and Blatter, H., 2013. Estimating the ice thickness of mountain glaciers with an inverse approach using surface topography and mass-balance. *Inverse Problems*, *29*(3), p.035002.

Michel, L., Picasso, M., Farinotti, D., Funk, M. and Blatter, H., 2014. Estimating the ice thickness of shallow glaciers from surface topography and mass-balance data with a shape optimization algorithm. *Computers & Geosciences*, *66*, pp.182-199.

Mishra, A., Negi, B.D.S., Banerjee, A., Nainwal, H.C. and Shankar, R., 2018. Estimation of ice thickness of the Satopanth Glacier, Central Himalaya using ground penetrating radar. *CURRENT SCIENCE*, *114*(4), p.785.

Möller, M., Obleitner, F., Reijmer, C.H., Pohjola, V.A., Głowacki, P. and Kohler, J., 2016. Adjustment of regional climate model output for modeling the climatic mass balance of all glaciers on Svalbard. *Journal of Geophysical Research: Atmospheres*, *121*(10), pp.5411-5429.

Morlighem, M., Rignot, E., Seroussi, H., Larour, E., Ben Dhia, H. and Aubry, D., 2010. Spatial patterns of basal drag inferred using control methods from a full-Stokes and simpler models for Pine Island Glacier, West Antarctica. *Geophysical Research Letters*, *37*(14).

Morlighem, M., Rignot, E., Seroussi, H., Larour, E., Ben Dhia, H. and Aubry, D., 2011. A mass conservation approach for mapping glacier ice thickness. *Geophysical Research Letters*, *38*(19).

Mosbeux, C., Gillet-Chaulet, F. and Gagliardini, O., 2016. Comparison of adjoint and nudging methods to initialise ice sheet model basal conditions. *Geoscientific Model Development*, *9*(7), pp.2549-2562.

Nagler, T., Rott, H., Hetzenecker, M., Wuite, J. and Potin, P., 2015. The Sentinel-1 mission: New opportunities for ice sheet observations. *Remote Sensing*, *7*(7), pp.9371-9389.

Nakamura, K., Doi, K. and Shibuya, K., 2007. Estimation of seasonal changes in the flow of Shirase Glacier using JERS-1/SAR image correlation. *Polar Science*, *1*(2-4), pp.73-83.

Navarro, F.J., Martín-Español, A., Lapazaran, J.J., Grabiec, M., Otero, J., Vasilenko, E.V. and Puczko, D., 2014. Ice volume estimates from ground-penetrating radar surveys, Wedel Jarlsberg Land glaciers, Svalbard. *Arctic, Antarctic, and Alpine Research*, *46*(2), pp.394-406.

Nearing, M.A., Ascough, L.D. and Chaves, H.M.L., 1989. WEPP model sensitivity analysis. Water erosion prediction project landscape profi le model documentation. NSERL Report, (2).

Nelder, J.A. and Mead, R., 1965. A simplex method for function minimization. *The computer journal*, *7*(4), pp.308-313.

Nicoll, J.B. and Meyer, F.J., 2008, July. Mapping the ionosphere using L-band SAR data. In *IGARSS 2008-2008 IEEE International Geoscience and Remote Sensing Symposium* (Vol. 2, pp. II-537). IEEE.

Nitti, D.O., Hanssen, R.F., Refice, A., Bovenga, F. and Nutricato, R., 2010. Impact of DEM-assisted coregistration on high-resolution SAR interferometry. *IEEE Transactions on Geoscience and Remote Sensing*, *49*(3), pp.1127-1143.

Nye, J.F., 1952. The mechanics of glacier flow. *Journal of Glaciology*, *2*(12), pp.82-93.

Nye, J.F., 1965. The flow of a glacier in a channel of rectangular, elliptic or parabolic cross-section. *Journal of glaciology*, *5*(41), pp.661-690.

O'Connor, J.E. and Costa, J.E., 1993. Geologic and hydrologic hazards in glacierized basins in North America resulting from 19th and 20th century global warming. *Natural Hazards*, *8*(2), pp.121-140.

Oerlemans, J., 2001. *Glaciers and climate change*. CRC Press.

Palmer, S., Shepherd, A., Nienow, P. and Joughin, I., 2011. Seasonal speedup of the Greenland Ice Sheet linked to routing of surface water. *Earth and Planetary Science Letters*, *302*(3-4), pp.423-428.

Patel, L., Sharma, P. and Thamban, M., 2019. Spatio-temporal variability of snow water equivalent over the Vestre Broggerbreen and Feiringbreen glaciers, Ny-Ålesund, Svalbard. *Journal of Earth System Science*, *128*(7), pp.1-15.

Pattyn, F., 2003. A new three-dimensional higher-order thermomechanical ice sheet model: Basic sensitivity, ice stream development, and ice flow across subglacial lakes. *Journal of Geophysical Research: Solid Earth*, *108*(B8).

Pattyn, F., Delcourt, C., Samyn, D., De Smedt, B. and Nolan, M., 2009. Bed properties and hydrological conditions underneath McCall Glacier, Alaska, USA. *Annals of glaciology*, *50*(51), pp.80-84

Paul, F., Bolch, T., Briggs, K., Kääb, A., McMillan, M., McNabb, R., Nagler, T., Nuth, C., Rastner, P., Strozzi, T. and Wuite, J., 2017. Error sources and guidelines for quality assessment of glacier area, elevation change, and velocity products derived from satellite data in the Glaciers_cci project. *Remote Sensing of Environment*, *203*, pp.256-275.

Paul, F., Bolch, T., Kääb, A., Nagler, T., Nuth, C., Scharrer, K., Shepherd, A., Strozzi, T., Ticconi, F., Bhambri, R. and Berthier, E., 2015. The glaciers climate change initiative: Methods for creating glacier area, elevation change and velocity products. *Remote Sensing of Environment*, *162*, pp.408-426.

Paul, F. and Linsbauer, A., 2011. Modeling of glacier bed topography from glacier outlines, 845 central branch lines, and a DEM. *Int. J. Geogr. Inform. Sci., doi*, *10*(13658816.2011), p.846.

Pfeffer, W.T., Arendt, A.A., Bliss, A., Bolch, T., Cogley, J.G., Gardner, A.S., Hagen, J.O., Hock, R., Kaser, G., Kienholz, C. and Miles, E.S., 2014. The Randolph Glacier Inventory: a globally complete inventory of glaciers. *Journal of glaciology*, *60*(221), pp.537-552.

Popov, N., 1997, August. Glacial debris-flows mitigation in Kazakstan: assessment, prediction and control. In *Debris-Flow Hazards Mitigation: Mechanics, Prediction, and Assessment* (pp. 113-122). ASCE.

Pralong, M.R. and Gudmundsson, G.H., 2011. Bayesian estimation of basal conditions on Rutford Ice Stream, West Antarctica, from surface data. *Journal of Glaciology*, *57*(202), pp.315-324.

Pritchard, H., Murray, T., Luckman, A., Strozzi, T. and Barr, S., 2005. Glacier surge dynamics of Sortebræ, east Greenland, from synthetic aperture radar feature tracking. *Journal of Geophysical Research: Earth Surface*, *110*(F3).

Purdie, H., Anderson, B., Mackintosh, A. and Lawson, W., 2018. Revisiting glaciological measurements on Haupapa/Tasman Glacier, New Zealand, in a contemporary context. *Geografiska Annaler: Series A, Physical Geography*, *100*(4), pp.351-369.

Rabatel, A., Sanchez, O., Vincent, C. and Six, D., 2018. Estimation of glacier thickness from surface mass balance and ice flow velocities: a case study on Argentière Glacier, France. *Frontiers in Earth Science*, 6, p.112.

Ramsankaran, R.A.A.J., Pandit, A. and Azam, M.F., 2018. Spatially distributed ice-thickness modelling for Chhota Shigri Glacier in western Himalayas, India. *International Journal of Remote Sensing*, *39*(10), pp.3320-3343.

Rasmussen, L.A., 1988. Bed topography and mass-balance distribution of Columbia Glacier, Alaska, USA, determined from sequential aerial photography. *Journal of Glaciology*, *34*(117), pp.208-216.

Raymond, C.F. and Colbeck, S.C., 1980. Temperate valley glaciers. Dynamics of snow and ice masses, pp.79-139.

Ren, D. and Leslie, L.M., 2011. Three positive feedback mechanisms for ice-sheet melting in a warming climate. *Journal of Glaciology*, *57*(206), pp.1057-1066.

Reynolds, J.M., 1992. The identification and mitigation of glacier-related hazards: examples from the Cordillera Blanca, Peru. In *Geohazards* (pp. 143-157). Springer, Dordrecht.

Richardson, S.D. and Reynolds, J.M., 2000. An overview of glacial hazards in the Himalayas. *Quaternary International*, *65*, pp.31-47.

Rignot, E., Echelmeyer, K. and Krabill, W., 2001. Penetration depth of interferometric synthetic-aperture radar signals in snow and ice. *Geophysical Research Letters*, *28*(18), pp.3501-3504.

Rigsby, G.P., 1958, September. Fabrics of glacier and laboratory deformed ice. In *Symposium on Physics of the Movement of the Ice, Symposium of Chamonix* (pp. 16-24).

Riveros, N., Euillades, L., Euillades, P., Moreiras, S. and Balbarani, S., 2013. Offset tracking procedure applied to high resolution SAR data on Viedma Glacier, Patagonian Andes, Argentina. *Advances in Geosciences*, *35*, pp.7-13.

Ruan, Z., Guo, H., Liu, H. and Yan, S., 2013. Glacier surface velocity estimation in the West Kunlun Mountain range from L-band ALOS/PALSAR images using modified synthetic aperture radar offset-tracking procedure. *Journal of Applied Remote Sensing*, 8(1), p.084595.

Saintenoy, A., Friedt, J.M., Booth, A.D., Tolle, F., Bernard, E., Laffly, D., Marlin, C. and Griselin, M., 2013. Deriving ice thickness, glacier volume and bedrock morphology of Austre Lovénbreen (Svalbard) using GPR. *Near Surface Geophysics*, *11*(2), pp.253-262.

Sattar, A., Goswami, A., Kulkarni, A.V. and Das, P., 2019. Glacier-surface velocity derived ice volume and retreat assessment in the dhauliganga basin, central himalaya–A remote sensing and modeling based approach. *Frontiers in Earth Science*, *7*, p.105.

Sánchez-Gámez, P. and Navarro, F.J., 2017. Glacier surface velocity retrieval using D-InSAR and offset tracking techniques applied to ascending and descending passes of Sentinel-1 data for southern Ellesmere ice caps, Canadian Arctic. *Remote Sensing*, *9*(5), p.442.

Savage, J.C. and Paterson, W.S.B., 1963. Borehole measurements in the Athabasca Glacier. *Journal of Geophysical Research*, *68*(15), pp.4521-4536.

Scherler, D., Leprince, S. and Strecker, M.R., 2008. Glacier-surface velocities in alpine terrain from optical satellite imagery—Accuracy improvement and quality assessment. *Remote Sensing of Environment*, *112*(10), pp.3806-3819.

Schiefer, E., Menounos, B. and Wheate, R., 2007. Recent volume loss of British Columbian glaciers, Canada. *Geophysical Research Letters*, *34*(16).

Schubert, A., Faes, A., Kääb, A. and Meier, E., 2013. Glacier surface velocity estimation using repeat TerraSAR-X images: Wavelet-vs. correlation-based image matching. *ISPRS Journal of Photogrammetry and Remote Sensing*, *82*, pp.49-62.

Short, N.H. and Gray, A.L., 2005. Glacier dynamics in the Canadian High Arctic from RADARSAT-1 speckle tracking. *Canadian Journal of Remote Sensing*, *31*(3), pp.225-239.

Singh, K.K., Negi, H.S., Gusain, H.S., Ganju, A., Singh, D.K. and Kulkarni, A.V., 2018. Temporal change and flow velocity estimation of Patseo glacier, Western Himalaya, India. *Current Science (00113891)*, *114*(4).

Singh, S.K., Rathore, B.P., Bahuguna, I.M., Ramnathan, A.L. and Ajai, 2012. Estimation of glacier ice thickness using Ground Penetrating Radar in the Himalayan region. *Current Science*, pp.68-73.

Strozzi, T., Luckman, A., Murray, T., Wegmuller, U. and Werner, C.L., 2002. Glacier motion estimation using SAR offset-tracking procedures. *IEEE Transactions on Geoscience and Remote Sensing*, *40*(11), pp.2384-2391.

Swain, A.K., Mukhtar, M.A., Majeed, Z. and Shukla, S.P., 2018. Depth profiling and recessional history of the Hamtah and Parang glaciers in Lahaul and Spiti, Himachal Pradesh, Indian Himalaya. *Geological Society, London, Special Publications*, *462*(1), pp.35-49.

Turrin, J., Forster, R.R., Larsen, C. and Sauber, J., 2013. The propagation of a surge front on Bering Glacier, Alaska, 2001–2011. *Annals of glaciology*, 54(63), pp.221-228.

Vallon, M., Petit, J.R. and Fabre, B., 1976. Study of an ice core to the bedrock in the accumulation zone of an alpine glacier. *Journal of Glaciology*, *17*(75), pp.13-28.

Van der Veen, C.J., 1987. Longitudinal stresses and basal sliding: a comparative study. In *Dynamics of the West Antarctic ice sheet* (pp. 223-248). Springer, Dordrecht.

Van Der Veen, C.J. and Whillans, I.M., 1989. Force budget: I. Theory and numerical methods. *Journal of glaciology*, *35*(119), pp.53-60.

Van Pelt, W.J.J., Oerlemans, J., Reijmer, C.H., Pettersson, R., Pohjola, V.A., Isaksson, E. and Divine, D., 2013. An iterative inverse method to estimate basal topography and initialize ice flow models. *The Cryosphere*, *7*(3), pp.987-1006.

Vaughan, D.G., Comiso, J.C., Allison, I., Carrasco, J., Kaser, G., Kwok, R., Mote, P., Murray, T., Paul, F., Ren, J. and Rignot, E., 2013. Observations: cryosphere. Climate change, 2103, pp.317-382.

Voytenko, D., Dixon, T.H., Werner, C., Gourmelen, N., Howat, I.M., Tinder, P.C. and Hooper, A., 2012, July. Monitoring a glacier in southeastern Iceland with the portable Terrestrial Radar Interferometer. In 2012 *IEEE International Geoscience and Remote Sensing Symposium* (pp. 3230-3232). IEEE.

Vuichard, D. and Zimmermann, M., 1987. The 1985 catastrophic drainage of a moraine-dammed lake, Khumbu Himal, Nepal: cause and consequences. *Mountain Research and Development*, pp.91-110.

Vuille, M., Carey, M., Huggel, C., Buytaert, W., Rabatel, A., Jacobsen, D., Soruco, A., Villacis, M., Yarleque, C., Timm, O.E. and Condom, T., 2018. Rapid decline of snow and ice in the tropical Andes–Impacts, uncertainties and challenges ahead. *Earth-Science Reviews, 176*, pp.195-213.

Waller, J.A., García-Pintado, J., Mason, D.C., Dance, S.L. and Nichols, N.K., 2018. Analysis of observation uncertainty for flood assimilation and forecasting. *Hydrol Earth Syst Sci*, 22, pp.3983-3992.

Wang, X., Ding, Y., Liu, S., Jiang, L., Wu, K., Jiang, Z. and Guo, W., 2013. Changes of glacial lakes and implications in Tian Shan, central Asia, based on remote sensing data from 1990 to 2010. *Environmental Research Letters*, *8*(4), p.044052.

Warner, R.C. and Budd, W.F., 2000. Derivation of ice thickness and bedrock topography in data-gap regions over Antarctica. *Annals of Glaciology*, *31*, pp.191-197.

Watson, M.I., 1995. *Geophysical and glaciological studies of the Tasman and Mueller Glaciers* (Doctoral dissertation, University of Auckland).

Weertman, J., 1964. The theory of glacier sliding. *Journal of Glaciology*, *5*(39), pp.287-303.

Weertman, J., 1973b. Creep of ice. In: Whalley, E., Jones, S.J., Gold, L.W. (Eds.), Physics and Chemistry of Ice, R. Soc. Can., Ottawa, 320–337.

Weertman, J., 1983. Creep deformation of ice. Ann. Rev. Earth Planet. Sci. 11, 215–240.

Wheler, B.A., 2009. *Glacier melt modelling in the Donjek Range, St. Elias Mountains, Yukon Territory* (Doctoral dissertation, Dept. of Earth Sciences-Simon Fraser University).

Wu, K., Liu, S., Zhu, Y., Liu, Q. and Jiang, Z., 2020. Dynamics of glacier surface velocity and ice thickness for maritime glaciers in the southeastern Tibetan Plateau. Journal of Hydrology, 590, p.125527.

Yamada, T., 1998. Glacier lake and its outburst flood in the Nepal Himalaya. Data Center for Glacier Research. *Japanese Society of Snow and ice. Monograph*, *1*, p.96.

Yan, S., Guo, H., Liu, G. and Ruan, Z., 2013. Mountain glacier displacement estimation using a DEM-assisted offset tracking method with ALOS/PALSAR data. *Remote sensing letters*, *4*(5), pp.494-503.

Yang, L., Zhao, C., Lu, Z., Yang, C. and Zhang, Q., 2020. Three-Dimensional Time Series Movement of the Cuolangma Glaciers, Southern Tibet with Sentinel-1 Imagery. *Remote Sensing*, 12(20), p.3466.

Yellala, A., Kumar, V. and Høgda, K.A., 2019. Bara Shigri and Chhota Shigri glacier velocity estimation in western Himalaya using Sentinel-1 SAR data. *International Journal of Remote Sensing*, *40*(15), pp.5861-5874.

Zagorodnov, V., Tyler, S., Holland, D., Stern, A., Thompson, L.G., Sladek, C., Kobs, S. and Nicolas, J.P., 2014. New technique for access-borehole drilling in shelf glaciers using lightweight drills. *Journal of Glaciology*, *60*(223), pp.935-944.

Zienkiewicz, O.C., 1971. The finite element methods in engineering science. McGraw-Hill.

Zekollari, H., Huybrechts, P., Fürst, J.J., Rybak, O. and Eisen, O., 2013. Calibration of a higher-order 3-D ice-flow model of the Morteratsch glacier complex, Engadin, Switzerland. *Annals of Glaciology*, *54*(63), pp.343-351.

Zhang, Z., Liu, S., Wei, J., Xu, J., Guo, W., Bao, W. and Jiang, Z., 2016. Mass change of glaciers in Muztag Ata–Kongur Tagh, Eastern Pamir, China from 1971/76 to 2013/14 as derived from remote sensing data. *PloS one*, *11*(1), p.e0147327.

Zhang, G., Yao, T., Xie, H., Kang, S. and Lei, Y., 2013. Increased mass over the Tibetan Plateau: From lakes or glaciers?. *Geophysical Research Letters*, *40*(10), pp.2125-2130.

Zhang, G., Zheng, G., Gao, Y., Xiang, Y., Lei, Y. and Li, J., 2017. Automated water classification in the Tibetan plateau using Chinese GF-1 WFV data. *Photogrammetric Engineering & Remote Sensing*, *83*(7), pp.509-519.

Zmitrowicz, A., 2003. Glaciers and laws of friction and sliding. *Acta mechanica*, *166*(1), pp.185-206.

Appendix-A1

Google earth imagery of Chhota Shigri glacier dated 10th October, 2010. The boxes show the sites receiving contribution from rock fall and/or avalanches.

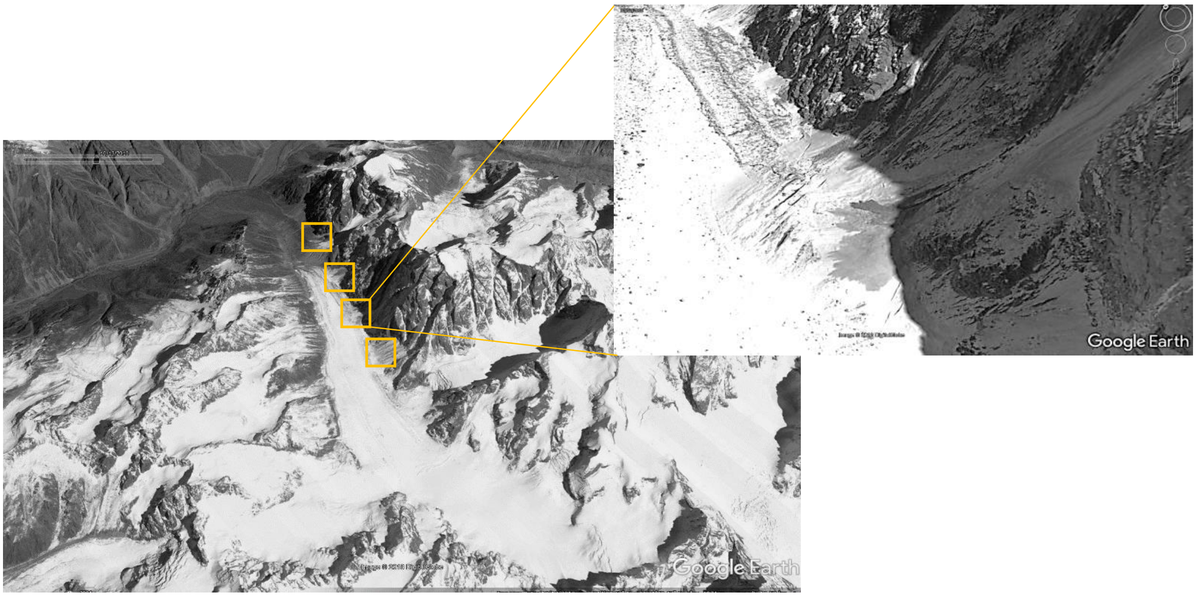

Appendix-A2

Window size distribution of South Glacier for period a. 2005-06 and b. 2014-15. Darker regions represent a smaller window size. Legend shows the window size in pixel x pixel.

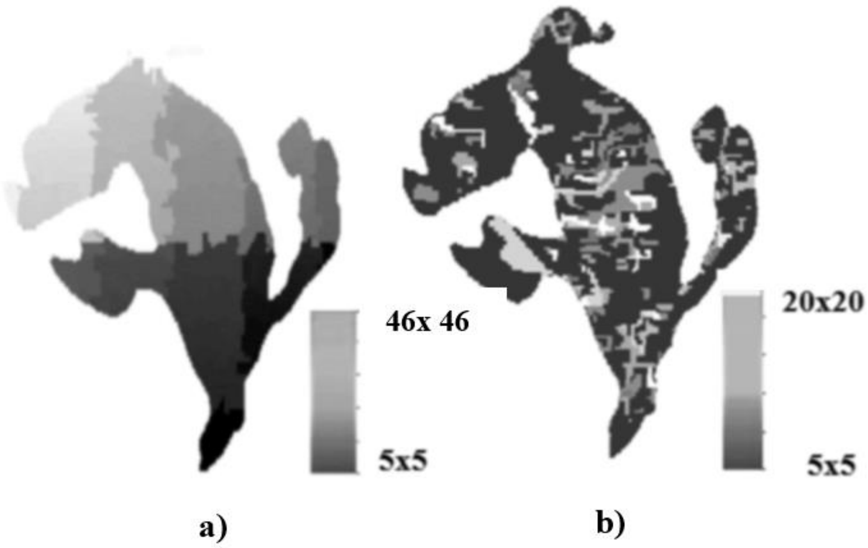

Appendix-A3

Window size distribution of South Glacier using optical imagery of a) Aug, 2013 and b) Nov, 2014.

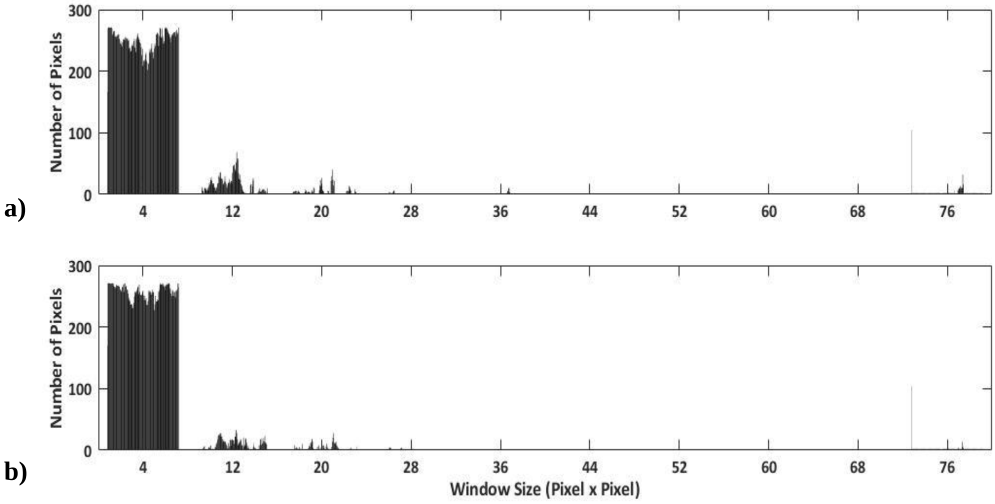

Appendix-A4

Comparative plot of proposed velocity estimates and cross correlation based velocity estimates (at standard window sizes of 32 x32, 64 x 64 and 128 x 128 pixels) of study glaciers: a) South Glacier for period 2005-06, b) Chhota Shigri Glacier for period 2009-10, and c) Tasman Glacier for period 2007-08.

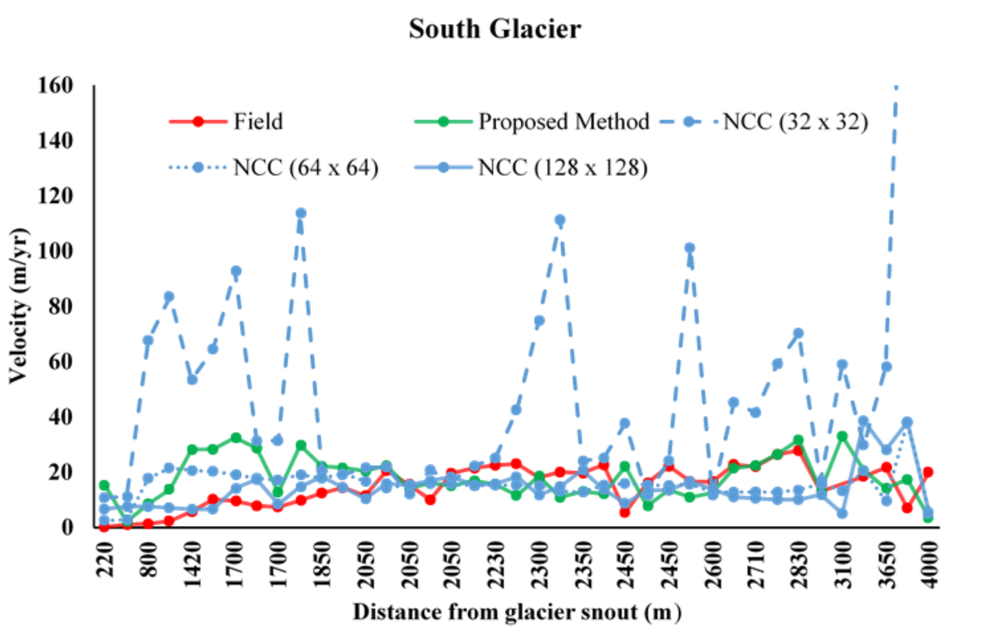

a)

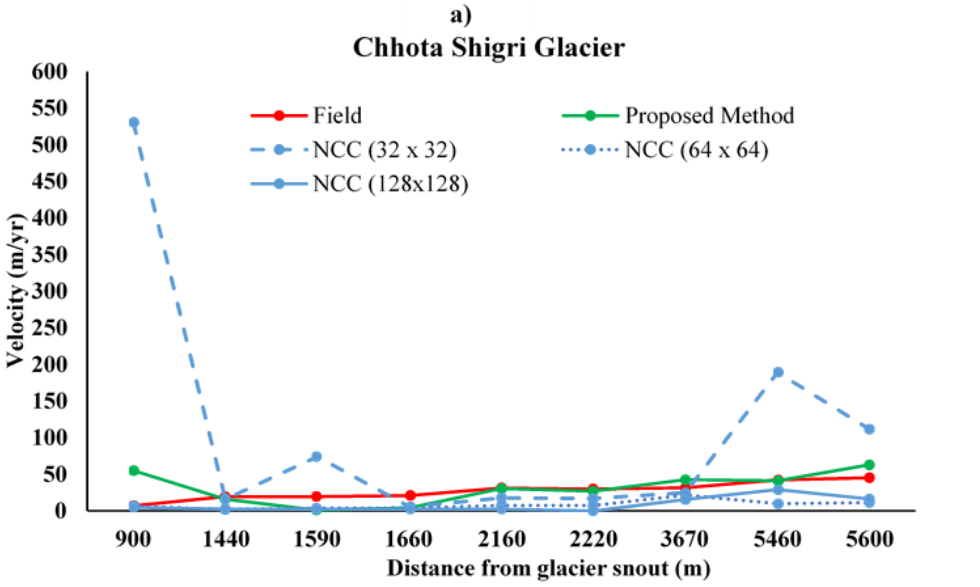

b)

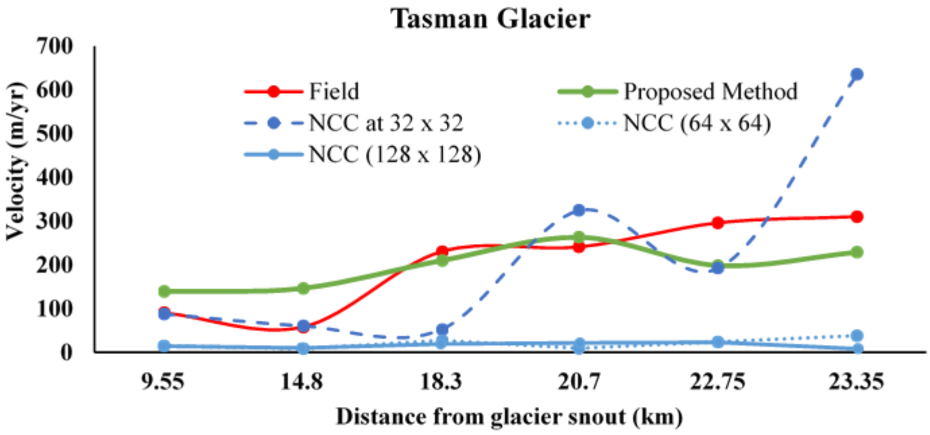

Tasman Glacier
Velocity (m/yr)
700
600
500
400
300
200
100
0
Field
Proposed Method
NCC at 32 x 32
NCC (64 x 64)
NCC (128 x 128)
9.55
14.8
18.3
20.7
22.75
23.35
Distance from glacier snout (km)

c)

Appendix-A5

Estimated vertical velocity w_s (in m/yr) for the four study glaciers.

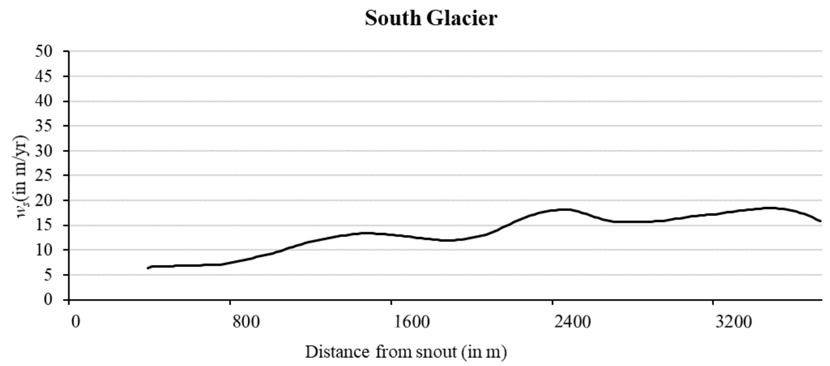

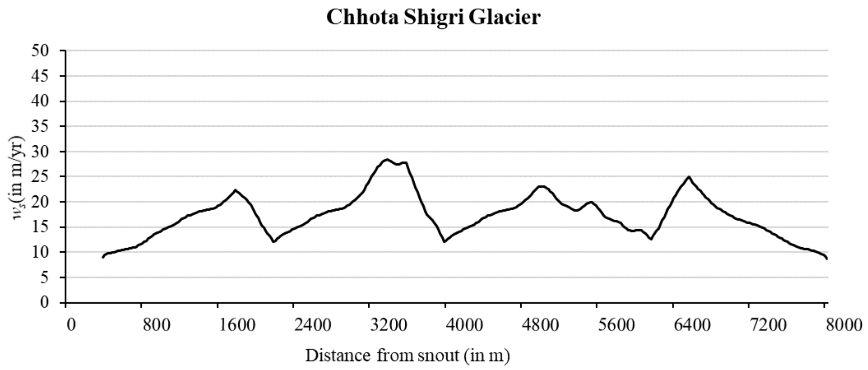

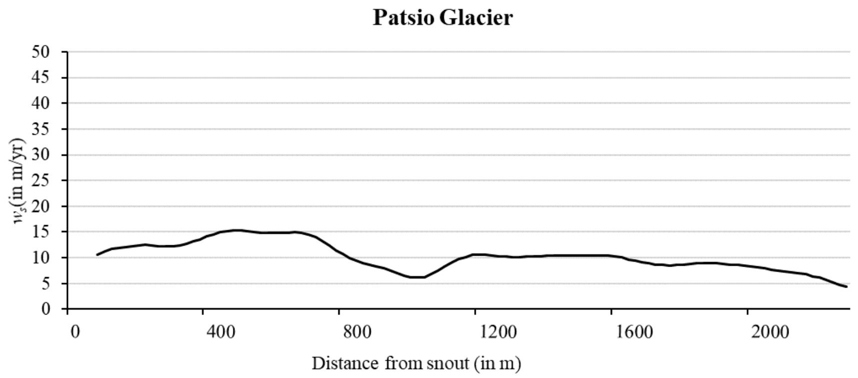

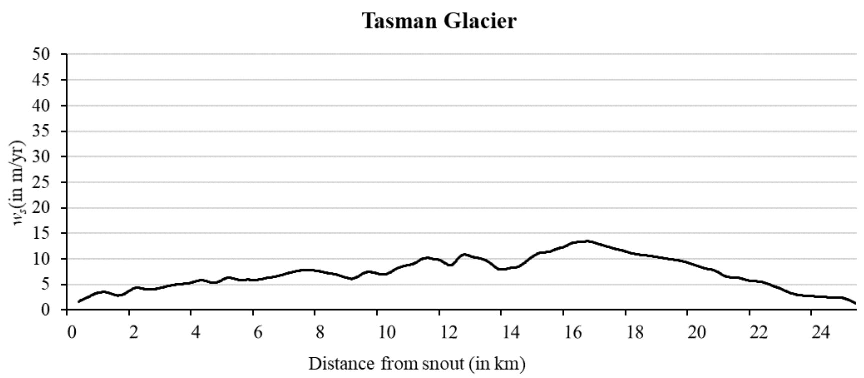

Appendix-A6

Estimated glacier surface velocity of Patsio Glacier calculated using the proposed SWIFT (**S**patially varying **WI**ndow based maximum likelihood **F**eature **T**racking) algorithm in Chapter 5. The velocity represents the estimates for period 2016-17 calculated using optical data in chapter 4.